ATOMIC FORCE FLUORESCENCE MICROSCOPY

COMBINING THE BEST OF TWO WORLDS

Roel Kassies

Samenstelling promotiecommissie:

Prof. dr. N.F. van Hulst	Universiteit Twente (voorzitter)
Prof. dr. V. Subramaniam	Universiteit Twente
Dr. C. Otto	Universiteit Twente
Prof. dr. A.G.J.M. van Leeuwen	Universiteit Twente
Prof. dr. W.L. Vos	Universiteit Twente
Prof. dr. R. van Grondelle	Vrije Universiteit Amsterdam
Prof. dr. A.J. Meixner	Universiteit van Siegen (Duitsland)

Acknowledgement

This research was financially supported by:

- The Netherlands Organization for Scientific Research NWO
- The Institute for Biomedical Engineering (BMTI), University of Twente

R. Kassies,
Atomic force fluorescence microscopy; combining the best of two worlds
Proefschrift Universiteit Twente, Enschede.
ISBN 90-365-2150-5
Copyright © R. Kassies, 2005
Printed by FEBODRUK BV, Enschede

ATOMIC FORCE FLUORESCENCE MICROSCOPY

COMBINING THE BEST OF TWO WORLDS

PROEFSCHRIFT

ter verkrijging van
de graad van doctor aan de Universiteit Twente,
op gezag van de rector magnificus,
prof. dr. W.H.M. Zijm,
volgens besluit van het College voor Promoties
in het openbaar te verdedigen
op donderdag 10 maart 2005 om 16.45 uur

door

Roelf Kassies
geboren op 3 januari 1976
te Meppel

Dit proefschrift is goedgekeurd door:

Prof. dr. V. Subramaniam	promotor
Dr. C. Otto	assistent promotor

Contents

Chapter 1

Introduction

The invention of the microscope and the telescope in the 1590s triggered enormous interest in exploring previously unobservable worlds. The observations made from those explorations would transform human understanding of the world and the universe.

1.1 Confocal microscopy

One of the early pioneers in the history of the microscope was the Dutch lens maker Zacharias Janssen, who invented the first compound microscope in 1595. However it was Antoni van Leeuwenhoek, a Dutch scientist and maker of microscopes, who built the world's first practical microscope around 1660 and used it to study bacteria, yeast plants, the teeming life in a drop of water, and the circulation of blood corpuscles in capillaries. Throughout the following centuries, the microscope was further perfected. Primarily in biological research, the desire arose to image thin slices of the specimen without the need to mechanically section the sample. Optical sectioning with conventional microscopy is of poor quality because the images are degraded by out-of-focus information (Amos *et al.*, 1987), which limits the attainable resolution. To overcome this problem, Minsky invented a new type of microscope in 1957: the confocal scanning optical microscope (CSOM) (Minsky, 1961; Minsky, 1988). The basic principle of this microscope is illustrated in Fig. 1.1. In confocal microscopy only one spot on the sample is illuminated at a time through a pinhole, in contrast with conventional wide field microscopy where the whole sample is illuminated and imaged at once. The light scattered by the specimen is collected through the same or another pinhole. By scanning the spot or the sample in a raster pattern a complete image can be formed. Scattered light from an out-of-focus spot will be de-focused on the pinhole and hence will not pass to the detector. Confocal microscopy therefore enables 3 dimensional optical sectioning.

In the early years the potential of the confocal microscope was not fully developed because of the lack of an adequate light source. The invention of the laser solved this problem and in 1969 Davidovits & Egger developed a CSOM using a laser as a light source (Davidovits and Egger, 1969). In 1979, Brakenhoff and co-workers

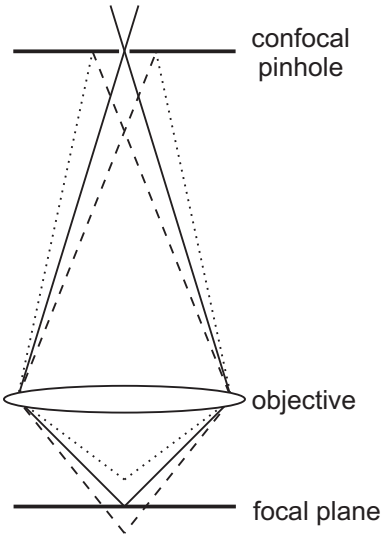

Figure 1.1. Basic principle of the confocal microscope. Light from the focal spot passes the confocal pinhole and will be detected (solid line). Out-of-focus light will be blocked by the pinhole (dashed and dotted lines).

demonstrated a well engineered confocal laser scanning microscope, showing the improvement in definition and contrast obtainable with confocal imaging and its use in biological applications (Brakenhoff *et al.*, 1979).
Fluorescence imaging is probably the most widely used application of the CSOM. Fluorescence microscopy is of great importance because fluorescent labels can be used as markers to follow biological activity. The CSOM's ability to remove out-of-focus fluorescence contributions dramatically improves the detail in the images (White *et al.*, 1987). With the advent of very sensitive detectors it is now possible to detect fluorescence emission down to the level of individual molecules (Shera *et al.*, 1990; Weiss, 1999).
In the quest to observe ever smaller details, light microscopy runs into its fundamental limit. The obtainable resolution with conventional light microscopy is limited by diffraction to roughly half the wavelength of the light ($\sim 250 - 300$ nm). In order to image even smaller details, sophisticated far field optical microscopy techniques have been developed such as 4-Pi microscopy (Hell and Stelzer, 1992; Hell *et al.*, 1997; Schrader *et al.*, 1998), harmonic excitation light-microscopy (HELM) (Frohn *et al.*, 2000) and stimulated emission depletion (STED) microscopy (Klar and Hell, 1999; Klar *et al.*, 2000). With these techniques, optical resolutions in the range of $\lambda/5 - \lambda/10$ can be achieved. Other types of microscopes were built using radiation with smaller wavelengths such as x-rays or electrons. However these techniques are not always applicable to biological research. Yet another type of microscopy, scanning probe microscopy, has become an important tool to break the limits of optical methods.

1.2 Atomic force microscopy

In 1981, Binnig, Rohrer, Gerber & Weibel introduced the first of the family of scanning probe microscopes (SPM) known today, the scanning tunneling microscope (STM) (Binnig *et al.*, 1982b; Binnig *et al.*, 1982a). In this technique, a sharp conducting tip

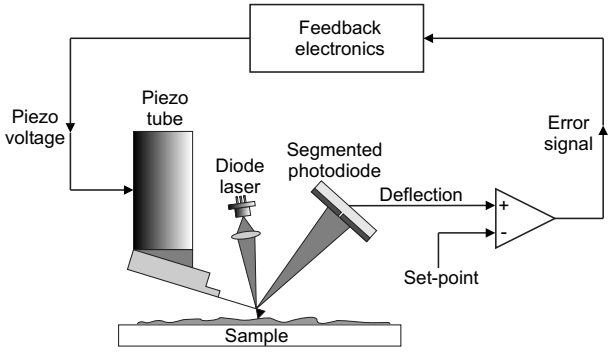

Figure 1.2. Schematic of the AFM. The deflection signal is used in a feedback loop in order to maintain a constant deflection and consequently a constant imaging force.

is brought close to the sample surface. When a potential difference is applied between the tip and the surface, electrons can tunnel between the tip and the sample. This tunneling current depends exponentially on the tip-sample separation. Scanning the tip in a raster pattern over the surface, while measuring the tunneling current yields a topographic image of the sample surface. The scanning motion of the tip is performed by a piezo-electric 3-dimensional scanner. The STM was the first instrument to generate real-space images of surfaces with atomic resolution. Five years later, in 1986, Binnig and Rohrer were awarded the Nobel prize in physics for their invention.

A limitation of the STM is the fact that only conducting or semiconducting samples can be imaged. To be able to also image surfaces of insulators, Binnig, Quate & Gerber invented the atomic force microscope (AFM) in 1986 (Binnig *et al.*, 1986). In atomic force microscopy, a very sharp tip located on the free end of a cantilever is scanned over the sample surface. The forces between the tip and the sample surface cause the cantilever to deflect. Detecting the cantilever deflection from point to point results in a map of the surface topography. In the first AFM, the deflection was measured by a tunneling tip on the back of the cantilever. In 1987, Albrecht & Quate showed that it was possible to obtain atomic resolution with the AFM (Albrecht and Quate, 1987).

An essential step for the biological application of the AFM was the demonstration by Marti *et al.* in 1987 that the AFM can be operated under a fluid layer (Marti *et al.*, 1987). The first demonstration of AFM imaging under physiological conditions on a biological sample was given by Drake *et al.* (1989). They used an optical lever method to detect the cantilever deflection, introduced a year before by Meyer & Amer (1988). This method is the most widely used detection scheme used in AFM today.

In the traditional way of AFM imaging, the tip is in continuous contact with the sample surface during scanning, the so-called contact mode. However, when imaging soft or weakly immobilized samples in contact mode, the lateral forces were found to easily disrupt the sample or remove it from the surface. In order to reduce the lateral forces, tapping mode AFM was introduced in air (Zhong *et al.*, 1993) and in liquid (Hansma *et al.*, 1994; Putman *et al.*, 1994). In this mode, the cantilever is oscillated near its resonance frequency and the tip only gently touches the sample at the bottom of its travel. The change in oscillation amplitude caused by the interaction with the sample provides the height signal in tapping mode.

AFM imaging can be performed in either constant height mode or constant force mode. In the constant height mode, the spatial variation in the deflection or tapping amplitude is used directly to generate a topographic image because the height of the scanner is fixed as it scans. In constant force mode, the cantilever deflection or the tapping amplitude is used as an input to a feedback circuit that moves the scanner up and down in z-direction responding to the topography by keeping the deflection or amplitude constant, illustrated in Fig. 1.2. In this case, the image is generated from the scanner's motion. The constant cantilever deflection results in a well controlled constant imaging force. For this reason the constant force mode is generally preferred, especially for imaging of soft and fragile biological material.

Because of its unique capacity to provide structural information on the (sub)nanometer scale in a biologically relevant aqueous environment, the atomic force microscope has since its introduction evolved into a powerful and widely used tool in biological research. Detailed images of single protein structures have appeared in the literature (Czajkowsky and Shao, 1998; Viani *et al.*, 2000), and extremely high resolution structural information is obtained on crystallized protein samples (Müller *et al.*, 1999b; Stahlberg *et al.*, 2001; Scheuring *et al.*, 2003a; Bahatyrova *et al.*, 2004a; Fotiadis *et al.*, 2004b). Measurements on membrane proteins in their native membranes (Bahatyrova *et al.*, 2004b; Fotiadis *et al.*, 2004a; Scheuring *et al.*, 2004a) provide information on the natural higher order organization of these proteins. In addition to being an imaging tool, the AFM can be used to measure mechanical properties of proteins and the strength of inter- and intra-molecular bonds (Lee *et al.*, 1994; Hinterdorfer *et al.*, 1996; Rief *et al.*, 1997; Müller *et al.*, 1999a; Oesterhelt *et al.*, 2000). Furthermore, using the AFM tip as a manipulation tool allows the precise and controlled modification of biological systems from the level of cells down to the scale of individual molecules (Schoenenberger and Hoh, 1994; Thalhammer *et al.*, 1997; Fotiadis *et al.*, 2002).

1.3 Combining the best of two worlds

Traditional AFM imaging is based on very general tip sample interactions, which makes the technique applicable to a wide range of samples. However, this also strongly limits its capacity to identify different objects comprising the sample, unless they have a very distinct shape or size. Several other modes of AFM, such as lateral force microscopy (Mate *et al.*, 1987; Marti *et al.*, 1990; Overney *et al.*, 1994), chemical force microscopy (Frisbie *et al.*, 1994; McKendry *et al.*, 1998; Wong *et al.*, 1998) and phase contrast imaging (Anczykowski *et al.*, 1996; Cleveland *et al.*, 1998; Noy *et al.*, 1998) use material specific tip-sample interactions to improve the chemical specificity. However, these modes are also often not distinctive enough to reliably identify surface species.

Optical spectroscopy and imaging, on the other hand, are well established techniques enabling the spectroscopic discrimination of distinct species in the sample. By fluorescent labelling of specific proteins it is possible to follow the processes and dynamics

of these components within living cells. Optical parameters such as intensity, wavelength, polarization and fluorescence lifetime provide valuable information about the specimen and its surroundings (Kühnemuth and Seidel, 2001). However, one of the major disadvantages of optical spectroscopy is its comparatively poor spatial resolution.
Remarkably, AFM and optical imaging have complementary strengths and weaknesses. Therefore, a combination between AFM and optical spectroscopy provides a very powerful tool in biological research. Such an *atomic force fluorescence microscope* (AFFM) directly combines high resolution structural imaging with chemically specific optical imaging. In addition to the added value of combined imaging, Weiss (1999) and Wallace *et al.* (2003) already described the possibilities of using the AFM tip as a force sensor/manipulator while simultaneously recording optical responses of the molecules under study. The number of potential applications of an AFFM is numerous.
A similar combination between topographic and optical imaging is realized in near-field scanning optical microscopy (NSOM) (Dunn, 1999). In this technique, a tapered optical fiber with a sub-wavelength sized aperture (typically 70-120 nm) is scanned near the sample surface at a distance within ~ 10 nm. The strongly localized optical near field at the aperture illuminates the sample, resulting in an optical image with a spatial resolution determined by the aperture size. During scanning, the contours of the sample surface are followed by the fiber tip, yielding a perfectly correlated topographic image of the same area. However, in order to achieve sufficient optical throughput, the aperture size has a lower limit, which leads to a much lower topographic resolution than that achievable with AFM. In NSOM, the same probe is used to obtain both topographic and optical images, which can lead to artifacts in the optical signal caused by the z-motion of the near field probe (Hecht *et al.*, 1997). Furthermore, the use of a fragile optical probe complicates the operation of the microscope. Integration of AFM and confocal fluorescence microscopy in an atomic force fluorescence microscope (AFFM) provides an easier and more flexible way of combining high topographic resolution with sensitive spectroscopic identification capability.

1.4 AFFM on bacterial photosynthetic systems

The interest to develop the atomic force fluorescence microscope described in this thesis, was mainly inspired by research on bacterial photosynthetic systems. This section describes the basic principles of bacterial photosynthesis and the role of the AFFM in the research on this biological system.

1.4.1 Bacterial photosynthesis

Life as we know it today exists largely because of photosynthesis, the process through which light energy is converted into chemical energy by plants, algae, and photosynthetic bacteria. The primary processes of photosynthesis involve the absorption of

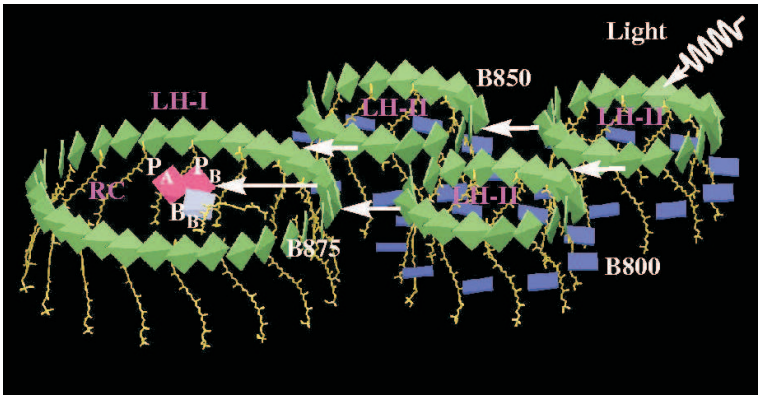

Figure 1.3. Schematic illustration of the primary steps in photosynthesis: light absorption and energy transfer towards the reaction center. For clarity, only the pigments of the LH complexes are shown. This figure was taken from www.ks.uiuc.edu/Research/psu/psu_inter.html.

photons by light harvesting complexes (LH's), transfer of the excitation energy from the LH's to the photosynthetic reaction centers (RC's), and the primary charge separation across the photosynthetic membrane. This charge separation eventually leads to the production of chemical energy in the form of ATP (adenosine triphosphate), through a series of dark reactions . In purple bacteria, this photosynthetic machinery is located within the intracytoplasmic membrane. The first steps of light absorption and energy transfer towards the RC is schematically illustrated in Fig. 1.3.
In the photosynthetic apparatus, light energy is absorbed by an antenna containing thousands of pigments (bacteriochlorophylls and carotenoids) that are highly organized in two types of ring shaped protein complexes, the LH1 and the LH2 complexes. The RC is situated within the LH1 ring and the LH2 complexes are believed to be located peripheral to the RC-LH1 core. In this way, the LH2 complexes enlarge the cross-section for capturing sunlight, supplying the RC with excitation energy. Time resolved spectroscopy revealed that excitation energy is transferred from the LH's to the RC in less than 100 ps with a very high quantum yield of 95 %. A review of the photosynthetic apparatus of purple bacteria is given by Hu *et al.* (2002). The excitonic mechanisms in photosynthesis is extensively discussed in Van Amerongen *et al.* (2000).
Most of the experiments in this thesis are performed on LH2 complexes. The structure and function of this particular light harvesting complex is discussed in more detail in the following section.

1.4.2 The LH2 complex

The crystal structure of the LH2 complex was first revealed for the species *Rhodopseudomonas acidophila* by Mc Dermott *et al.* (1995), closely followed by the analogous structure from *Rhodospirillum molischianum* (Koepke *et al.*, 1996). Data obtained by cryo-electron microscopy showed a similar structure for the LH2 complex of *Rhodobacter sphaeroides* (Walz *et al.*, 1998).
The basic building block of the LH2 complex is a heterodimer of two small (5-6 kDa) polypeptides, α and β, both consisting of a single transmembrane helix. This pair of apoproteins bind non-covalently three Bchl *a* and most likely two carotenoid

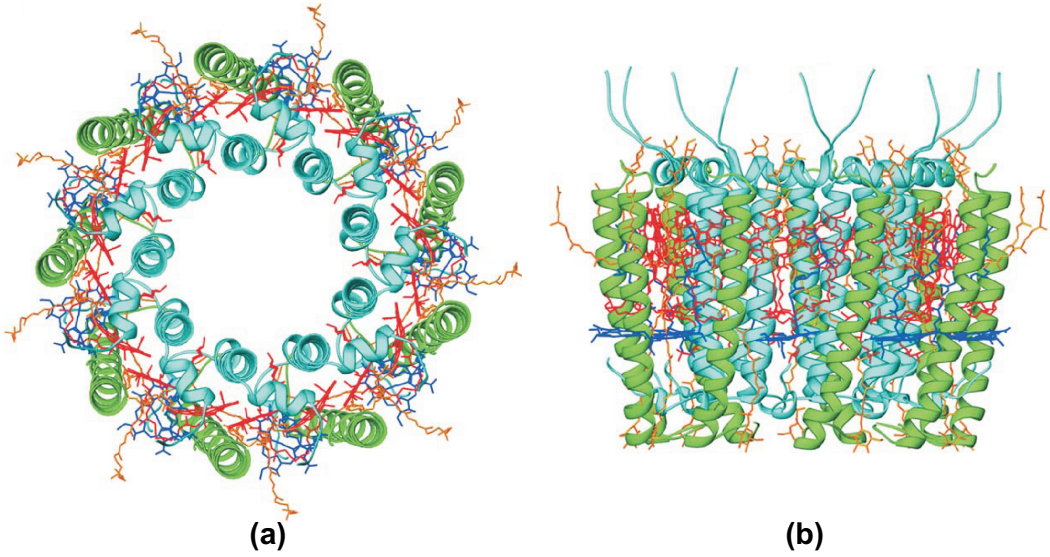

Figure 1.4. Structure of the LH2 complex from *Rhodopseudomonas acidophila* at 2.0 Å resolution. (a) View normal to the membrane plane. (b) A side view of the complex. The ring has a diameter of ∼6 nm and a height of ∼4 nm. This figure was taken from Cogdell *et al.* (2004).

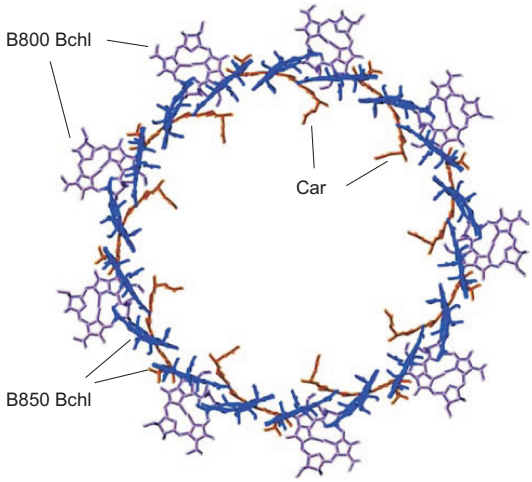

Figure 1.5. View normal to the membrane plane of the LH2 complex from *Rhodopseudomonas acidophila* with the α and β polypeptides removed, leaving only the Bchl *a* and the carotenoid molecules. Two of each group of pigments is marked in the figure. This figure was taken from Cogdell *et al.* (2004).

molecules. The LH2 complex of most species comprises nine of these subunits (the LH2 complex of *Rs. molischianum* possesses eight subunits) arranged to form a closed ring, with the α-polypeptides on the inside and the β-polypeptides on the outside of the ring. Two of the Bchl pigments of each subunit are tightly coupled, sandwiched between the two polypeptides, resulting in a closely interacting ring of nine Bchl dimers with an absorption maximum at $\sim$ 850 nm. This ring of 18 pigments is named B850 after the position of this absorption band. The third Bchl pigment is bound by the β-polypeptide of the subunit to form a nine membered ring of monomers, absorbing around 800 nm, named B800. Finally, each $\alpha\beta$-apoprotein pair binds a carotenoid which stretches along the whole height of the complex.

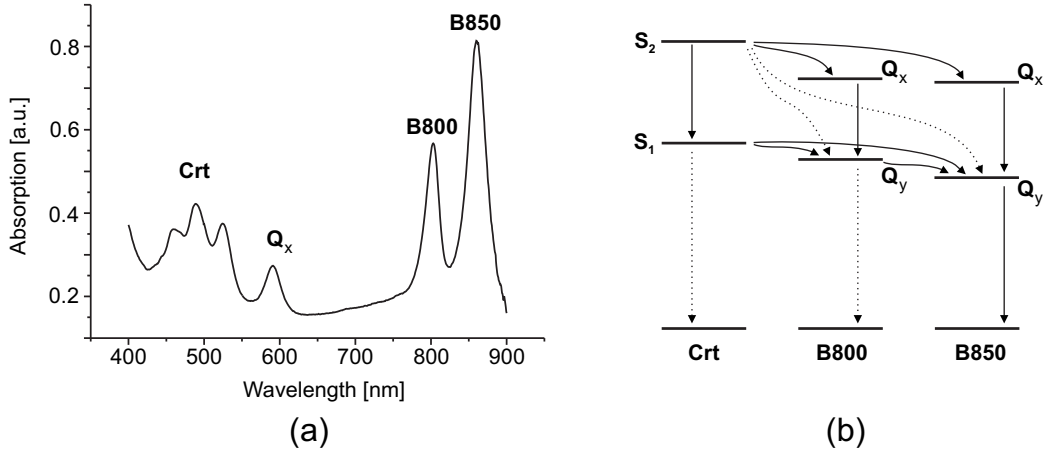

Figure 1.6. (a) Absorption spectrum of LH2. The complex can be excited in the carotenoids, the B800 ring and the B850 ring. (b) Scheme of energy levels together with excitation transfer and relaxation processes involved in LH2. Solid lines show the major and the dotted lines the minor transfer/relaxation channels. This figure was adapted from Sundström *et al.* (1999).

The Bchl's are the main light harvesting pigments. The B800 Bchl's are relatively far apart (21.2 Å) and excitations in this group of Bchl's are localized on individual pigments. In contrast, the 18 Bchl's in the B850 band are very close together, 8.9 Å between two Bchl's in one subunit and 9.6 Å between Bchl's of neighboring subunits, leading to an excitonic interaction. The excitation energy in this ring is found to be delocalized over 3–4 pigments at room temperature (Monshouwer *et al.*, 1997). The carotenoids have three main functions. First, they protect the light harvesting complexes by directly quenching both triplet excited Bchl's and singlet oxygen. This is their essential function. Second, carotenoids play a role as accessory light harvesting pigments, absorbing light in the blue-green and yellow regions of the spectrum. Third, in many antenna complexes, carotenoids serve a structural role (Fraser *et al.*, 2001). The suggested second carotenoid per $\alpha\beta$-apoprotein pair has been discovered recently in *Rhodopseudomonas acidophila* (Papiz *et al.*, 2003). The complete structure of the LH2 complex is illustrated in Fig. 1.4. In Fig. 1.5 the LH2 complex is shown with the α and β polypeptides removed, leaving only the pigments. Both figures were taken from Cogdell *et al.* (2004).

The arrangement of all the pigment molecules in the LH2 complex results in an absorption spectrum shown in Fig. 1.6(a). The LH2 complex can be excited through the carotenoids in the visible wavelength region ($\sim$450 – 550 nm) and in the B800 and B850 Bchl's at 800 and 850 nm respectively. Within the complex the excitation energy is very rapidly transferred towards B850 with transfer times in the order of 1 ps or less (Fig. 1.6(b)). An extensive overview of transfer processes and times is given in Sundström *et al.* (1999). *In vivo* the energy is subsequently transferred from B850 to B850's of neighboring LH2's and finally to the LH1 complex (absorption band

around 870-880 nm) where the energy is transferred to the reaction center eventually resulting in a transmembrane charge separation. However, when the complexes are isolated the excitation energy will be released by fluorescence after $\sim$ 1 ns with a quantum yield of $\sim$ 10% (Monshouwer *et al.*, 1997). The fluorescence emission has a maximum at $\sim$ 870 nm.

1.4.3 AFFM to relate structure and function

The functional properties of the photosynthetic system such as the spectral position of the absorption peaks of the LH complexes, the rapid and efficient energy transfer within the LH2 complex to B850, the energy transfer between LH2's and finally towards the LH1 and the RC, all rely strongly on the structure of the individual complexes and the higher order organization of the complexes within the membrane. Information on the structure of the RC (Fritzsch *et al.*, 2002), the LH2 complex (McDermott *et al.*, 1995; Koepke *et al.*, 1996; Walz *et al.*, 1998; Papiz *et al.*, 2003) and the LH1-RC complex (Karrasch *et al.*, 1995; Walz *et al.*, 1998; Jungas *et al.*, 1999; Jamieson *et al.*, 2002; Roszak *et al.*, 2003) have been obtained using x-ray crystallography and electron microscopy. These techniques provide high resolution information when the proteins are crystallized into a highly periodic structure. However, the natural membranes containing all proteins involved in photosynthesis do not display such a long range periodicity, which makes these techniques ineffective for the study of the membrane architecture. To reveal the higher order organization of the photosynthetic membrane, atomic force microscopy is the only technique available that is capable of directly imaging the structure with high resolution in a relevant aqueous environment. Recently, high resolution AFM data on these membranes has appeared in literature, providing a first glimpse at the native architecture (Scheuring *et al.*, 2003b; Scheuring *et al.*, 2004a; Scheuring *et al.*, 2004b; Bahatyrova *et al.*, 2004b).
Atomic force fluorescence microscopy can bring the research a significant step further by providing the ability to directly relate structure and function. Spectroscopic information acquired on individual LH complexes, crystals of complexes and photosynthetic membranes can be related with corresponding high resolution structural AFM data of the same object. Furthermore, the AFM tip can also be used as a nanomanipulation tool to interact with the complexes and asses their flexibility and record the spectral responses.
The significant added value of combined spectroscopic and topographic information forms a strong motivation for the development of the atomic force fluorescence microscope.

1.5 Outline of this thesis

This thesis describes the development of an atomic force fluorescence microscope which is capable of simultaneous measurements with single molecule sensitivity in a liquid environment. The AFFM is demonstrated on individual proteins, crystals and

membranes of a bacterial photosynthetic system.
In chapter 2, the requirements of the AFFM are discussed and the design of the instrument is presented. Several modes of operation that were implemented in the software are described.
The optical lever detection of the cantilever deflection in atomic force microscopy can cause disturbances due to interference and optical feedback effects. In chapter 3, a simple method is introduced which strongly reduces the interference effects and eliminates optical feedback.
Chapter 4 describes the performance of the AFFM. The requirements, defined in chapter 2, are tested in this chapter. The AFFM is demonstrated to be capable of single molecule fluorescence detection in the near infra-red part of the spectrum, and high resolution AFM imaging resolving individual protein structures.
The simultaneous operation of the AFFM is demonstrated in chapter 5. The various modes of operation are applied to 2-dimensional crystals of LH2 complexes, membrane fragments containing both LH1 and LH2 complexes. Attempts to simultaneously measure on individual LH complexes are shown and discussed.
The AFFM can perform simultaneous measurements using chromophores throughout the whole visible to near-IR spectral region. This greatly enhances the general application of the AFFM in biological research and the strongly developing field of (bio)-nanotechnology. To facilitate fluorescence excitation through the whole wavelength range, the AFFM was connected to an Argon-Krypton mixed gas laser. The prism set-up described in chapter 6 enables the flexible selection of any wavelength or combination of wavelengths from this laser.
In chapter 7, the potential future applications of the AFFM are described.

Chapter 2

Development of the atomic force fluorescence microscope

Integration of atomic force microscopy (AFM) and confocal fluorescence microscopy (CFM) combines the high resolution topographical imaging of AFM with the reliable (bio)-chemical identification capability of optical methods. The development of the atomic force fluorescence microscope (AFFM) is described in this chapter. This AFFM is capable of performing simultaneous optical and topographic measurements with single molecule sensitivity throughout the whole visible to near-infrared spectral region. The instrument is equipped with a spectrograph / CCD camera combination, enabling combined topographic and fluorescence spectral imaging, which significantly enhances discrimination of spectroscopically distinct objects. The modular design allows easy switching between different modes of operation such as tip-scanning, sample-scanning or mechanical manipulation, all of which are combined with synchronous optical detection.

2.1 Introduction

Several examples of AFM and fluorescence microscope combinations have been reported in the literature over the last few years (Lieberman *et al.*, 1996; Lal and Proksch, 1997; Foubert *et al.*, 2000; Horton *et al.*, 2000; Kolodny *et al.*, 2001; Noy and Huser, 2003; Gradinaru *et al.*, 2004). One of the most significant problems in these designs is the optical background in the fluorescence detection caused by the laser used in the AFM to detect the cantilever position (Meyer and Amer, 1988). Due to this problem, most combined microscopes perform the AFM and fluorescence measurements sequentially. For simultaneous imaging, this laser light must be filtered from the detection path using high quality filters, consequently blocking a potentially useful part of the spectrum (Gradinaru *et al.*, 2004). An alternative approach is demonstrated by Noy *et al.* (2003) who implemented an interleaved scanning mode, where each line is scanned twice during imaging. In the first scan the AFM collects the topographical information. During the second scan, the AFM laser is switched off and the optical information is collected. In this method, the two microscopes still operate

sequentially on the same spot, and can therefore not be used to perform mechanical manipulations on the sample while simultaneously recording optical responses.
This chapter describes the development of the purpose-designed AFFM set-up which can perform truly simultaneous AFM and fluorescence imaging, force extension measurements, and nano-manipulation.

2.2 Requirements of the combined microscope and fundamental choices

2.2.1 Requirements of the AFFM

The combined microscope is primarily designed for the study of the light harvesting system of the photosynthetic bacterium *Rhodobacter sphaeroides*. The goal of the microscope is to perform simultaneous optical and topographic imaging, as well as mechanical nanomanipulation using the AFM tip, while synchronously detecting the optical responses. These measurements should be carried out on specimens ranging from native photosynthetic membranes and two-dimensional crystals of light harvesting complexes down to individual pigment-protein complexes. Because of the significant potential for the application of an integrated AFM/optical microscope in biophysical research, the set-up should be adaptable for the study of a wide range of systems. These goals lead to a set of demands for the design of the combined microscope:

- The confocal fluorescence microscope must feature single molecule fluorescence sensitivity throughout the visible to near-infrared spectral region.
- The laser used in the AFM to detect the position of the cantilever should not excite the chromophores in the sample and thereby cause photobleaching.
- The light from the AFM laser should be completely removed from the detection path of the confocal fluorescence microscope.
- The AFM and the fluorescence microscope should be able to measure simultaneously on the same sample.
- The combined microscope should facilitate many different types of experiments (modes of operation) with flexible switching between different modes.

2.2.2 Configuration of scanning elements

Since both AFM and CFM are scanning microscopy techniques, there are a number of possible choices for the design of the scanning elements in the combined microscope. An overview of the different options is presented in Fig. 2.1. The most fundamental selection considers the main scanning scheme.

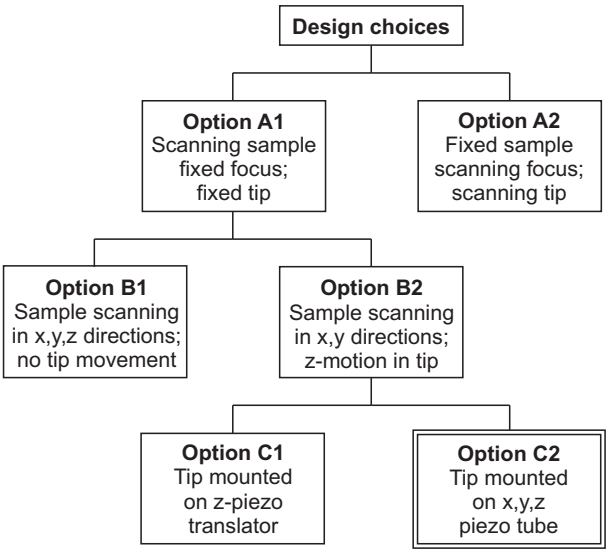

Figure 2.1. Selection diagram of the different options for the configuration of the scanning elements in the AFFM. The combination of an x,y piezo sample scanner with an x,y,z piezo-tube tip scanner was found to be optimal for the combined microscope.

Option A1 represents the configuration in which the AFM-tip and the focus are placed in a fixed location on the optical axis of the CFM in combination with a scanning sample. In this scheme both microscopes share the same scanner and therefore the images are inherently correlated. The lateral scan ranges of the AFM and the CFM are the same, determined by the sample scanner. Option A2, in which the sample is fixed and the tip and the focus perform lateral scanning, requires two scanning elements, namely a tip scanner and an optical beam scanning mirror. During combined imaging, both scanners have to operate simultaneously (requiring 4 analog output channels in stead of 2) and perfectly synchronously in order to keep the tip and the focus well aligned. However, both elements will have a different dynamic behavior which will complicate the synchronization. The simpler, and better-controllable, configuration of option A1 is therefore most suitable.

Option A1 can be implemented either with an x,y,z sample scanner, which facilitates motion in all three directions (option B1) or with an x,y scanner, only providing lateral motion (option B2). In option B1, the tip can in principle be completely fixed, since the sample provides the z-motion necessary to keep a constant deflection during imaging. This allows a simple design with only one scanning element. However, most suitable x,y,z scanning stages have a relatively low resonance frequency in the z-direction leading to a limited operational bandwidth. For example, the unloaded resonance frequency in the z-direction for the P-517.3CD x,y,z-stage (Physik Instrumente, Karlsruhe, Germany) is 1100 Hz, a value which will drop when the mass of a sample holder is added. AFM images are typically recorded at pixel frequencies of $>$ 2000 Hz. Using an x,y,z-stage would therefore strongly limit the AFM scan speed. A slow scan speed results in a long image time, which induces photobleaching of the chromophores in a combined experiment. The sample scanner in option B2 only moves the sample in the lateral plane and the vertical movement has to be performed by a separate piezo element. This allows the selection of a piezo scanner with a sufficiently high resonance frequency to accommodate the z-motion of the tip.

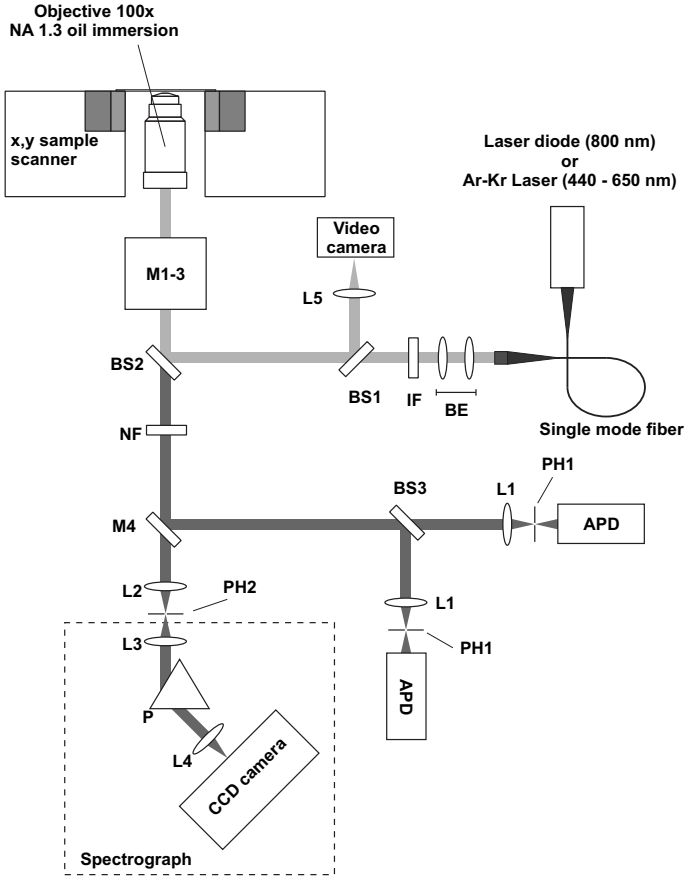

BE	Beam expander
IF	Narrow band interference filter
BS1	Beam splitter T=5% ; R=95%
BS2	Dichroic beam splitter
BS3	Beam splitter (pol/dichroic)
M1-4	Mirror
NF	Notch filter
L1	Lens f=60 mm
L2	Lens f=19 mm
L3	Lens f=50 mm
L4	Lens f=100 mm
L5	Lens f=200 mm
PH1	Pinhole 25 μm
PH2	Pinhole 10 μm

Figure 2.2. Schematic layout of the confocal fluorescence microscope

Option B2 is therefore preferable over option B1 for this application.
In option C1, the tip is mounted on a high bandwidth linear piezo translation stage. Option C2, where the tip is mounted on an x,y,z piezo-tube, enables an additional lateral motion of the tip. During simultaneous imaging, the AFM tip should be aligned on the optical axis of the CFM. For the coarse alignment, a set of differential spindles can be used to orient the AFM head (accuracy of 0.1 μm), however for the last accurate alignment a piezo x,y positioning is valuable. In addition, option C2 enables tip scanning AFM imaging and more flexibility in tip movement for mechanical nanomanipulation.
In conclusion, a configuration consisting of an x,y sample scanner in combination with an x,y,z tip scanner is found to be optimal for the AFFM design and combines high precision with maximum flexibility.

2.3 The confocal fluorescence microscope

2.3.1 Design of the CFM

The confocal fluorescence microscope is designed in an inverted geometry to accommodate the integration with the AFM (Fig. 2.2). The microscope pedestal is constructed from a solid aluminum block ($20 \times 20 \times 10$ cm). This pedestal comprises the sample

scanner (P-730 XY, Physik Instrumente, Karlsruhe, Germany), the objective (Plan Fluor 100×, oil immersion, NA 1.3, Nikon), a manual focussing mechanism and a mirror to couple light in and out of the objective. The sample stage has a scan range of 40×40 μm^2 with a minimal step size 0.5 nm in closed loop mode.

The confocal microscope typically uses a diode laser (RLT80010MG, $\lambda = 800$ nm, Roithner Laser Technik, Vienna, Austria) as a light source. The laser beam is passed through beam expander BE (2×) in order to completely fill the entrance aperture of the objective. The spectral side bands typical of diode laser emission are suppressed by narrow bandpass interference filter IF (F10-800.0-4-1.00, CVI Technical Optics LTD, UK), which only transmits the main emission peak of the laser. The excitation light is subsequently reflected by dichroic beam splitter BS2 (Q850LPXXR, Chroma, Brattleboro, USA) and mirror combination M1-3 towards the objective which focusses the light onto the sample. The fluorescence light is collected by the same objective and passes through the dichroic beam splitter. Back scattered laser light is mainly reflected by BS2 and BS1 to be imaged on a video camera, enabling the monitoring of the excitation focus and the AFM cantilever during the measurements. Any remaining excitation light in the detection path is removed by holographic notch filter NF (HNPF-800, Kaiser Optical Systems). By switching a foldable mirror, the fluorescence light can be directed either towards two single photon counting avalanche photodiodes (APD) (SPCM-AQR-14, Perkin Elmer Optoelectronics), or towards a home-built prism based spectrograph, with single molecule sensitivity, equipped with a liquid nitrogen cooled back illuminated CCD camera (Spec-10:100B, Princeton Instruments). The APD's are suitable for measurements which require high time resolution, such as recording fast dynamics in fluorescence timetraces or rapid fluorescence imaging. By using a dichroic beam splitter, two separate spectral regions can be monitored simultaneously. Alternatively, a polarizing beam splitter can be used to detect the emission in two perpendicular polarizations. The spectrograph CCD camera combination can be used for spectral imaging of the sample as well as for recording spectral time-traces, where a complete spectrum is recorded for each image pixel or time step respectively.

In addition to the excitation with 800 nm laser light, wavelengths in the visible spectral region (450-650 nm) from a mixed gas Argon-Krypton laser (Innova 70 spectrum, Coherent) can be used by means of an additional fiber connection. Any wavelength or combination of wavelengths from this laser can be easily selected by means of a specially designed prism based wavelength selector, and subsequently coupled into the single mode fiber (see Chapter 6). These visible laser lines can be used to excite the light harvesting complexes through the carotenoids. The dichroic beam splitter BS2 is designed such that it reflects from the visible wavelengths up to ~ 850 nm, so that the same beam splitter can be used for excitation through the carotenoids, the B800-ring and the B850-ring (Fig. 2.3).

The availability of many commonly used visible laser wavelengths from the Ar-Kr laser, and the flexibility with which these laser lines, or combinations of laser lines, can be selected, greatly enhances the applicability of the AFFM.

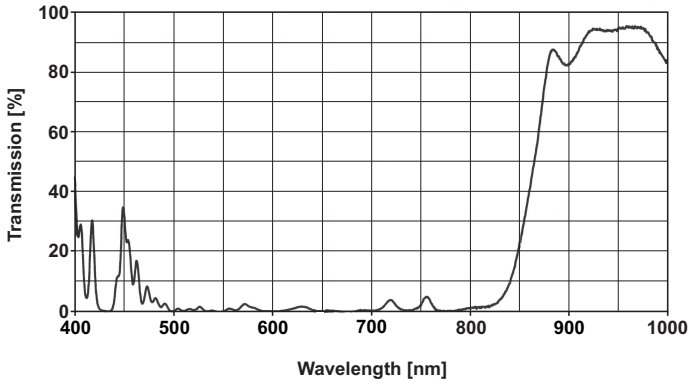

Figure 2.3. Transmission curve of dichroic beam splitter BS2 (Fig. 2.2), measured at and angle of 45°. The beam splitter was designed such that it can be used when exciting the carotenoids (visible wavelengths), the B800-ring and the B850-ring of the LH2 complex.

2.3.2 Spectrograph

In many biological research questions there is a demand to simultaneously observe multiple chromophores, e.g. in protein co-localization studies, where proteins are labelled with different chromophores. With the advent of fluorescent quantum dots, multi-color fluorescence experiments become even more appealing since a multitude of dots with different emission wavelengths can be excited with a single laser line.
The detection of multiple chromophores is usually achieved by using multiple detector channels in combination with suitable dichroic beamsplitters and emission filters. However, the number of wavelength bands that can be simultaneously detected in this way is limited. In addition, the broad emission spectra of fluorescent probes often partially overlap, which complicates the separation of different spectra, resulting in crosstalk between detection channels. Furthermore, the separate detectors record the integrated intensity over a spectral band, without the assessment of the shape of the spectrum.
The ability to measure a full fluorescence spectrum, using a spectrograph in combination with a sensitive CCD camera, solves these difficulties and provides information about the shape of the spectrum. Many different emission wavelengths can be easily detected simultaneously, without the need of specialized beam splitters and filters.
A fluorescence spectrum at room temperature is generally distributed over a relatively large wavelength range (tens of nanometers). Therefore, a spectral resolution in the order of 1 nm is sufficient to reveal relevant details within a spectrum. This allows the use of an equilateral prism as a dispersing element in the spectrograph, as opposed to a grating. In general, a prism is less dispersive than a grating, but has a slightly higher efficiency, which makes a prism preferable when low intensities are measured. For this spectrograph, SF11 glass was selected as prism material because of its comparatively strong dispersion. An extensive description of a similar type of spectrograph is described by Frederix *et al.* (2001).
The parallel beam of fluorescence light is focussed on the confocal pinhole PH2 of the spectrograph by lens L2 (Fig. 2.2). Lens L3 subsequently collimates the beam before it enters the prism. As a general rule, reflection losses are minimized for unpolarized rays travelling parallel to the base of the prism. This condition is termed 'minimum deviation'. The spectrograph is designed such that this condition is fulfilled. Lens

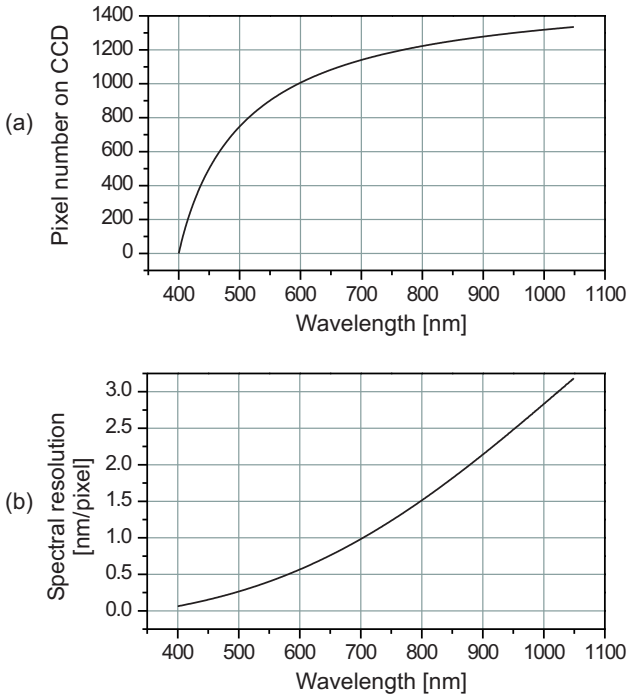

Figure 2.4. The fluorescence light entering the spectrograph is dispersed by the prism and imaged on the CCD camera. (a) Pixel position of each wavelength on the CCD chip. It is clear that the dispersion of the prism leads to a non-linear wavelength scale on the camera. (b) The non-linear wavelength scale corresponds to a changing spectral resolution as a function of the wavelength. The spectral resolution varies roughly between 0.25 and 3.0 nm/pixel.

L4 in combination with lens L3 images the pinhole (10 μm) onto a single pixel of the CCD camera (20 μm). The dispersion of the prism leads to a non-linear wavelength scale on the camera and consequently a wavelength dependent spectral resolution (Fig. 2.4). The resolution varies from $\sim$ 0.25 nm/pixel at 500 nm to $\sim$ 3.2 nm/pixel at 1050 nm.

2.4 Design of the atomic force microscope

The most widely used method for detection of cantilever displacement in atomic force microscopes is the optical beam deflection technique (Meyer and Amer, 1988). However, when an AFM is combined with a highly sensitive fluorescence microscope, the use of this technique causes several difficulties.

Part of the laser light, used in the optical beam deflection method, transmits through and passes beside the cantilever. This light is inevitably collected by the objective of the CFM and enters the detection path. This creates a significant background in the fluorescence measurements during simultaneous operation of both microscopes. While the application of high quality filters can remove this light from the detection path, this consequently blocks a potentially useful part of the spectrum.

In addition, light from the AFM laser may easily excite the fluorophores in the sample when their absorption peaks lie close to the emission wavelength of the laser. This limits the selection of fluorophores applicable in combined experiments and can cause an unwanted photobleaching of the fluorescent material.

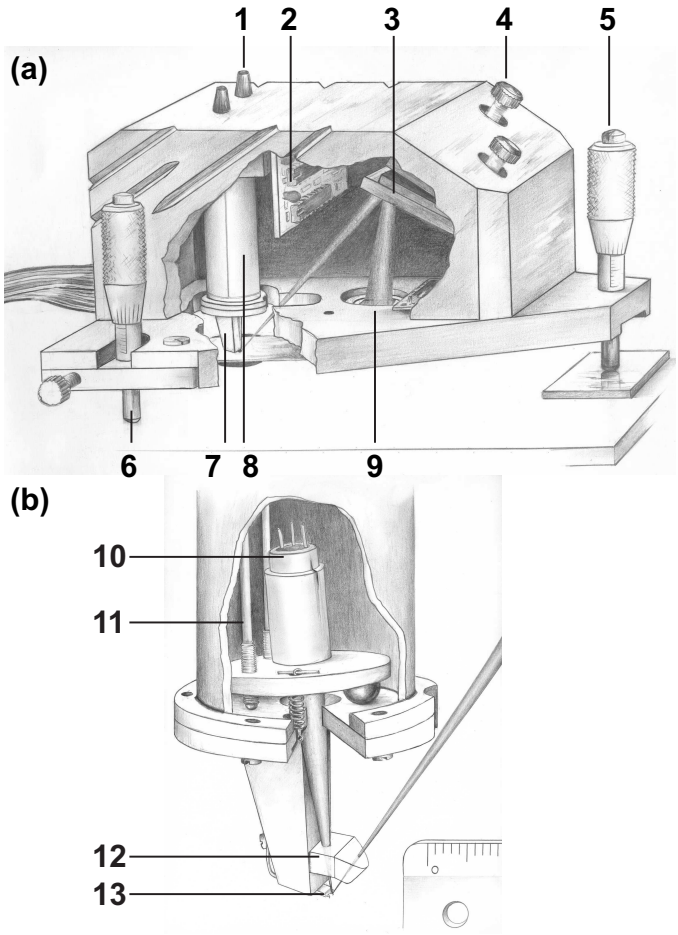

Figure 2.5. Schematic drawing of the home-built stand alone atomic force microscope. (a) Overall layout, (b) close-up of the laser diode (located inside the piezo tube) and the cantilever holder. 1) adjustment knobs for laser beam alignment, 2) pre-amplifier electronics, 3) beam-steering mirror, 4) mirror adjustment knobs, 5) fine approach spindle, 6) coarse approach spindle, 7) cantilever holder, 8) piezo tube x,y,z scanner, 9) quadrant detector, 10) laser diode and focussing lens, 11) flexible rods for laser alignment, 12) window for liquid measurements, 13) chip with cantilevers. The cantilever holder can be replaced by a liquid cell. The AFM for the combination microscope was adapted from this design.

The use of piezo resistive cantilevers circumvents these difficulties. This non-optical deflection detection scheme is based on the piezoresistive effect where the resistivity of a material changes with the applied stress. In this method, the deflection of a piezoresistive cantilever is detected, by measuring the electrical resistance of the cantilever by using a Wheatstone bridge circuit (Tortonese *et al.*, 1993). This scheme provides a direct electrical readout of the deflection, integrated in the cantilever, without the need of an external sensing method. However, this technique has some serious disadvantages. First, the method is less sensitive than the optical lever method. Piezoresistive cantilevers are mostly used in situations where their simplicity is particularly beneficial, e.g. in ultrahigh vacuum (Giessibl and Trafas, 1994), in cryostats (Thomson, 1999) and in portable and autonomous instruments (Furman *et al.*, 1998) where the reduced sensitivity is not an issue. In the study of proteins and organization of proteins in membranes however, a high sensitivity is crucial. Second, piezoresistive cantilevers have, to our knowledge, not been used to image biological specimens under aqueous conditions. The ability to measure in biologically relevant liquid environment is a prerequisite of the combined system. Third, the commercial availability of piezo levers is limited, which makes it hard to select a lever with optimal mechanical properties for each experiment. Fourth, piezoresistive cantilevers

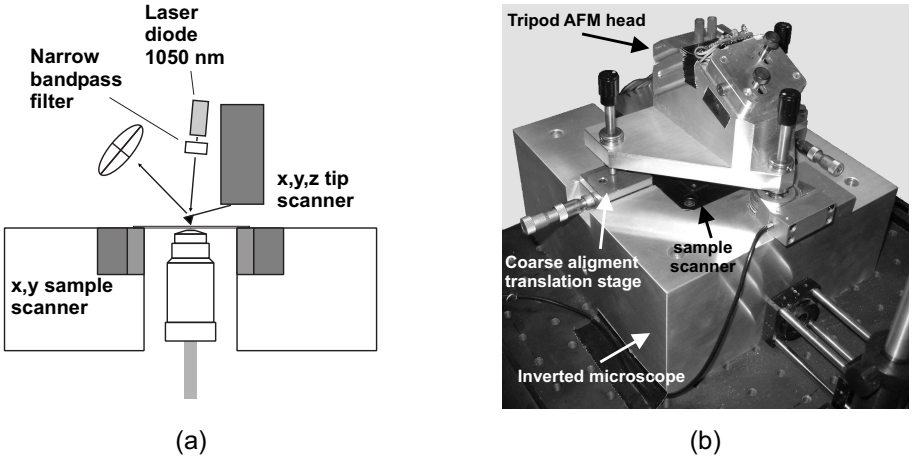

Figure 2.6. A laser diode with a wavelength of 1050 nm was installed in the AFM head in combination with a narrow band interference filter. This prevents undesired excitation of the chromophores and allows the effective suppression of this laser light in the detection path of the fluorescence microscope. For clarity, the laser and filter are drawn outside the piezo tube, while in reality they are placed inside the tube.

are extremely expensive, and since cantilevers are used in rather large quantities over time, the cost is an important factor. Because of these arguments, the optical beam deflection method is the best sensing method for the AFFM.

The optimal configuration of the scanning elements (see section 2.2.2) and the use of the optical lever method, allowed the design of the AFM to be adapted from the stand-alone AFM system which was previously developed in our laboratory (van der Werf *et al.*, 1993) (Fig. 2.5).

In order to prevent the previously mentioned problems of the optical lever method, a new diode laser was installed in our AFM with a wavelength of 1050 nm (Roithner Laser Technik, RLT106010MG). A similar approach was taken by Ebenstein *et al.* (2002). In addition a narrow bandpass filter (CVI Laser, F10-1050-4) was installed inside the AFM head which only transmits the 1050 nm emission peak and suppresses the typical sidebands of the diode laser emission (Fig. 2.6(a)). The advantage of using this laser wavelength in combination with the bandpass filter is two fold. First, it allows the use of the AFM in combination with essentially all fluorophores in the visible to near IR spectrum, without the AFM laser exciting the fluorescent molecules or overlapping with their emission spectra. Second, the narrow wavelength range, limited by the bandpass filter, makes it possible to effectively remove this light from the detection path of the fluorescence microscope by a suitable notch or low pass filter. This allows single molecule fluorescence detection extended to emission wavelengths in the near IR during operation of the AFM.

The base plate of the AFM tripod is widened in order to effectively span the sample scanning stage (Fig. 2.6(b)). Two legs of the AFM head are placed on two perpendicularly oriented translation stages which allows the coarse positioning of the AFM with respect to the optical axis of the confocal microscope. Fine adjustment of the tip

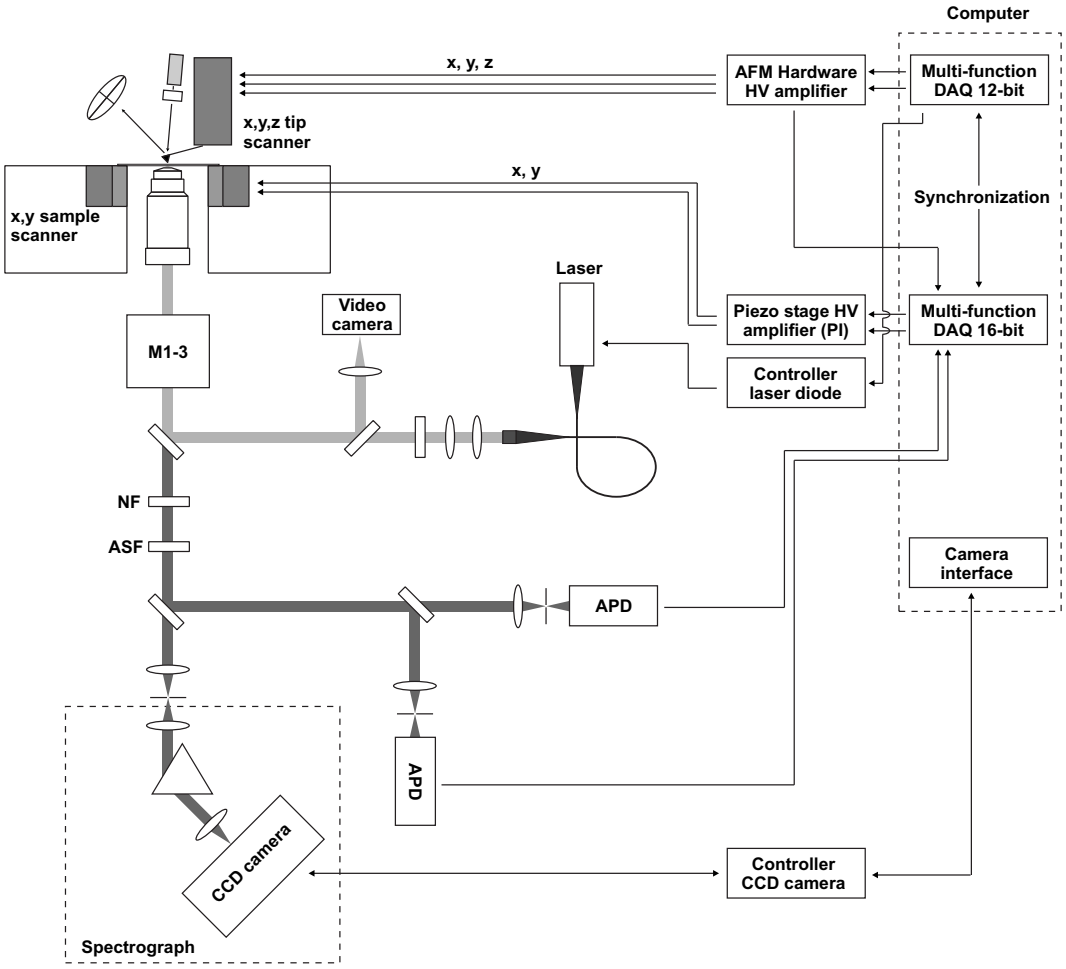

Figure 2.7. Schematic of the AFFM and the controllers and computer interface cards. In the detection path, an additional optical filter (ASF) is placed to suppress the AFM laser light collected by the objective.

position can be achieved using the piezo tube inside the AFM head. This tip scanner has a range of $3 \times 3 \times 1$ μm^3 in x,y,z directions respectively.

2.5 The AFFM

The atomic force microscope combined with the confocal fluorescence microscope is shown in Fig. 2.7, along with the controllers and the computer interface cards. The control- and data streams are schematically indicated as arrows.
The sample scanner and the tip scanner (piezo tube) are addressed independently. The sample scanner is controlled by the computer through a 16 bit multifunction data acquisition card (6052 E, National Instruments). The 16 bit resolution of this card makes it possible to scan the sample over the full range of 40×40 μm^2 with a minimum step size of 0.6 nm. The tip scanner is controlled through a 12 bit multifunction data

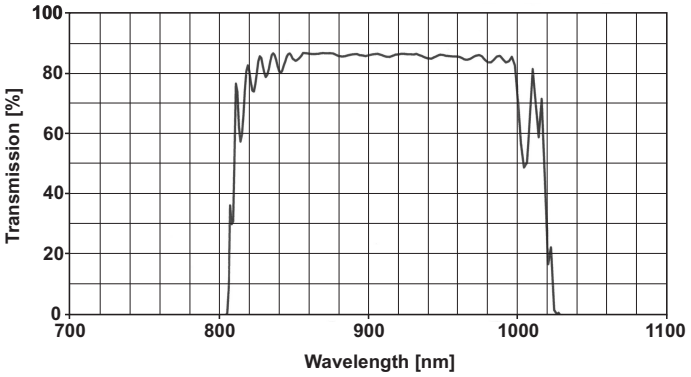

Figure 2.8. Transmission curve of the AFM-laser suppression filter. This filter was designed such that it also helps to suppress the 800 nm light from the fluorescence excitation laser.

acquisition card (MIO-16-E4, National Instruments), which allows a lateral step size of $\sim$ 0.6 nm. Both cards are synchronized using their real-time system integration (RTSI) bus. For acquisition of both AFM and APD data, the 6052E card is used because of its superior 16 bit analog to digital conversion compared to the 12 bit MIO-16-E4 card. The CCD camera controller is addressed through a high speed serial interface card (PCI-25, Roper Scientific) for control as well as data acquisition.

The AFM laser light which is collected by the objective is suppressed in the detection path of the CFM by a high quality bandpass filter (Fig. 2.8). In addition to the strong suppression of the 1050 nm light coming from the AFM, the filter also aids the suppression of the backscattered 800 nm excitation light. With this filter in the detection path, there is no residual optical background due to the AFM laser.

2.6 Modes of operation

The independent control of the sample- and the tip scanner allows the movement of the sample and the tip relative to the excitation volume and relative to each other. This results in a multitude of possible modes of operation, which can be realized on the software level. The AFFM is controlled by software written in our laboratory using National Instruments Labview. Software routines for new modes of operation can be flexibly added in a modular way. Several examples of these new modes are shown in Fig. 2.9. A number of modes that are realized in the software are described below.

Simultaneous topographic and optical imaging

In simultaneous fluorescence and topographic imaging mode the sample is scanned between the microscope objective and the AFM-tip. The vertical motion of the tip relative to the sample is induced by the piezo-tube inside the AFM in order to keep a constant deflection. Fluorescence and topographical information are collected simultaneously and are inherently spatially correlated.

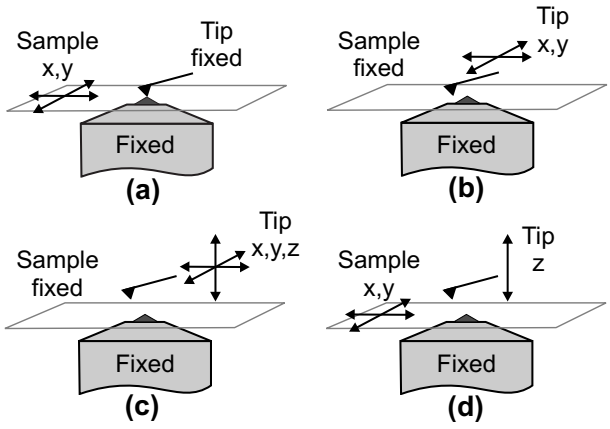

Figure 2.9. Different modes of operation: (a) Simultaneous imaging by scanning the sample between a fixed tip and a fixed focus; (b) AFM imaging by lateral tip scanning with a specific area (selected by positioning the sample stage) in the excitation volume; (c) Force-extension imaging with the tip moving in three dimensions; (d) Force-extension imaging with the tip ramping perpendicular to the surface and the sample moving in lateral directions. In mode (c) and (d) optical time-traces are recorded and stored along with the force-extension curves.

Combined AFM and spectral fluorescence imaging

The ability to perform spectral fluorescence imaging strongly enhances the chemical identification capacity of the instrument. In conventional spectral imaging, a complete fluorescence spectrum is measured for each pixel. Multiple fluorescent components can be easily distinguished even when their emission spectra partially overlap and separation into different detectors using dichroic beam splitters becomes very difficult. In order to obtain spectra with a sufficient signal-to-noise ratio, the accumulation time per pixel is usually in the order of 10 ms or more, depending on the fluorescence intensity. In AFM imaging the time per pixel is usually much lower, ranging from 0.2 to 0.5 ms. Because of this discrepancy, AFM and spectral images are recorded sequentially.

Combined optical and force extension measurements/nanomanipulation

The desirability of combined force spectroscopy and single molecule fluorescence measurements has already been addressed in literature (Wallace *et al.*, 2003; Weiss, 1999). For the measurement of mechanical properties of objects, interaction forces and adhesion forces, the so-called force-extension mode is often used. In this mode, the AFM tip is lowered towards the surface until it makes contact and a certain preset force is reached, after which the tip is retracted again. In this way, a force-extension curve is measured and stored for each image pixel. In our AFFM a fluorescence time-trace is recorded by the APD and stored along with the force-extension curve for each pixel. This type of imaging can either be done with the sample in a fixed location and with the tip moving in three dimensions (Fig. 2.9(c)), or by laterally scanning the sample and ramping the tip up and down (Fig. 2.9(d)). In general, this mode provides optical information from the sample as a function of the three dimensional position of the tip.

In a force-extension measurement, the maximum force that the tip exerts on the

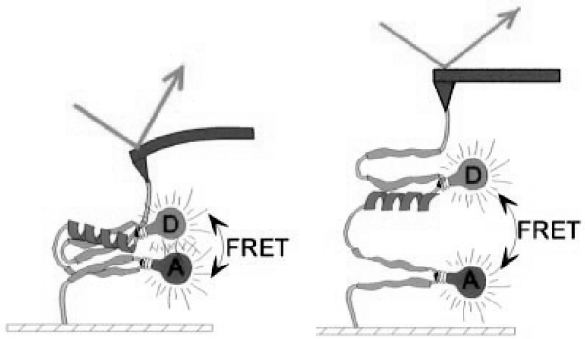

Figure 2.10. A combined fluorescence force-extension experiment as proposed by Weiss (1999). Mechanical unfolding of a protein combined with the recording of a single pair FRET. This figure was taken from Weiss (1999). The combined force extension mode enables this type of experiment.

sample is well controlled, and the optical response of a molecular system can be observed as a function of the applied force. An example of such a measurement, as proposed by Weiss (1999) is shown in Fig 2.10.

2.7 Conclusions

The combination between atomic force microscopy and confocal fluorescence microscopy provides detailed structural information about the specimen with high biochemical specificity. The additional information obtained by the combination of both techniques allows more reliable interpretation of measured data.
The AFFM presented in this chapter can perform truly simultaneous topographic and optical imaging with single molecule sensitivity. By shifting the AFM laser to a wavelength of 1050 nm, chromophores that have excitation and emission wavelengths anywhere in the visible to near-IR region can be used. The incorporation of fluorescence spectral imaging strongly enhances the chemical identification capability of the system.
The possibility to address the sample scanner and the tip scanner independently and synchronized with the optical detection results in a very flexible instrument, allowing many different types of experiments. The combined optical and force-extension mode provides the possibility to measure optical responses of the specimen as a function of a well controlled force.
These multiple imaging modes and the flexibility and modularity of the AFFM make it a powerful tool for bio-nanotechnology applications.

Chapter 3

High frequency laser current modulation

Atomic force microscopy measurements based on optical beam deflection can be seriously affected by two specific types of artifacts. Disturbances of the first type are caused by interference on the quadrant photodiode between the beam reflected directly from the cantilever and stray light from the sample surface. The second type is due to optical feedback effects caused by light scattering from the surface back into the laser cavity. In the AFFM, optical feedback induced instabilities caused serious disturbances during imaging. Interference effects were present as well. This chapter describes the application of high frequency laser current modulation to prevent optical feedback effects and to significantly reduce interference artifacts in AFM measurements. Residual noise is dominated by electronic and mechanical noise, shot noise and noise caused by the thermal motion of the cantilever. Additionally, a simple and compact high frequency modulator is described which enables the application of this technique in any AFM system.

3.1 Introduction

The optical beam deflection method is the most widely used sensing technique in atomic force microscopes (Meyer and Amer, 1988). In this technique, a light beam from a laser diode is focused on the back of a cantilever from which the beam is reflected towards a quadrant detector. A deflection or torsion movement of the cantilever results in a displacement of the light spot on the quadrant photodiode. Difference signals from the quadrant segments provide a measure for the cantilever position.
The signal to noise ratio in AFM is limited by mechanical and electronic noise, shot noise and noise caused by the thermal motion of the cantilever. In addition there is noise which is inherent to the optical beam deflection method itself. Two specific contributions to the latter form of noise can be distinguished. The first contribution is due to optical interference on the quadrant detector between the light that is reflected off the cantilever and the light scattered from the sample surface (situation A in Fig. 3.1). The second contribution is caused by optical feedback, when light is

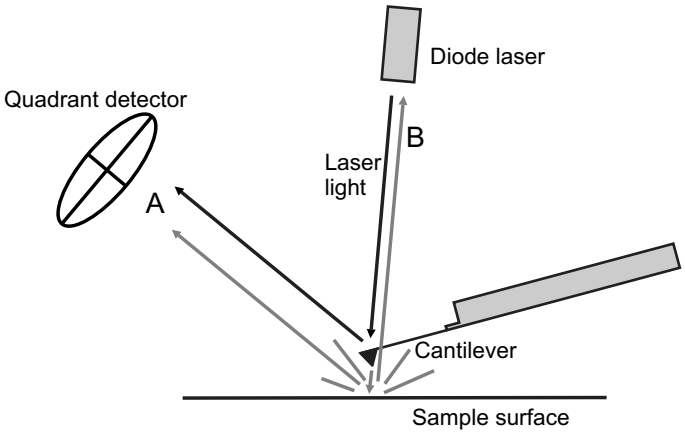

Figure 3.1. Schematic illustration of the causes of two artifacts related to the optical beam deflection method: A) optical interference on the quadrant detector; B) optical feedback in the laser cavity.

scattered back into the AFM laser cavity (situation B in Fig. 3.1).
Optical feedback effects appear in a wide frequency range and therefore seriously disturb AFM measurements in contact-mode, adhesion-mode and in tapping-mode imaging. This kind of noise is impossible to remove off-line. Optical interference artifacts can sometimes be removed using a procedure proposed by Méndez-Vilas *et al.* (2002), which is based on a Fourier transform technique. However, this technique is only successful when the fringes are confined to a narrow band in the spatial frequency domain. When the fringes take a more complex shape, these artifacts are also very difficult to remove off-line.
The presence of optical interference and optical feedback disturbances in AFM measurements can complicate interpretation of the measured data. Moreover, in situations when the AFM is operated in a feedback loop to maintain a constant imaging force, distortions in the deflection signals can be translated into real force fluctuations. Especially in the case of optical feedback in the laser cavity this can lead to large and rapid fluctuations in imaging force and even destruction of the sample when delicate biological material must be imaged.
In this chapter, it is demonstrated that although the mechanisms producing the optical feedback and interference effects are essentially very different, application of high frequency laser current modulation can reduce both effects in AFM measurements to a level where residual noise is dominated by the other noise sources mentioned above. Implementation of this method requires no alterations in the geometrical design of the AFM.

3.2 Experimental methods

The experiments were carried out with the AFM part of the AFFM instrument. All experiments were performed using a silicon nitride cantilever with a force constant of 0.01 N/m (Tip C, MSCT-AUHW, Veeco Microlevers, see appendix A). The images were acquired at 256 by 256 pixels with a pixel frequency of 2000 Hz. The force distance curves were measured by ramping the piezo-tube perpendicular to the surface over a range of 1080 nm at a frequency of 1 Hz. All measurements were taken in

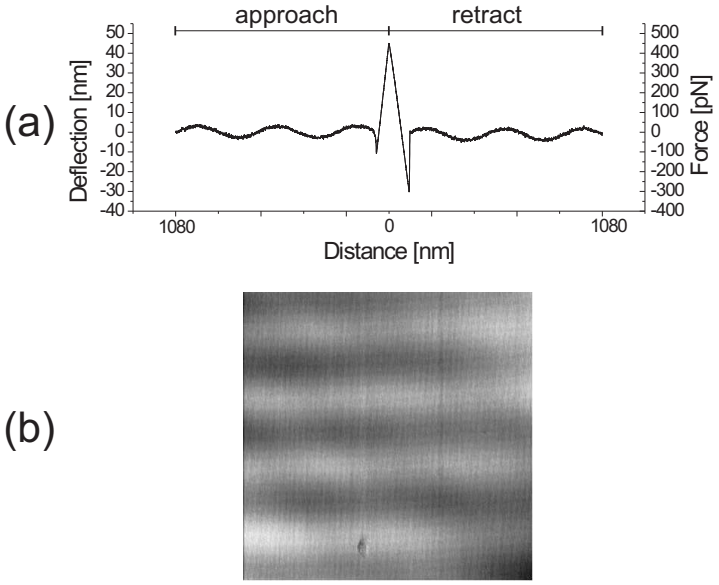

Figure 3.2. Examples of interference artifacts in AFM measurements. (a) Force-distance curve where a fringe pattern occurs. One complete cycle is shown over a distance of 1080 nm. The approach and retract phases are represented in a single curve (instead of superimposed) to clearly show the disturbing pattern. (b) Interference fringes in a 2D friction force image. The scan range in the image is 2.7×2.7 μm.

liquid (water) on a glass surface. The glasses were cleaned before the measurements by putting them in a solution of 60% HNO_3 for several days.

3.3 Artificial deflection and torsion signals in AFM measurements

3.3.1 Optical interference between the signal beam and stray light

The pattern of interference fringes on the quadrant detector depends on the optical path length difference between the stray light and the signal beam and therefore on the distance between the cantilever and the sample surface. Changes in the fringe pattern on the detector appear as deflection and torsion signals in AFM measurements. Maxima and minima in these signals will occur with a period of half the laser wavelength in optical path length difference. Changes in optical path length difference in the order of half the laser wavelength or more can occur due to large vertical movement of the cantilever e.g. in force distance type of AFM measurements, and lateral movement of the cantilever in 2D imaging modes.
Interference effects in force-distance curves are commonly observed (Weisenhorn *et al.*, 1992). An example is shown in Fig. 3.2(a). The presence of interference artifacts in force-distance curves causes several problems. First, the force set-point (the force at which the tip is retracted from the surface) is defined by a certain level in the deflection signal. When interference fringes cause large disturbances in the deflection signal, the minimal force set-point will be limited by these interference effects. This will complicate measuring small interaction forces, for instance on delicate biological samples. Second, due to an undefined baseline, the interpretation of force-distance curves is more difficult when interference patterns are present.

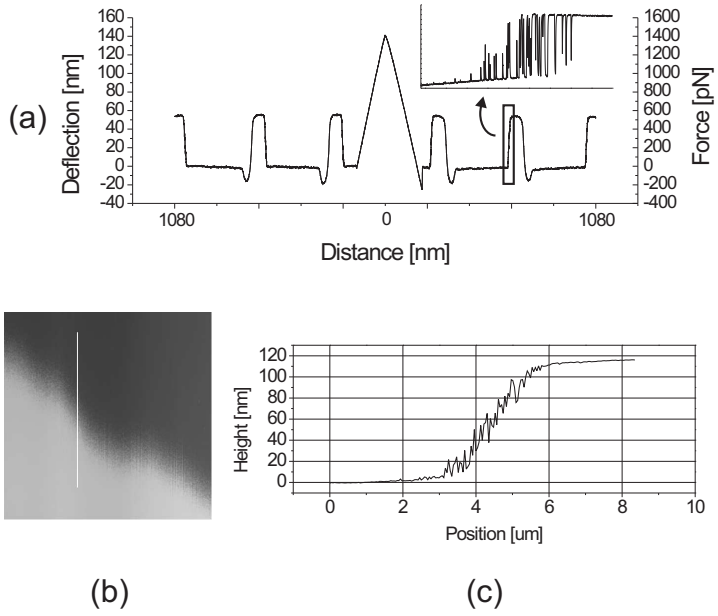

Figure 3.3. Examples of AFM measurements with optical feedback artifacts. (a) Force-distance curve showing dramatic jumps in the deflection signal when the laser makes a transition from one state to the next due to optical feedback. The inset shows high frequency jumps which are often observed during such a transition. (b) Height image disturbed by optical feedback effects. Also here the high frequency jumps during the transition are visible. A line trace through the image is shown in (c). In this case the image was acquired using a sample scanning stage over 11.2 × 11.2 μm.

The meaning of the effects in terms of nanometers deflection and forces depends on the properties of the particular cantilever used. In the case of Fig. 3.2(a) the interference fringes produce an artificial deflection signal during the approach with an amplitude of 6.13 nm corresponding to 61.3 pN.
Interference artifacts can also occur in 2D imaging due to the lateral motion of the cantilever. Disturbances in height images caused by interference are usually not significant, because their contribution is small compared to the height signals. In friction force measurements where the torsional movement of the cantilever is measured, the magnitude of the signal is much smaller and interference artifacts can become significant (Méndez-Vilas *et al.*, 2002; Reifer *et al.*, 1995). Fig. 3.2(b) shows an example of a friction force image on a glass surface in which the interference pattern is clearly visible.

3.3.2 Laser instabilities caused by optical feedback

Besides light scattered towards the quadrant detector, light can also be scattered back towards the laser diode, giving rise to optical feedback. When laser light is scattered back inside the cavity of a laser diode, the emission can become unstable causing sudden jumps in output power and fluctuations in the far-field pattern of the laser beam (Lang and Kobayashi, 1980). Both of these effects will appear as deflection and torsion signals in AFM measurements. The amplitude of optical feedback artifacts can be much larger than in the case of optical interference and can cause major problems. The conditions for optical feedback depend on the optical path length between the

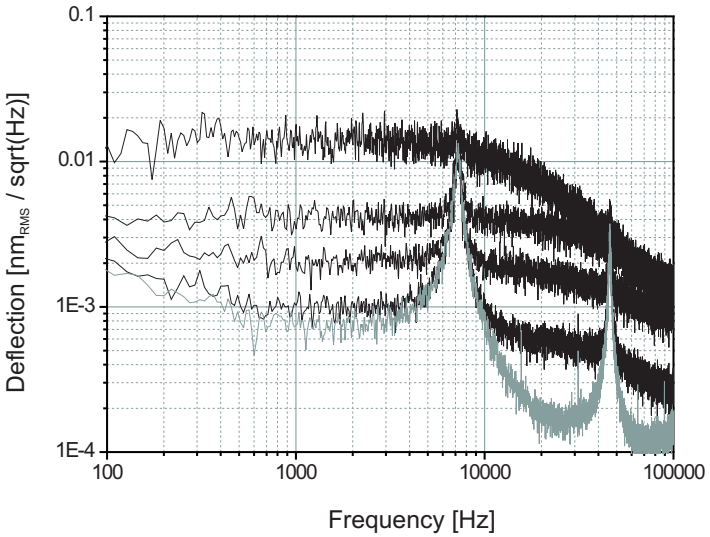

Figure 3.4. Frequency spectra of the deflection signal in air. The gray spectrum is taken in a situation without feedback. A low noise level is observed and the Brownian motion of the cantilever is clearly visible. The black spectra were measured under various levels of feedback. The noise level increases over the whole frequency range, up to levels were the Brownian motion of the cantilever is hardly observable.

laser and the external reflector (the sample surface). The fluctuations caused by optical feedback occur periodically with optical path length variation, with a period of half the laser wavelength (Lang and Kobayashi, 1980; Arimoto and Ojima, 1984). Therefore these disturbances will be present in force distance curves (Fig. 3.3(a)).

Sudden jumps in the deflection signal occur in the approach and retract curve. Depending on the amount of optical feedback, the amplitude of these jumps can become very large. The actual shape of the disturbances is different for each situation, but is always periodic with the distance between the laser and the sample surface with a period of half the laser wavelength. Similar to the situation with interference effects, the magnitude of the fluctuations in terms of nanometers and forces depends on the particular cantilever used. In the case of Fig. 3.3(a) the deflection signal fluctuated during the approach with an amplitude of 73.5 nm corresponding to 735 pN. In comparison with the example of optical interference (Fig. 3.2(a)), the artifacts due to optical feedback in Fig. 3.3(a) are more than 10 fold larger in amplitude, and can sometimes even be more dramatic.

Unlike in the case of optical interference on the quadrant detector, deflection fluctuations caused by optical feedback in the laser diode do produce serious disturbances in 2D height imaging (Fig. 3.3(b)), even though the distance between the laser and the surface does not change much. This is because large jumps in deflection can occur within a very small change in distance between the laser and the surface. In the case of the force-distance curve in Fig. 3.3(a) the deflection drops by 54 nm over a change in distance between laser and surface of only 13.6 nm. Therefore a minor and unavoidable tilt in the sample can cause a sudden jump in the deflection signal when such a transition region is crossed. During such a sudden transition of the laser emission from one state to the next, the laser tends to jump rapidly between the two states (Fig. 3.3(b), (c) and inset Fig. 3.3(a)). Spectral analysis of the deflection signal in air shows that the noise caused by optical feedback occurs throughout the whole

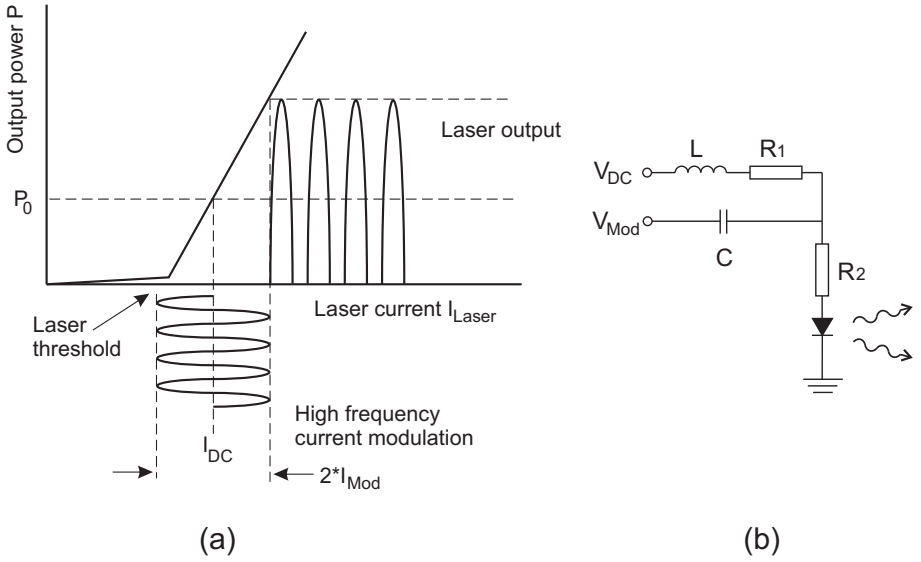

Figure 3.5. (a) The principle of high frequency laser current modulation $I_{Laser} = I_{DC} + I_{Mod} \times \sin(\omega t)$. It is important that the modulation crosses the threshold current. This figure was adapted from Ojima *et al.* (1986). (b) Scheme of the electronic circuit used to superimpose the high frequency modulation on top of the DC laser current: $L = 82$ μH, $R1 = 200$ Ω, $R2 = 50$ Ω, $C = 33$ nF.

bandwidth of the AFM system (DC to ∼300 kHz), and therefore also has a detrimental effect during tapping mode imaging. This is illustrated in Fig. 3.4. The gray spectrum was acquired in absence of feedback effects. A low noise level is observed with a clear peak at ~ 7 kHz corresponding to the Brownian motion of the cantilever at its resonance frequency (tip C, appendix A) and an second peak corresponding to a higher order cantilever oscillation. The black spectra were recorded under various levels of optical feedback. The noise increases over the whole frequency range, up to a level where the Brownian motion of the cantilever hardly be observed.

3.4 High frequency laser current modulation

3.4.1 The principle of laser current modulation

Interference and optical feedback are most profound in AFM systems using a single-mode diode laser, although they have also been observed in our laboratory in systems using a multi-mode laser. A single mode laser has a larger coherence length and will thus produce sharp interference fringes. The large coherence length makes it also more sensitive to optical feedback. A lower coherence length will therefore reduce both types of disturbances discussed in the previous section.
During several nanoseconds after turn-on, a single-mode laser will initially emit in a multi-mode state before the single-mode develops. When the diode laser current is modulated with a high frequency through the laser threshold current level, the laser

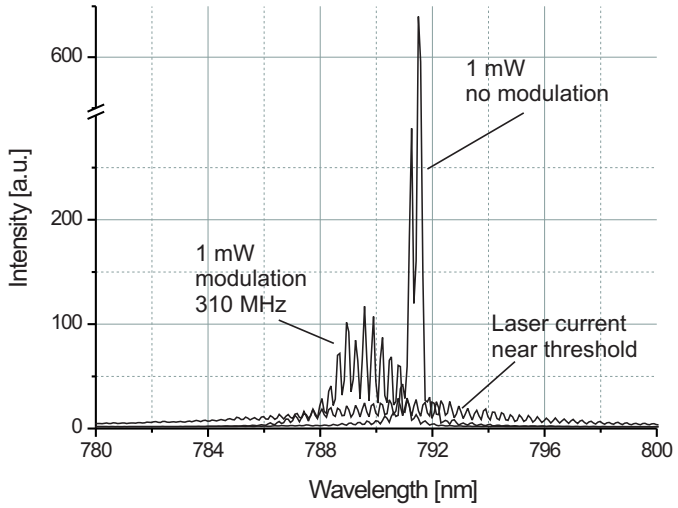

Figure 3.6. Emission spectra of the laser diode. The laser emits a broad spectrum with many modes when operated close to the laser threshold current. Upon normal operation with a DC current at 1 mW output power, two dominant modes are visible. When the modulator is switched on, the same optical power is emitted from multiple modes.

emission can be kept in a stable multi-mode state with a low coherence length (Lau *et al.*, 1984). This forced multi-mode emission state of the laser will eliminate optical feedback sensitivity and significantly reduce interference fringes. The application of this high frequency current modulation method in optical videodisc players has been described by Ojima *et al.* (1986) and Arimoto *et al.* (1986).
An illustration of the principle is presented in Fig. 3.5(a). The laser is operated at a DC current I_{DC}, on top of which a high frequency modulation current is superimposed. The amplitude of the modulation should be large enough to drive the laser through the threshold current during each oscillation. The average output power of the modulated laser is determined by the DC current and the modulation amplitude.

3.4.2 Laser emission under modulation

Spectral distribution

To test this modulation technique, the emission spectrum of a diode laser was measured with and without current modulation. The laser was modulated with a frequency of 310 MHz, using the electronic circuit of Fig. 3.5(b). The emission spectrum was measured with a monochromator with a spectral resolution of 0.08 nm using a blazed holographic grating with 600 grooves/mm (Jobin-Yvon, Paris, France). First, a DC current close to the laser threshold was applied without modulation (Fig. 3.6). In this case, the laser emits a multitude of modes. When the DC current was increased to a level where the laser emits 1 mW of light, the mode profile developed into one or two main peaks. Subsequently, the laser current modulation was switched on and the DC current was tuned such that again an average optical power of 1 mW was attained. The laser emission is clearly forced into a multi-mode state (Fig. 3.6). The same overall laser intensity is now distributed over a much broader emission spectrum.

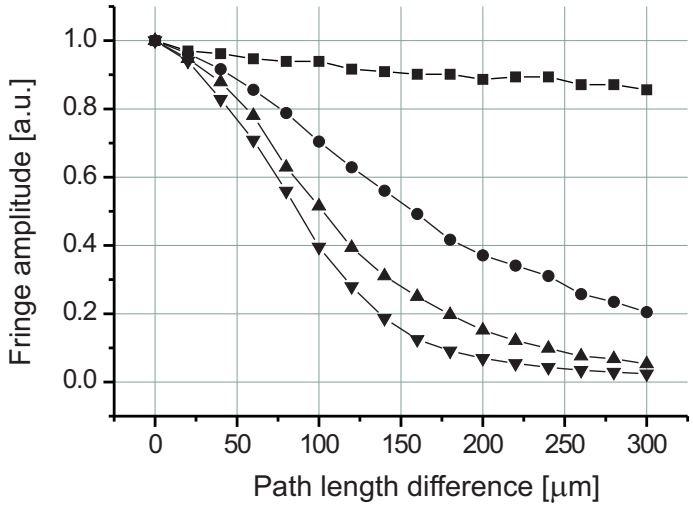

Figure 3.7. Interferograms of the laser emission under application of different modulation frequencies. From these curves the coherence lengths can be extracted, defined by the path length difference that corresponds to $1/e^2$ times the maximum fringe amplitude:

no mod	■	:	1058 μm
310 MHz	●	:	350 μm
640 MHz	▲	:	208 μm
925 MHz	▼	:	155 μm

Coherence length

Reduction of optical feedback and interference effects by high frequency current modulation relies on the decrease in coherence length of the emission. Due to the increased bandwidth of the laser under application of current modulation, the coherence length drops. Higher modulation frequencies result in a broader spectrum and a shorter coherence length. To investigate the amount by which it can be decreased, the coherence length was measured as a function of the modulation frequency. For this purpose, the laser beam was coupled into a Michelson interferometer in which the optical path length of one arm can be adjusted with respect to the other arm. By measuring the amplitude of the interference fringes as a function of the path difference between the two arms, the coherence length of the emission can be determined, defined by the path difference that corresponds to a fringe amplitude of $1/e^2$ times the maximum fringe amplitude. The modulation signals were generated by a high frequency function generator in order to vary the frequency.

Fig. 3.7 shows the interferograms acquired for different modulation frequencies. When no modulation is applied the coherence length amounts ~ 1 mm. Application of the 310 MHz modulation reduces the coherence length to 350 μm. The coherence length drops further when the frequency is increased, reaching a value of 155 μm at 925 MHz. However, the coherence length does not decrease as fast at higher frequencies. Therefore a further increase in modulation frequency above 925 MHz will not result in a significant decrease in coherence length. The exact minimal modulation frequency will be different for each laser. It should be sufficiently high in order to keep the laser emitting in a stable multi-mode state.

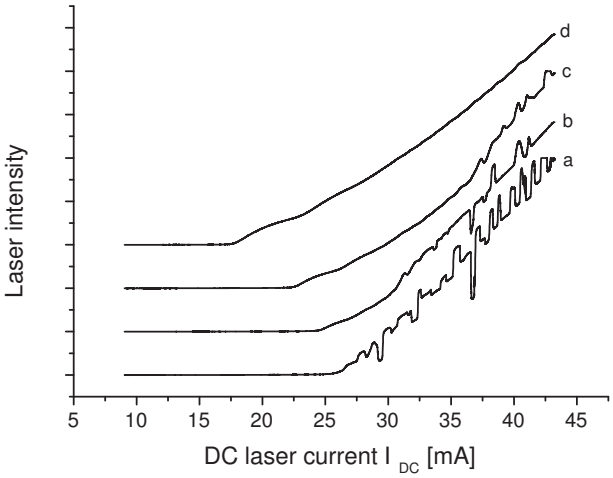

Figure 3.8. P-I curves with increasing modulation amplitude. For clarity the curves are displaced from each other. Curve (a) shows the jumps in laser intensity caused by optical feedback when no modulation is applied. Curves (b-d) show increasing stability with increasing modulation amplitude.

3.5 Application in the atomic force microscope

The high frequency laser current modulation technique was implemented in the AFM to monitor the improvements in an actual measurement situation. The results of these measurements will be discussed below.

3.5.1 Laser output stability

The effect of high frequency current modulation on the laser stability in an AFM situation with optical feedback is demonstrated in Fig. 3.8. A DC current (I_{DC}) sweep from 7 to 50 mA at 1 Hz was applied to the laser, on top of which a 500 MHz sine wave was superimposed with varying amplitude I_{Mod}. The output intensity was monitored by measuring the sum voltage from the quadrant detector in the AFM. Curve (a) shows the P-I diagram without current modulation. Sudden fluctuations in the output intensity occur due to optical feedback. The subsequent curves (b-d) were measured with high frequency modulation. With each curve, the amplitude I_{Mod} of the modulation current was increased. It is clear from curve (b) and (c) in Fig. 3.8 that the beginning of the P-I curves start to become smooth until the DC current is reached where the sine wave amplitude is not large enough to drive the laser through its threshold. This figure shows the importance of passing the laser threshold current with the high frequency modulation. For example, for a laser, which is operated at a DC current (I_{DC}) of 40 mA and with a threshold current of 25 mA, a modulation amplitude (I_{Mod}) larger than 15 mA should be superimposed in order to force the laser into a multi-mode emission state, eliminating its sensitivity to optical feedback.

3.5.2 Reduction of interference effects

To demonstrate the effect of the high frequency laser current modulation method in AFM measurements, force distance curves were measured in a situation with optical

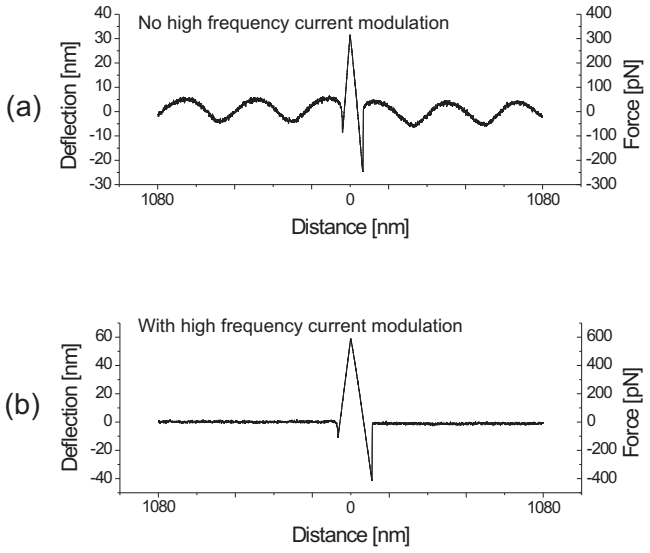

Figure 3.9. Application of the high frequency modulation method to a situation with optical interference. (a) Force-distance curve without laser current modulation. A clear interference pattern is present. (b) Force-distance curve in the same situation under application of a 500 MHz current modulation. The interference fringes disappear because of the forced multi-mode emission state of the laser.

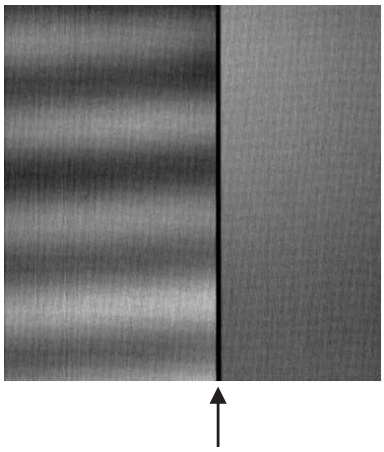

Figure 3.10. Friction force image of a glass surface. In the first part of the image interference fringes produce artificial friction signals. In the second part of the image, the high frequency modulation is switched on (indicated by the arrow) and the fringes disappear. The tip was scanned over 2.7×2.7 μm.

interference on the quadrant photodiode. Without the modulation, the force-distance curve of Fig. 3.9(a) was measured. An interference pattern with an amplitude of 9 nm corresponding to 90 pN is present in the approach and retract curve. When a 500 MHz current modulation was superimposed on the DC laser current, the interference pattern was suppressed to a regime where the residual noise is dominated by the other noise sources, mentioned before (Fig. 3.9(b)).

Also in friction force imaging, application of the high frequency modulation method effectively solves the problem of interference fringes in the image. In Fig. 3.10 it is demonstrated that the interference pattern disappears after switching on the high frequency modulation.

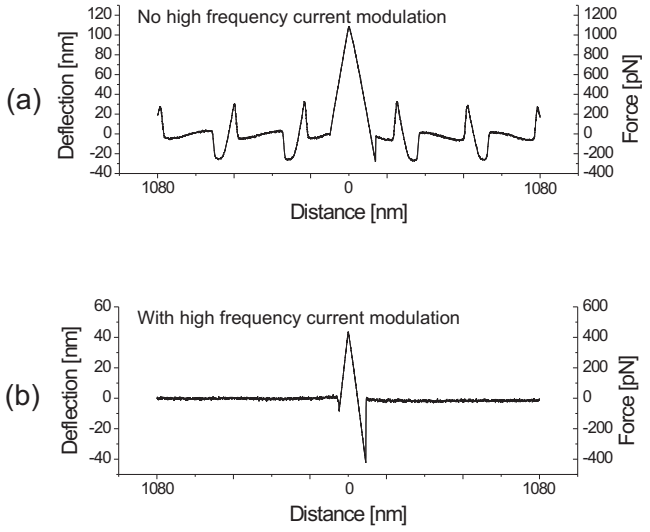

Figure 3.11. Application of the high frequency modulation method in a situation with optical feedback. (a) Force-distance curve showing sudden jumps in deflection during the approach and retract curve. (b) Force-distance curve in the same situation under application of 500 MHz modulation current. The forced multi-mode emission state of the laser makes it insensitive to optical feedback. The jumps have been completely eliminated.

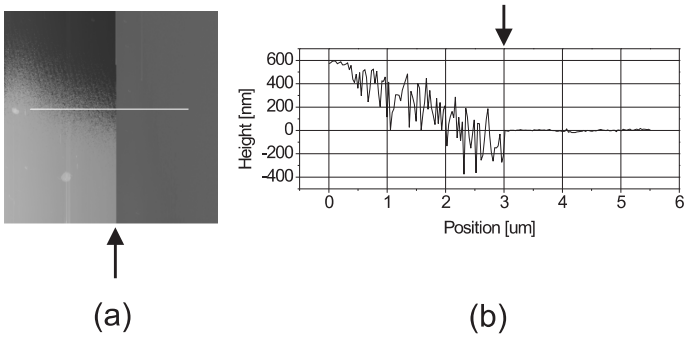

Figure 3.12. (a) Contact-mode image with artifacts due to optical feedback. In the first part of the image the disturbances are clearly visible. At the point indicated with the arrow, the high frequency current modulation is switched on and the artifacts disappear. This is further illustrated in the line trace in (b). This image was acquired using a sample scanning stage over 7.5×7.5 μm.

3.5.3 Elimination of optical feedback artifacts

The high frequency current modulation method was also applied in a situation with optical feedback artifacts. The effect of the method in a force-distance AFM measurement is shown in Fig. 3.11. The approach curve without high frequency modulation shows significant jumps in the deflection signal with an amplitude of 55 nm corresponding to 550 pN. When the high frequency modulation is switched on, the optical feedback artifacts are eliminated. The forced multi-mode state of the laser makes it insensitive to optical feedback. The residual noise is again dominated by the other noise sources.

The method of high frequency current modulation can also be successfully applied in 2D height imaging as is shown in Fig. 3.12. In the first part of the image optical feedback effects disturb the measurement. At the point indicated with the arrow the high frequency modulation was switched on and the image immediately becomes

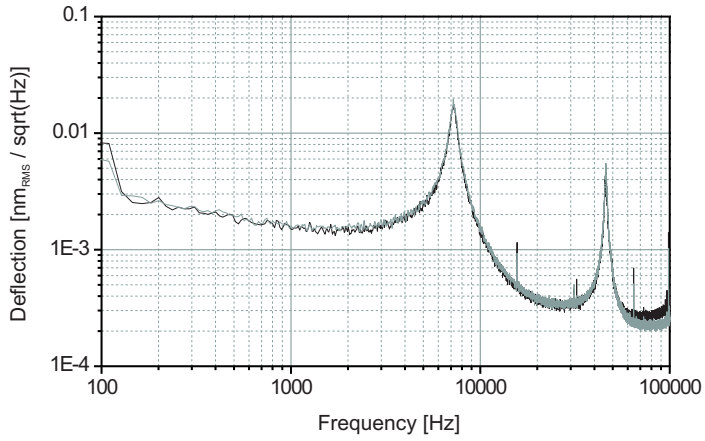

Figure 3.13. Frequency spectra of the deflection signal of tip C in air. The black spectrum was taken in a situation without optical feedback effects and no modulation. The gray spectrum was acquired with the oscillator switched on. There is clearly no increase in the noise level when laser current modulation is applied.

free of any artificial height signals. This is further illustrated by the line trace in Fig. 3.12(b). The height signals in the second part of the image are due to real topographic features.

3.5.4 No additional noise

Because of the high frequency used for the laser modulation compared to the bandwidth of the AFM system, the application of this technique does not add any additional noise to the measurements. This is illustrated in Fig. 3.13. The black curve shows the frequency spectrum of the deflection signal in a situation without optical feedback when no laser current modulation is applied. When the current modulation is switched on, no increase in the noise level is observed. Therefore, application of this technique has no negative side effects on the AFM performance.

3.6 A compact high frequency modulator

The laser current modulation technique can, in principle, be applied to any AFM system, without the need for any significant adaptations to the microscope. All that is required is a high frequency oscillator to be connected to the laser diode using a simple electronic scheme. However, suitable oscillators which can modulate the laser current with sufficient amplitude at a high frequency are not widely available. Specialized high frequency function generators are bulky and very expensive and therefore not suitable for the general application in AFM systems. In this section, the application of a compact oscillator, based on surface-acoustic-wave technology, is described. The oscillator is tested in combination with a 790 nm multi-mode diode laser, and subsequently the same oscillator-laser combination is tested in an AFM system.

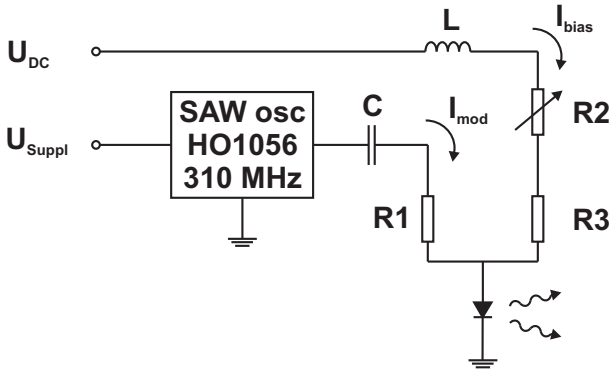

Figure 3.14. Scheme of the circuit used for driving the laser diode.

U_{DC}	=	12 V
U_{Suppl}	=	2-13 V
L	=	470 nH
C	=	560 pF
$R1$	=	47 Ω
$R2$	=	0 – 100 Ω
$R3$	=	470 Ω

3.6.1 Selection of a modulator

A suitable modulator for the general application of laser current modulation in AFM systems, has to meet three important criteria: (a) it has to be able to produce a peak-peak current modulation of 25 to 35 mA with a load impedance of 50 Ω in order to drive the laser through its threshold current with sufficient amplitude, (b) it has to oscillate at a frequency of 300 MHz or more, (c) it has to be small in order to fit inside or on the AFM head.
The RF-Monolithics Inc. #HO surface-acoustic-wave (SAW) oscillator series meets all three requirements. One out of this series, the HO1056 SAW oscillator with an oscillation frequency of 310 MHz was used for testing. The oscillator is located inside a compact sized metal case ($20.45 \times 12.83 \times 6.35$ mm). This RF oscillator produces a maximum output power of +13 dBm with a 50 Ω load impedance. This corresponds to a maximum current modulation of 56.6 mA peak-peak. The modulation amplitude increases linearly with increasing DC supply voltage (0-13 V) applied to the oscillator, and can therefore simply be tuned.

3.6.2 Implementation in the AFM head

The electronic scheme used to drive the laser diode is shown in Fig. 3.14. The DC bias current of the laser diode can be varied between 20 and 25 mA by controlling the potentiometer R2. The modulation current is superimposed on the DC current. A miniature coaxial cable (50VMTX) was used to connect the oscillator to the laser diode. This type of cable is suitable for use up to 3 GHz, and has a characteristic impedance of 50 Ω. In order to match the impedances of the oscillator (50 Ω), the cable and the total load of the oscillator, a resistor R1 of 47 Ω is placed in series with the laser diode (3 Ω). The condition of impedance matching assures that the modulation signal is transferred without reflections, so that all power is transferred from the oscillator to the laser diode.
The many different AFM designs will often not allow a direct connection of the modulator to the laser diode. Therefore, the emission spectrum of the laser has been tested for different lengths of the coaxial cable connecting the modulator and the laser. Although the effective modulation amplitude drops somewhat with increasing cable length, the same broad emission spectrum is measured with cable lengths up

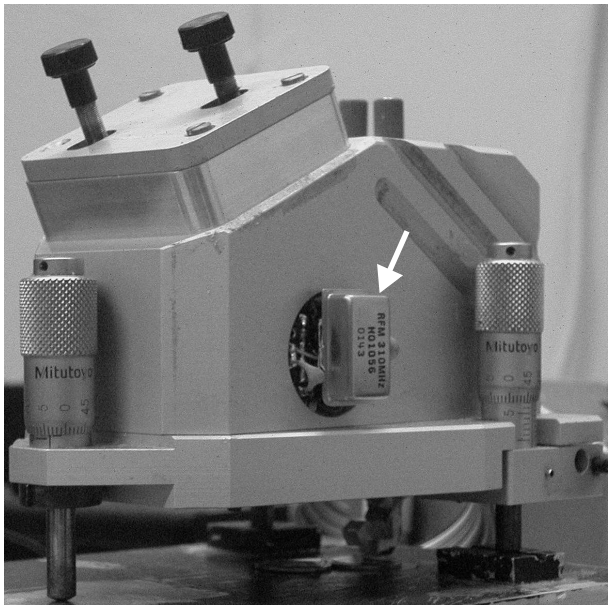

Figure 3.15. HO1056 310 MHz SAW oscillator mounted externally on the AFM head. A small printed circuit board with the components L1 and R1-3 is directly connected to the laser inside the piezo tube. The modulator is connected to the printed circuit board with a 10 cm miniature coaxial cable.

to 24 cm. This permits the location of the modulator somewhere on the AFM head where the geometry is suitable, and only the small diameter coaxial cable has to enter the head to be connected to the laser diode.

The components L1, and R1-3 are placed on a small printed circuit board, directly connected to the laser diode inside the piezo tube (See Fig. 2.5 chapter 2). The oscillator is mounted externally on the AFM head in an IC-socket, which allows the exchange of this module for a module with a different frequency (Fig. 3.15). The coaxial cable connecting the oscillator and the small printed circuit board on the laser, has a length of 10 cm.

3.6.3 Elimination of optical feedback and reduction of interference

The implemented modulator was tested in a force-extension experiment. In order to perform the test in a worst case situation with a large amount of scattered light, a gold sample was taken as a substrate. In Fig. 3.16, a part of an approach curve is shown before the tip touches the surface. The black curve shows large sudden jumps due to strong optical feedback. In addition, interference fringes are observed with significant amplitude. When the oscillator is switched on (gray curve), the optical feedback effects have completely disappeared. The interference artifacts in the deflection signal are reduced with a factor of 5. The #HO SAW oscillator series consists of modulators with frequencies of 310, 400, 640, 700 and 750 MHz. Application of a module with a higher modulation frequency will decrease the interference effects even more. Note however that AFM measurements are generally performed on a mica or glass substrate where the amount of scattered light will be lower.

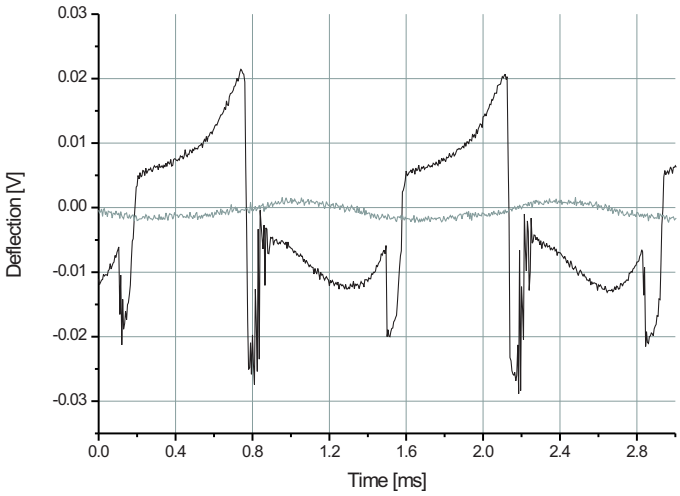

Figure 3.16. Part of an approach curve in a force extension measurement on a gold substrate. In the black curve, without current modulation, interference and optical feedback effects are strongly present. The grey curve shows the same approach curve when the modulation is switched on. Optical feedback artifacts are eliminated and interference effects are strongly suppressed.

3.7 Conclusions

A method of high frequency laser current modulation has been applied to AFM measurements in situations with optical interference as well as with optical feedback. The experimental results show that application of the method provides a simple and effective method to reduce both artifacts to a level where residual noise is dominated by mechanical and electronic noise, shot noise, and noise caused by the thermal motion of the cantilever. No additional noise is introduced by this technique.
Application of this method prevents uncontrolled fluctuations in imaging forces and removes the necessity to subtract disturbances in measured data off-line, which is in general laborious, difficult, and sometimes impossible. Interpretation of the data is not complicated by artificial signals generated by optical interference and optical feedback artifacts when the high frequency laser current modulation method is applied.
Implementation of this method does not require any geometric alterations in the AFM system. The compact SAW modulator can be mounted on the AFM head itself. Since the method is based on general properties of laser diodes it is applicable in any AFM system with diode lasers of any wavelength.

Chapter 4

Performance of the AFFM

For the design of the AFFM, a number of strict requirements were defined. The confocal microscope should be capable of detecting single molecule fluorescence in the near infrared part of the spectrum, since the light harvesting complexes emit at wavelengths of 870 nm (LH2) and 890 nm (LH1). Additionally, the AFM laser should not excite the molecules or produce a large optical background signal. Furthermore, the combination of the AFM with the fluorescence microscope should not compromise the ability to measure topography with a high resolution. In this chapter, these aspects will be treated and the performance of both microscopes will be demonstrated on individual light harvesting complexes as well as on 2 dimensional crystals of LH1 and LH2 complexes.

4.1 Performance of the confocal fluorescence microscope

The ability to detect fluorescence with single molecule sensitivity is a matter of creating a high detection efficiency combined with strong background suppression. This can be achieved by minimizing the number of optical components in the microscope and careful selection of those components necessary. Additionally, the use of sensitive detectors with a low noise level is crucial. In this section, the background levels and the detection efficiency of the confocal microscope will be treated and the sensitivity will be demonstrated by measurements performed on individual light harvesting complexes.

4.1.1 Detection efficiency

The detection efficiency of the fluorescence microscope can be calculated from the collection angle and transmission of the objective and reflection and transmission values of all components in the detection path. The values mentioned below were taken for wavelengths between 850 and 900 nm, the emission range of the LH complexes.

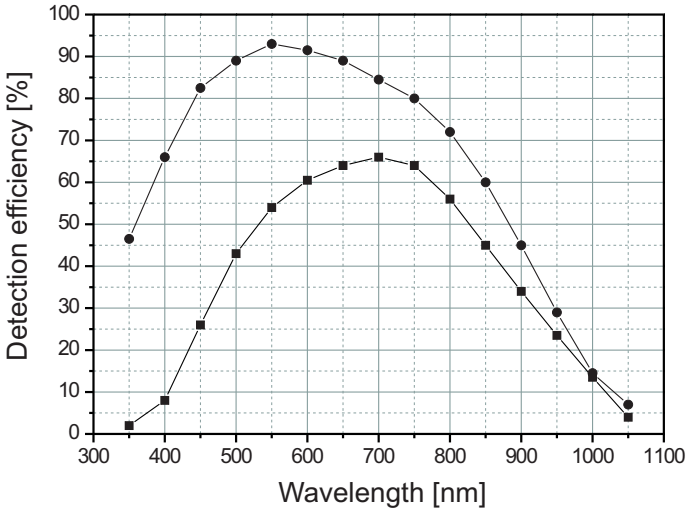

Figure 4.1. Detection efficiency of the APD (■) and CCD camera (●) as a function of wavelength. The values for the detection efficiency were taken from data sheets of Perkin Elmer and Roper Scientific.

$$\eta_{common} = \eta_{NA} \cdot T_{obj} \cdot (R_M)^3 \cdot T_{BS2} \cdot T_{NF} \quad (4.1)$$

$$\eta_{APD\ det} = \eta_{common} \cdot R_M \cdot T_L \cdot \eta_{APD} \quad (4.2)$$

$$\eta_{Spec\ det} = \eta_{common} \cdot (T_L)^2 \cdot T_{prism} \cdot T_L \cdot \eta_{CCD} \quad (4.3)$$

where η_{common} represents the efficiency of the part of the detection path which is common for both APD detection and spectrograph detection, $\eta_{APD\ det}$ represents the total detection efficiency for APD detection and $\eta_{Spec\ det}$ the total efficiency for spectrograph detection. Furthermore:

η_{NA}	: collection eff. objective	$= 0.24$
T_{obj}	: transmittance objective	$= 0.80$
R_M	: reflectance mirrors M1-4	$= 0.95$
T_{BS2}	: transmittance dichroic beam splitter BS2	$= 0.95$
T_{NF}	: transmittance notch filter NF	$= 0.83$
T_L	: transmittance lenses L1-4	$= 0.98$
η_{APD}	: detection efficiency APD	$= 0.40$
T_{prism}	: transmission dispersing prism	$= 0.74$
η_{CCD}	: detection efficiency CCD-camera	$= 0.52$

The detection efficiencies of the APD and the CCD camera strongly depend on the wavelength (Fig. 4.1). In general the detection efficiency of silicon based detectors drops for near IR wavelengths.
Substituting these values in Eq. 4.2 and Eq. 4.3 results in:

$$\eta_{APD\ det} = 4.8\ \%$$
$$\eta_{Spec\ det} = 4.7\ \%$$

4.1.2 Noise sources

The detection of very low light intensities requires a low noise level. The four main noise sources present in the fluorescence measurements are:

- Photon noise (shot noise)
- Thermal noise (dark current noise)
- Readout noise
- Noise from background sources

Photon noise

Photon noise (or shot noise) refers to the inherent natural variation of the incident photon flux. The total number of photons emitted by a steady source over any time interval varies according to a Poisson distribution. The root mean square (r.m.s.) variation in the number of emitted photons is given by:

$$\sigma_{ph} = \sqrt{N} \tag{4.4}$$

where N is the average number of photons emitted per unit time. This form of noise is always present in optical measurements.

Thermal noise

Electron-hole pairs can be generated in absence of any light through thermal agitation. Electrons freed in this way are indistinguishable from 'true' photoelectrons. The random thermal generation of electrons also follows a Poisson distribution, and therefore the r.m.s. thermal noise level σ_{th} is given by the square root of the dark current.
The SPCM-AQR-14 APD's (Perkin-Elmer Optoelectronics) are thermoelectrically cooled and temperature controlled to obtain a stable and low dark count rate. The specified dark count level of the APD's is < 100 cnts/sec, leading to a thermal noise level of < 10 cnts/sec. The CCD camera (Spec-10:100B, Princeton Instruments) is cooled to -120°C using liquid nitrogen to minimize the dark current. The specified dark current at -120°C is 0.3 electrons/pixel/hour. For integration times up to a few hundred milliseconds in typical fluorescence measurements, the dark current noise for the CCD camera is negligible.

Readout noise

Readout noise is only present in measurements using the CCD camera. This type of noise refers to the uncertainty introduced during the process of quantifying the electronic signal on the CCD, the major component of which arises from the on-chip preamplifier. CCD readout noise is added during each readout event and in normal operation, readout noise will be added to each pixel. However, when pixels are binned, readout noise is added to each 'super-pixel' which has the combined signal from multiple pixels. In the ideal case, this produces an improvement in signal-to-noise ratio equal to the binning factor. In spectroscopic measurements the different wavelengths are spread in horizontal direction on the CCD chip, and full vertical binning can be applied. The exact readout noise level is dependant on the exact hardware setting for a certain experiment, but a reasonable estimation for this noise level σ_{ro} is 3.5 electrons/pixel.

Noise from background sources

In addition to the previously mentioned noise sources, background light sources can also contribute to the total noise level. Examples of these background sources are back scattered excitation light, weak luminescence from the sample substrate, and collected AFM laser light in the case of combined operation.

When the 800 nm excitation light is focussed on the glass liquid (water) interface to excite the specimen, the back scattered fraction of this light is removed from the detection path by a narrow band holographic notch filter (HNPF-800, Kaiser Optical Systems) with a transmission of $< 10^{-6}$ at 800 nm. The detected background level for APD detection in this situation increases to about $\sim$ 200 cnts/sec, 100 cnts/sec above the dark current level. Part of this increased background level can be attributed to weak luminescence from the glass substrate. The additional r.m.s. noise σ_{bg} due to these sources is consequently 10 cnts/sec.

Another potential source of background signal in APD measurements is the AFM laser light collected by the objective in combined experiments. To prevent spectral overlap of this laser light with fluorescence emission of the specimens, a laser is used with a wavelength of 1050 nm. This allows the selective suppression of the laser wavelength in the detection path. An additional advantage of this wavelength is the reduced detection efficiency of the APD at this wavelength ($\sim$ 5 %). When cantilevers without reflective coating are used a substantial amount of light passes through the cantilever. Without the suppression filter, this light saturates the detectors. Application of the AFM laser suppression filter reduces the background to $\sim$ 3000 cnts/sec in this case. However, the commonly used cantilevers are coated on the back side with a thin reflective gold layer. With this type of cantilevers and the presence of the suppression filter, the total background hardly increases above 200 cnts/sec.

Since the wavelengths of the excitation laser and the AFM laser are spectrally well separated from the emission bands of the specimen, residual background from these sources does not add significant noise to the pixels detecting the fluorescence signal in

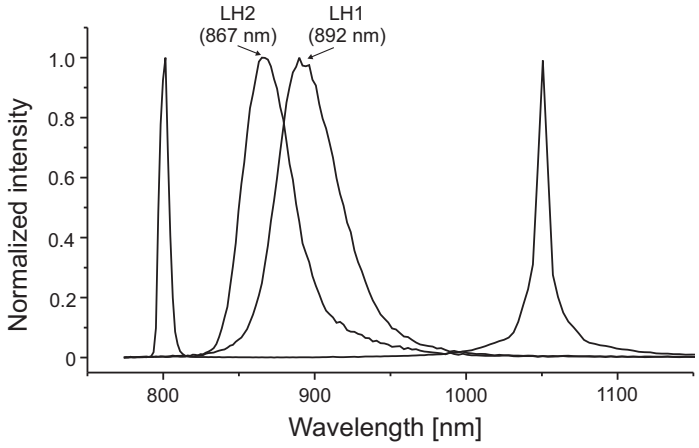

Figure 4.2. Spectral distribution of the excitation wavelength at 800 nm, the AFM laser at 1050 nm and the emission spectra of purified LH1 and LH2 complexes with emission peaks at 892 nm and 867 nm respectively.

spectrally resolved measurements. The spectral distribution of the excitation wavelength, the AFM laser wavelength and the LH1 and LH2 emission bands is shown in Fig. 4.2. Comparison of the spectral emission shapes of the LH1 and LH2 complexes with and without the presence of the 800 nm notch filter and the AFM laser suppression filter showed that these filters do not affect the emission profiles (data not shown).

Signal-to-noise ratio

In general, the signal-to-noise ratio for fluorescence detection is given by:

$$S/N = \frac{A_{sign}}{\sigma_{noise}} = \frac{S\eta_{det}t}{\sqrt{\sigma_{ph}^2 + \sigma_{th}^2 + \sigma_{ro}^2 + \sigma_{bg}^2}} \tag{4.5}$$

where S is the fluorescence emission rate (# photons/sec), η_{det} is the total detection efficiency (η_{APDdet} in case of APD detection and $\eta_{Specdet}$ in case of spectral detection), t is the measurement time interval, and σ_{ph}, σ_{th}, σ_{ro} and σ_{bg} are the r.m.s. levels of the photon noise, thermal noise, readout noise and background noise.

4.1.3 Sample preparation

In order to immobilize the LH complexes on the surface of a coverglass, the glass surface was coated with poly-L-lysine (PLL Hydrobromide, Sigma). This polymer of lysines has a net positive charge at neutral pH, and binds to the slightly negatively charged glass surface by electrostatic interaction. The largely negatively charged N-terminal regions of the LH2 apoproteins subsequently bind electrostatically to the coated surface.

The glasses (#1, thickness 170 μm, $\varnothing$ 24 mm, Menzel-Gläser, Braunschweig, Germany) were extensively cleaned in 65 % HNO_3 under sonication for $\sim$ 15 min. After

sonication the glasses were stored in the acid solution. Before addition of the coating, the glasses were taken from the acid solution and thoroughly rinsed with deionized water. The glasses were coated by submerging them in a solution of 0.01 % PLL for more than 1 hour. Before use, they were again rinsed with deionized water and dried. The purified LH2 complexes from the photosynthetic bacterium *Rhodobacter sphaeroides* are stored in a buffer solution [50mM TRIS (pH 7.8), 50mM NaCl, 0.1 % lauryldimethylamine oxide (LDAO)]. The detergent LDAO is needed in order to solubilize the complexes. This solution was diluted in the same buffer by a factor of 10^4 in three steps. A 6 μL drop of the diluted sample was spread out on the PLL coated coverslip. After 2 minutes adsorption time, the glass was rinsed with $\sim$ 0.5 mL of buffer. An amount of $\sim$ 10 μL of buffer was added after rinsing and the sample was closed with a top coverslip and mounted on the confocal microscope of the AFFM.

4.1.4 Fluorescence imaging

Fig. 4.3 shows confocal fluorescence images of individual LH2 complexes. The images were recorded with 128×128 pixels, using $\sim$ 6 μW excitation intensity at 800 nm in images (a) and (b), and $\sim$ 2 μW at 488 nm excitation in (c) and (d). The integration time per pixel was 2 ms in Fig. 4.3(a), (c) and (d) and 1 ms in Fig. 4.3(b). Even though the LH2 complex contains a multitude of chromophores, the emission of the complexes shows characteristics similar to a single chromophore such as blinking (molecule 1) and single step photobleaching (molecule2) in Fig. 4.3(a). Due to the rapid transfer of excitation energy within the complex towards the B850 ring, most of the observed dynamics originates from this group of pigments. Spots 3 and 4 in Fig. 4.3(a) show aggregates of various amounts of complexes. Fig. 4.3(b) shows a fluorescence image of individual LH2's with a smaller scan range, also clearly showing the blinking and bleaching behavior.
The near-IR fluorescence from LH2 complexes can also be observed when the carotenoids of the complexes are excited using light with a wavelength of 488 nm. Images recorded with 488 nm excitation are shown in Fig. 4.3(c) and (d). The emission of the complexes still occurred at 870 nm from B850, caused by the efficient energy transfer between the pigments in the complex. The fact that the emission still originates from B850 is indicating that the molecules are intact on the surface.
The lateral resolution of the microscope is determined by the size of the excitation spot. The diffraction limited radius r of a focus for a Gaussian beam is given by

$$r = \frac{K\lambda_0 f/\#}{2n} \tag{4.6}$$

where K is a truncation constant, λ_0 is the free space wavelength, n is the refractive index of the medium and $f/\#$ is a measure of the relative aperture of a lens, its light gathering power, given by

$$f/\# = \frac{f}{D} \tag{4.7}$$

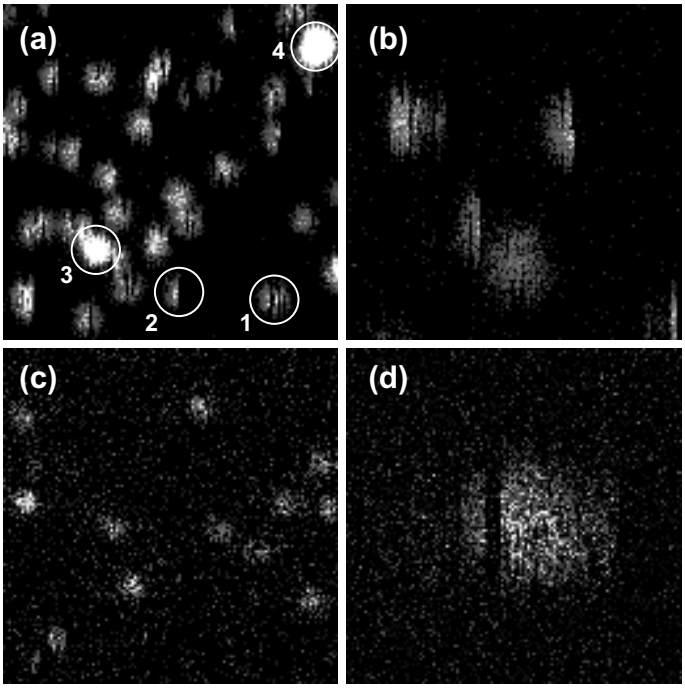

Figure 4.3. Confocal fluorescence images of individual LH2 complexes. (a) Overview of 6.3×6.3 μm^2. Spots 1 and 2 show blinking and single step photobleaching behavior typical of single chromophore emission. Spots 3 and 4 are examples of aggregates of various amounts of LH2 complexes. (b) Zoom in of 3.0×3.0 μm^2. Also this image clearly shows the blinking and bleaching behavior. (c), (d) Images of single LH2 complexes excited with 488 nm. The scan ranges are 7.7×7.7 μm^2 and 1.5×1.5 μm^2 respectively.

where f is the focal length of the lens and D is the diameter of its aperture. When the spot radius is determined at $1/e^2$ intensity level, the truncation factor should be set to $K = 1.83$. Substituting $f/\# = n/(2NA)$, where NA is the numerical aperture of the objective, the final expression for the radius of the beam waist in the focus of the objective becomes

$$r = \frac{1.83\lambda_0}{4NA} \tag{4.8}$$

Consequently, the maximum obtainable lateral resolution, using an oil immersion objective with NA 1.3, is 563 nm for 800 nm excitation and 344 nm for 488 nm excitation.

4.1.5 Fluorescence timetraces and the influence of oxygen

After localization of the complexes by recording a fluorescence image, one of the complexes can be selected and positioned in the focus of the objective and subsequently the fluorescence can be recorded over time, using the APD's, upon continuous illumination. When a large number of complexes is located in the focus (e.g. in spot 4 in Fig. 4.3(a)), the recorded timetrace of fluorescence intensity versus time features an exponential decay caused by a gradual photobleaching of the assembly of complexes (Fig. 4.4(a)). An aggregate of just a few complexes (e.g. in spot 3 in Fig. 4.3(a)) results in a timetrace with the single step behavior of the individual proteins clearly visible (Fig. 4.4(b)). A timetrace of a single complex can be recognized by the intensity of the emission as well as the appearance of discrete intensity steps down to

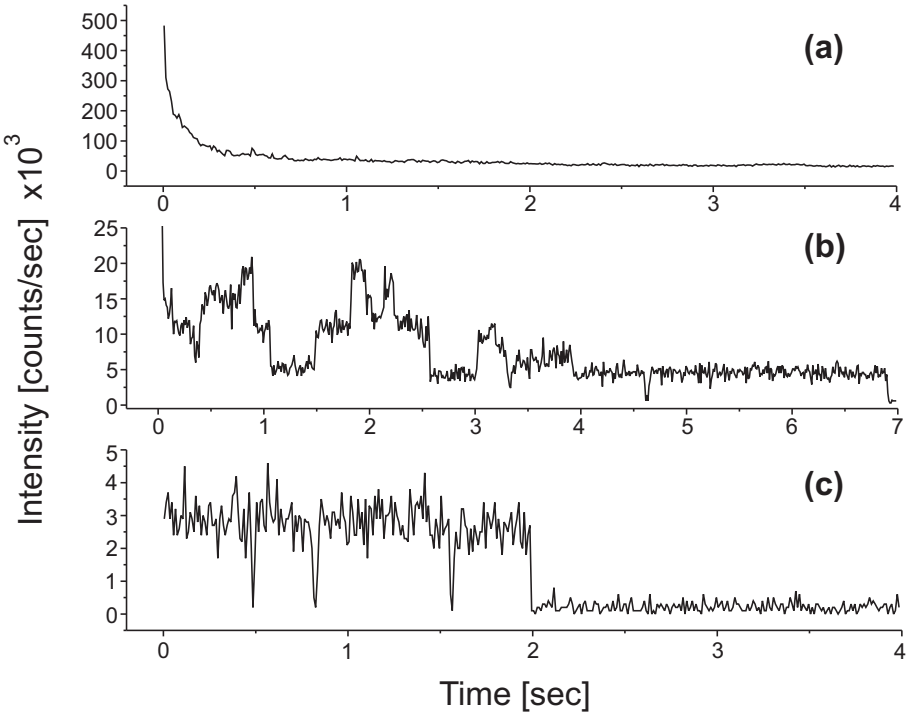

Figure 4.4. Fluorescence timetraces with various numbers of molecules in the excitation focus. (a) Timetrace of a large assembly of molecules (e.g. in spot 4 in Fig. 4.3a). (b) Timetrace with a few molecules in the focus (e.g. in spot 3 in Fig. 4.3a). (c) Single molecule timetrace.

the background level such as demonstrated in Fig. 4.4(c). After a few seconds the complexes photobleach and no further emission is observed.

Photobleaching often occurs through the reaction of a chromophore with oxygen species. The ground state triplet oxygen ($^3O_2$) is not very reactive, but can become activated by energy transfer from an excited state triplet chromophore to form the highly reactive singlet oxygen ($^1O_2^*$), which can in turn harm the chromophores. In the case of LH2, a singlet excited Bchl may convert into a triplet state with a yield of 2-15 % (Cogdell *et al.*, 1981; Monger *et al.*, 1976). This triplet, with a lifetime of 70 μs, can transfer its energy to triplet oxygen to form singlet oxygen. However, the carotenoids in LH2 protect the complex against this process by efficiently quenching the triplet Bchl within $\sim$ 20 ns (Angerhofer *et al.*, 1995), thereby forming a triplet-excited carotenoid. The energy level of this triplet carotenoid is lower than that of singlet oxygen, which prevents the formation of singlet oxygen from the carotenoid triplet itself. Schematically:

$$\text{Bchl} + h\nu \longrightarrow {}^1\text{Bchl}^* \longrightarrow {}^3\text{Bchl}^*$$
$${}^3\text{Bchl}^* + \text{O}_2 \dashrightarrow {}^1\text{O}_2^* + \text{Bchl}$$

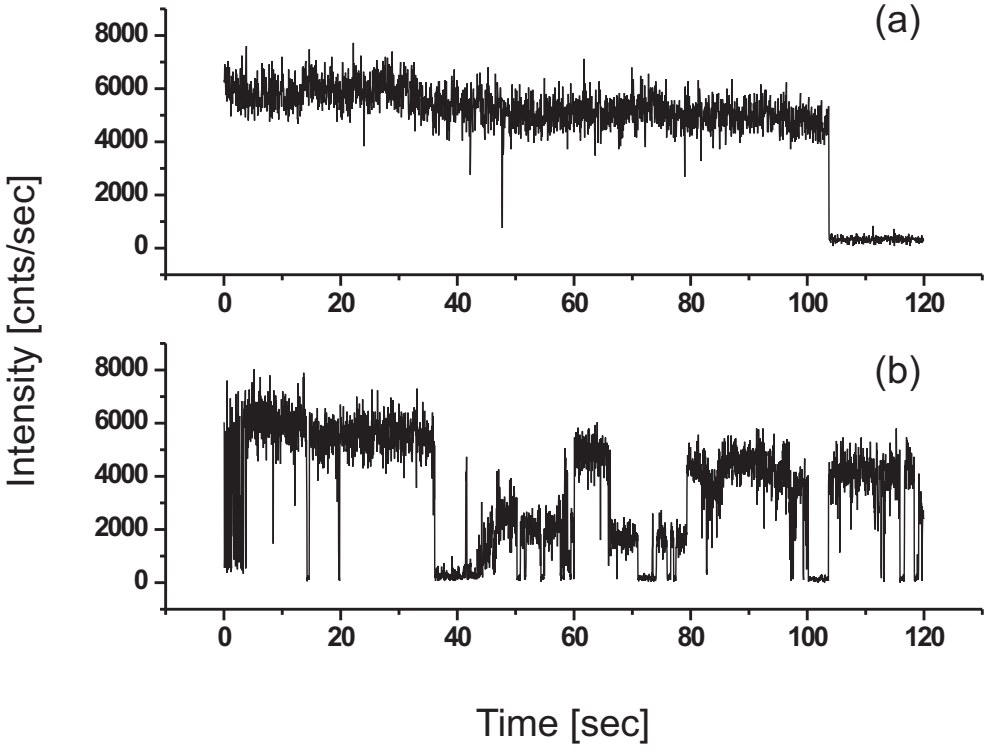

Figure 4.5. Fluorescence timetraces of single LH2 complexes recorded in the absence of oxygen. The molecules emit over much longer timescales when no oxygen is present. (a) This trace shows no dynamics and the molecule bleaches after $\sim$ 103 sec. (b) Much more dynamics is observed in this trace. After 2 minutes still no photobleaching has occurred. Oxygen was removed from the sample by addition of an oxygen scavenging system containing glucose, glucose oxidase and catalase.

or

$$^3\text{Bchl}^* + \text{Car} \longrightarrow {}^3\text{Car}^* + \text{Bchl}$$
$$^3\text{Car}^* \longrightarrow \text{Car} + \text{Heat}$$

The dashed arrow symbolizes the fact that this step is very unlikely because of the efficiency of triplet quenching by the carotenoids. Therefore, the formation of singlet oxygen is not the main threat for the LH2 complex. However, oxygen can also be activated by electron transfer from a singlet excited chromophore, thereby oxidizing the chromophore. Because of the rapid excitation transfer and delocalization over the pigments, the oxidation of an individual Bchl leads to a complete quenching of the fluorescence (Law and Cogdell, 1998). It is suggested that this photophysical process of electron transfer is responsible for the rapid photobleaching of the complexes in the presence of oxygen (Bopp *et al.*, 1999). In order to reduce photobleaching of the LH2 complexes, oxygen should be removed from the molecule's environment.

A very efficient oxygen scavenging system consists of a mixture of glucose, glucose oxidase and catalase (Harada *et al.*, 1990). This system functions by means of a catalytic reaction, and can therefore continuously remove oxygen from the solution without being consumed, provided sufficient glucose is present. The reaction mechanism of this system is:

$$2\ \text{Glucose} + 2\ O_2 + 2\ H_2O \xrightarrow{\text{Glucose Oxidase}} 2\ \text{Gluconic acid} + 2\ H_2O_2$$

$$2\ H_2O_2 \xrightarrow{\text{Catalase}} 2\ H_2O + O_2$$

The net chemical reaction is:

$$2\ \text{Glucose} + O_2 \xrightarrow[\text{Catalase}]{\text{Glucose Oxidase}} 2\ \text{Gluconic acid}$$

Examples of timetraces recorded under application of this oxygen scavenging system are demonstrated in Fig 4.5. A mixture of 4.5 mg/ml glucose, 216 μg/ml glucose oxidase and 36 μg/ml catalase was used (Harada *et al.*, 1990). The complexes indeed emit over much longer timescales. Because of the reduced chance of photobleaching, the dynamics of the emission over a longer time can be observed. The trace in Fig. 4.5(a) shows little dynamics followed by a single step photobleaching after $\sim$ 103 sec. However, the emission often shows a dynamic behavior with emitting states of intermediate intensities (Fig. 4.5(b)). These intermediate states are typical for strongly interacting multi-chromophoric systems (van den Bout *et al.*, 1997). More examples of LH2 emission behavior and a thorough discussion on the fluorescence lifetimes and the processes governing this behavior is given by Bopp *et al.* (1997).

4.1.6 Spectral fluorescence timetraces

When the foldable mirror M4 in Fig. 2.2 (chapter 2) is flipped out of the detection path, the fluorescence light passes towards the spectrograph and is detected by the CCD camera. The high efficiency of this spectrograph and CCD camera allows spectrally resolved measurements on single molecules. The microscope software enables spectral fluorescence imaging, where a complete fluorescence spectrum is recorded for each image pixel, as well as the measurement of the spectral evolution of a single molecule over time in a so called spectral fluorescence timetrace.
An example of such a spectral timetrace of a single LH2 complex is shown in Fig. 4.6. First, a quick overview image was acquired using the APD to determine the positions of the individual molecules. Subsequently, the foldable mirror was flipped out of the detection path and a spectral timetrace was recorded on each molecule. In the case of Fig. 4.6 it is clearly visible how the molecule switches between states with varying emission intensity. The spectra at three specific points during the trace are shown in Fig. 4.6(b): spectrum 1 during the initial bright state, spectrum 2 during the off period and spectrum 3 during the state with intermediate intensity. Summation of all

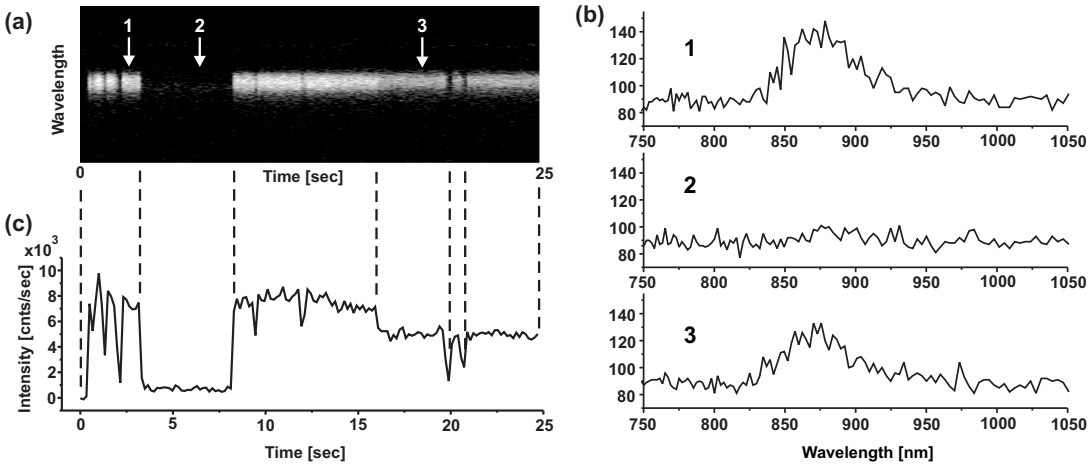

Figure 4.6. A spectral fluorescence timetrace of a single LH2 complex. (a) The complete timetrace represented in 'top-view' with the time on the x-axis, the spectral dimension on the y-axis and the intensity at each wavelength and time represented in the gray-scale. The spectra at three particular moments in time, marked by the arrows, are shown in (b). Summation of all the photon counts in the entire fluorescence band of each spectrum results in a normal intensity timetrace, shown in (c). The trace was measured with 7 μW of 800 nm laser light with an integration time of 150 ms per spectrum.

the photon counts in the entire fluorescence band results in a normal intensity trace, shown in Fig. 4.6(c).

To analyze the emission peak position of the LH2 complexes throughout the states with different intensities, spectral timetraces were acquired of 110 molecules with an excitation intensity of 6.5 μW. The signal to noise ratio of the spectra in each timetrace was improved by performing a singular value decomposition (SVD) analysis on the data set. The reconstructed spectra were fitted with a skewed Gaussian function, using a nonlinear Levenberg-Marquardt fitting procedure. The skewed Gaussian function is described by:

$$F(\lambda) = O + A \cdot exp\{(-ln(2)/b^2)(ln[1 + 2b(\lambda - \lambda_m)/\Delta\lambda])^2\} \tag{4.9}$$

where O is the offset, A the amplitude, λ_m the fluorescence peak wavelength, $\Delta\lambda$ the width and b the skewness (Rutkauskas *et al.*, 2004a). The fluorescence peak wavelength was found to vary from complex to complex with a mean peak position at 868.6 nm and a standard deviation (SD) of 3.0 nm. However, the emission peak for each complex was rather stable during the timetrace, even though the intensity showed discrete steps. The average SD for the peak position during the traces was 1.2 nm. Similar experiments were performed by Rutkauskas *et al.* (2004a; 2004b) on LH2 complexes from the bacterium *Rhodopseudomonas acidophila*. In these experiments, 58 out of 138 (42 %) recorded traces at similar excitation intensity (6 μW) showed discrete long-lived spectral jumps of up to 30 nm, both to the red and to the blue.

The authors conclude that the spectral jumps are light induced. Due to competing non-radiative decay channels within the complex only a fraction of the absorbed photons are re-emitted. The remaining excitation energy is eventually dissipated as heat, which causes a local temperature increase. This local temperature increase is thought to cause structural alterations that are associated with a change in the realization of the static disorder of the electronic transition energies in the system, which is in turn connected to the spectral properties. Differences in the details of the experiments may be responsible for the discrepancy in the observations. First, in our experiments the oxygen level was decreased using the glucose oxidase, catalase, glucose system. Although the oxygen level is strongly reduced, the exact oxygen concentration is unknown. The authors performed their experiments in absence of oxygen. A possible difference in oxygen concentration may play a role in the observed emission properties. Second, the absence of oxygen in the authors experiment allowed them to record the fluorescence emission over 2 minutes per molecule as opposed to 20-30 seconds in our experiments. Considering the duration of their traces may lead to the conclusion that the total observation time in our experiment may have been too short to observe the occurrence of spectral jumps. However, with an occurrence of 42 % one would expect to observe at least a few spectral jumps within the total observation time in our experiments. Third, although the average excitation intensities were comparable in both experiments, our measurements were performed under continuous wave (CW) illumination whereas the authors used pulsed excitation (3 ps pulses). This leads to significantly higher peak intensities which may trigger a 2-photon absorption process. In this case, significant excess energy is pumped into the system which will be dissipated as heat. This could cause the more frequent occurrence of spectral jumps under pulsed excitation. To what extent these factors play a role in the different observations needs to be further investigated.

4.2 Performance of the atomic force microscope

4.2.1 Noise sources in the AFM

High resolution imaging on fragile biological samples requires a low noise level in the height signal. The main noise sources in AFM measurements are:

- Electronic noise
- Laser noise
- Thermal noise (Brownian motion of the cantilever)
- External noise sources (mechanical or acoustical vibrations, air flow, etc.)

The relative contributions of each of the noise sources in the AFM system will be discussed below. The noise levels will be shown for two different cantilevers from the same chip (Veeco Microlevers, MSCT-AUHW): a typical contact mode and a typical

tapping mode cantilever, tip C and F respectively. The characteristics of these two cantilevers and the other cantilevers on this type of chip are summarized in appendix A.

Electronic noise

The electronic noise level can be determined by acquiring the deflection signal when the AFM laser is switched off, therefore only measuring the electronic contribution. The power spectral density of this deflection signal is shown in Fig. 4.7. The measurement was performed over a frequency range spanning six orders of magnitude in three sections (0.06-6 Hz; 6-1000 Hz; 1-100 kHz). Recording the high frequency part takes considerably less time than the low frequency sections and could therefore be averaged longer, which results in the less noisy appearance of this part of the spectrum.
The electronic noise is measured as a voltage, but the noise levels in a deflection signal attain a meaningful value when they are expressed in nanometers, using the deflection calibration constants of the particular cantilevers. These deflection constants were determined to be 410 nm/V for tip C and 125 nm/V for tip F, when the laser intensity is adjusted such that the sum of the voltages (V_{sum}), produced by the four segments of the quadrant detector, equals 8 V. Because each cantilever has a different deflection constant, the meaning of the electronic noise level expressed in nanometers depends on the cantilever used.
The electronic noise spectrum shows a plateau between $\sim 20\ \text{Hz} - 20\ \text{kHz}$, at roughly $1.8 \times 10^{-5}\ \text{nm}_{\text{rms}}/\sqrt{\text{Hz}}$ for tip F and $5 \times 10^{-5}\ \text{nm}_{\text{rms}}/\sqrt{\text{Hz}}$ for tip C. In the low frequency part, the 50 Hz power supply frequency and its 3rd (150 Hz) and 5th (250 Hz) harmonic dominate. These contributions can perhaps be reduced by more careful shielding and grounding of the electronic wires. Below 20 Hz the noise level shows the typical '1/f' behavior, containing various types of low frequency contributions. The level increase above 20 kHz can be attributed to a phenomenon called 'gain peaking' which is observed in photodiode current-to-voltage conversion using operational amplifiers.

Laser noise

A well designed AFM detection system is limited only by laser shot noise. This determines the smallest change in signal detectable on the segments of the quadrant photodiode. The signal to noise ratio can be optimized by using adequate laser power. To determine the contribution of laser noise the AFM laser was switched on, and the beam was reflected off the gold coated back-side of the chip that holds the cantilevers (see appendix A). This chip acts as a solid mirror for which thermal motion can be neglected. The laser intensity was adjusted to a sum voltage (V_{sum}) of 8 V, produced by the four segments of the quadrant photodiode. The noise level increases over the entire frequency range (Fig. 4.7). The detection system is clearly limited by laser noise. In the high frequency range (> 1 kHz) this is mainly shot noise, whereas in the low frequencies pointing stability and slow intensity fluctuations are likely to contribute.

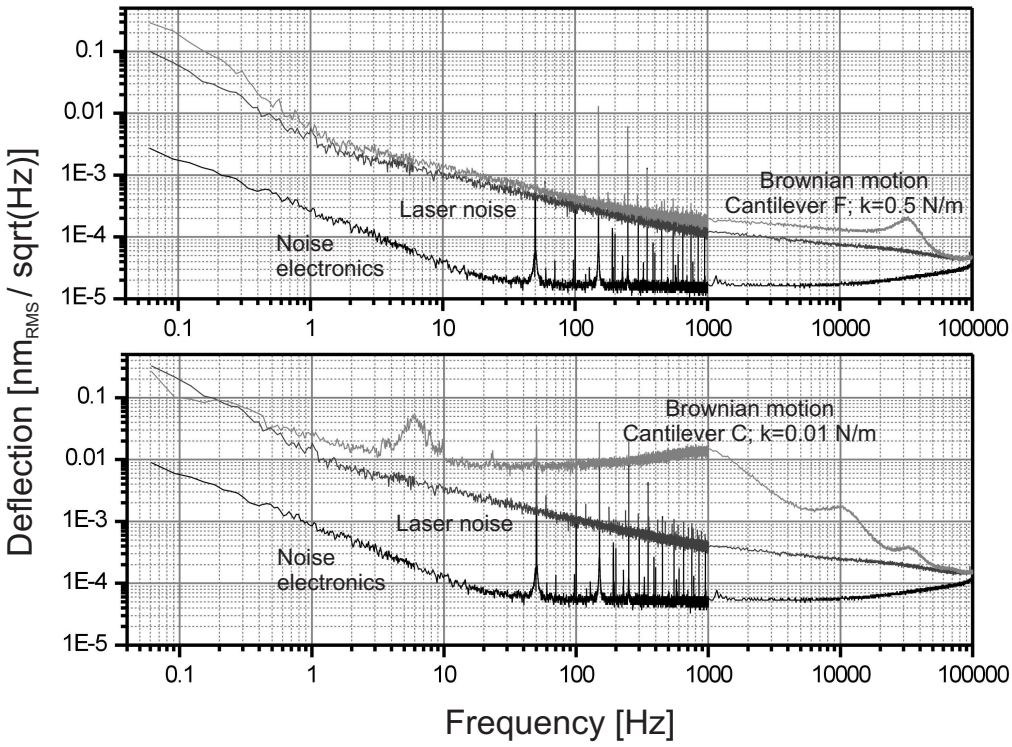

Figure 4.7. Noise levels of the AFM system for frequencies ranging from 0.06 Hz-100 kHz. The electronic noise level and the noise level with the AFM laser switched on are translated from $V_{rms}/\sqrt{Hz}$ into $nm_{rms}/\sqrt{Hz}$ by multiplication with the specific deflection constants of the two cantilevers. The detection system is clearly limited by laser noise. However, close to their resonance frequencies, the lowest detectable cantilever displacement is limited by the thermal motion of the cantilevers themselves. The resonance peak of the thermal motion for cantilever F can be clearly observed at ~ 33 kHz. For cantilever C the main resonance frequency in liquid lies at 1 kHz, but also two higher order resonances at ~ 10 and ~ 32 kHz are visible.

Thermal noise

An AFM cantilever in thermal equilibrium with the environment undergoes thermal (Brownian) motion. If the cantilever motion is modelled as a harmonic oscillator, the equipartition theorem states that

$$\frac{1}{2}k\langle(x-x_0)^2\rangle = \frac{1}{2}k_BT \tag{4.10}$$

where x_0 is the x-coordinate of the mean (equilibrium) position, k_B is Boltzmann's constant and T is the temperature in Kelvin. With k_BT on the order of 4×10^{-21} J

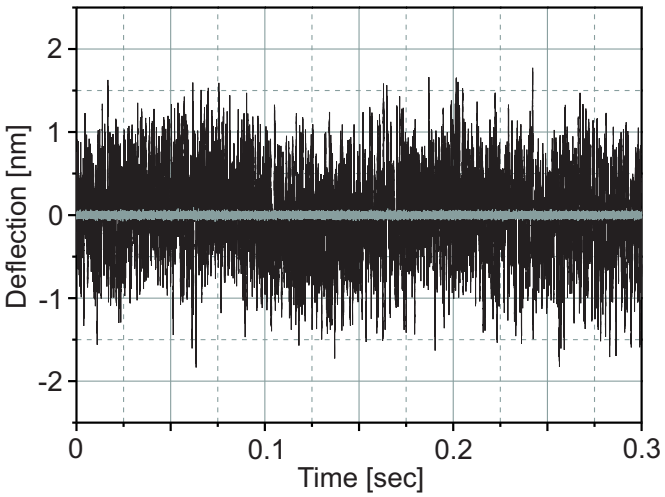

Figure 4.8. Timetraces of the Brownian motion of cantilever C (black trace) and cantilever F (gray trace) during 0.3 sec. The peak-peak thermal motion of cantilever C and F amount ~ 3 and ~ 0.17 nm respectively.

at room temperature the r.m.s. thermal motion of a cantilever with a spring constant k of 0.5 N/m amounts 0.09 nm. Near its resonance frequency it is this fundamental thermal motion of the cantilever itself that sets the lower limit to the deflection that can be measured with a well designed AFM (Gittes and Schmidt, 1998; Bonnell, 2001).

In order to observe the Brownian motion, the laser was subsequently focussed on cantilever C and F, immersed in liquid, and V_{sum} was again adjusted to 8V. For tip F, the noise level only increases significantly for higher frequencies, as expected for a relatively stiff cantilever (Fig. 4.7). At its resonance frequency in liquid (~ 34 kHz) a clear peak in thermal motion is observed. The much weaker cantilever C shows strong thermal motion down to low frequencies. The main resonance frequency in liquid is clearly visible at 1 kHz as well as two higher order resonances at ~ 10 and ~ 32 kHz (Stark *et al.*, 2001).

To assess the amplitude of the thermal motion of both cantilevers, a time domain measurement was performed. The thermal motion of tip C dominates the deflection signal from ~ 1 Hz to 50 kHz. Therefore the timetrace of tip C was measured from DC to 50 kHz using a second order low pass filter. The Brownian motion of tip F mainly dominates from $\sim 10 - 60$ kHz, therefore the timetrace of tip F was recorded passing only this frequency range using a bandpass filter. The traces are shown in Fig. 4.8 over a time window of 0.3 sec which corresponds roughly with a single line scan in a typical AFM image. The trace were recorded with a sampling rate of 200 kHz. Cantilever C (black trace) shows a peak-peak thermal motion of ~ 3 nm. The thermal motion of the significantly stiffer cantilever F (gray trace) is much smaller, with a peak-peak amplitude of ~ 0.17 nm.

Clearly, the sensitivity of the beam deflection is sufficient to detect the thermal motion of these cantilevers in liquid. Close to their resonance frequencies, the sensitivity of the AFM system is limited by Brownian motion of the cantilevers, rather than by electronic or laser shot noise.

	Noise from real cantilever deflections	**Noise from artificial deflection signals**
Noise within the bandwidth of the feedback	e.g. low frequency thermal motion, mechanical vibrations, drift in AFM construction, bending of the cantilever (tapping mode only) **consequence: height noise [nm]**	e.g. air flow, interference effects, optical feedback effects **consequence: height noise [nm] àand force noise [pN]**
Noise beyond the bandwidth of the feedback	e.g. high frequency thermal motion **consequence: force noise [pN]**	e.g. high frequency laser current modulation **consequence: none**

Table 4.1. Consequences of different noise sources during AFM imaging.

External noise sources

In addition to the noise sources mentioned above, which are all inherent to the AFM system, there are external influences that can contribute noise to the measurements. Temperature changes cause cantilevers to bend, which results in a changing imaging force. Local temperature changes can cause the thermal expansion or contraction of AFM structure which can lead to erroneous height measurements. Air flow through the laser beam causes slight local changes in air density and thereby variations in the index of refraction. This results in a fluctuating light path causing artificial deflection signals. Furthermore, mechanical and acoustical vibrations can disturb an AFM measurement. Most of these noise sources occur at low frequencies below 1 kHz. Noise caused by temperature effects can be minimized by allowing the AFM system to equilibrate with the environment before starting measurements. Acoustic vibrations and air flow can be reduced by covering the AFM with a closed box. The AFFM is particularly sensitive to acoustical vibrations since combined experiments have to be performed on thin substrates which form a membrane that can easily pick up acoustical signals. Mechanical vibrations are usually suppressed by placing the AFM head on a vibration damping table. In case of the combined system, the complete AFFM instrument is placed on inflated inner tubes.

Impact of different noise sources

AFM imaging is mostly performed using a feedback loop in order to maintain a certain interaction force with the sample. The voltage applied to the piezo tube to keep this constant interaction force provides the height signal. This feedback loop has a certain bandwidth and therefore the influence of noise sources on AFM measurements depends on the type and the frequency of the noise. Noise sources can lead to height noise in the images, noise in the imaging force or both height and force noise. The various possibilities are summarized in table 4.1, where noise sources are separated in noise originating from real cantilever deflections and artificial deflection signals. One important source of a varying imaging force could not be placed in this table: thermal equilibration of the cantilever which causes bending when suspended free in

solution, will result in a changing interaction force in contact mode imaging, because the deflection is kept constant by the feedback loop.

4.2.2 Detection limits of the AFM

AFM imaging is mainly performed in either contact mode or tapping mode. The contact mode is a DC coupled mode, where the tip is continuously in contact with the surface. The height profile is detected by the deflection of the cantilever. The tapping mode is an AC coupled mode in which the cantilever is oscillated near its resonance frequency, and the tip touches the surface for only a brief period during an oscillation. The height profile in tapping mode is detected from the change in oscillation amplitude. Consequently, these two imaging modes operate in different parts of the frequency spectrum.

For high resolution imaging on fragile biological samples, an accurate height measurement using very low interaction force is required. In contact mode, cantilevers with a low spring constant are used in order to minimize the interaction forces associated with a deflection. The relatively large amplitude of the thermal motion of weak cantilevers (Fig. 4.8) is damped by the surface and therefore the uncertainty in the tip position is reduced. Because of its low spring constant, tip C is a suitable contact mode tip. In tapping mode, the tip touches the surface only briefly during each oscillation period. Consequently, for a low spring constant cantilever, the thermal motion causes a significant uncertainty in tip position compared to the size of the objects to be imaged. The tip position is much better defined for cantilevers with a higher spring constant such as tip F (Fig. 4.8). The small amplitude of the Brownian motion for these cantilevers allows the use of tapping amplitudes as low as 1-5 nm. The amount of damping of the oscillation amplitude by the sample determines the interaction force. As an additional advantage, the higher resonance frequency of stiffer cantilevers allows higher scan speeds, reducing the imaging time.

The detection limits of the AFM are determined in both contact mode, using tip C, and tapping mode, using tip F. This was done by placing the tip in contact with the surface with the feedback switched on and measuring the noise on the height signal. To exclude contributions from surface roughness in this noise measurement, no scanning motion was applied. In contact mode and tapping mode different input signals are used for the feedback loop. Contact mode uses the deflection signal directly whereas in tapping mode, the r.m.s. deflection value is used. Therefore, first the noise contributions to these input signals are determined before placing the tips in contact with the surface. The measurements were performed on a thin coverglass (#1, thickness 170 μm, $\varnothing$ 24 mm, Menzel-Gläser, Braunschweig, Germany). The objective of the confocal microscope was placed such that it was focussed on the top layer of the glass with the immersion oil in between the glass and the objective, corresponding to the situation in combined experiments. In this way all relevant noise sources are taken into account: electronic noise, laser noise, thermal noise, mechanical and acoustic noise.

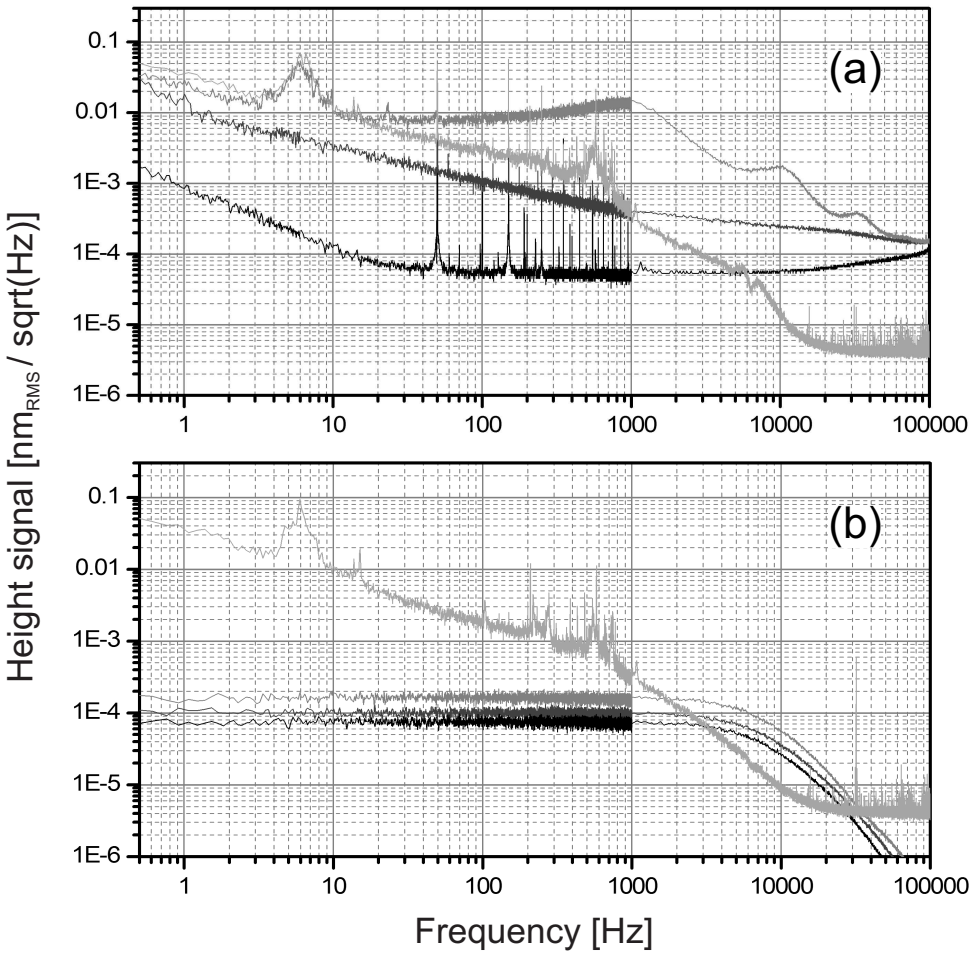

Figure 4.9. Spectral distribution of the noise levels in contact mode (a) and tapping mode (b). The electronic noise (black), laser noise (dark gray) and the thermal noise (gray) are the noise levels on the deflection signal in (a) and the r.m.s. amplitude of the deflection signal in (b). The light gray curves represent the noise on the height signal measured in contact with the surface of a coverglass with the feedback switched on in contact mode (a) and in tapping mode (b).

Contact mode

In contact mode, the deflection signal is directly used as the input signal for the feedback loop. The noise contributions on this deflection signal, illustrated in Fig. 4.7, are shown once more in Fig. 4.9(a): electronic noise (black), laser noise (dark gray) and thermal noise measured free in solution (gray). The noise on the deflection signal is limited by laser noise, and by thermal noise when the cantilever is free in solution. To determine the detection limit in contact mode, tip C was brought in contact with the glass coverslip with an interaction force of ~ 100 pN, and the feedback was switched on. The spectral distribution of the noise on the height signal is shown as the light gray curve in Fig. 4.9(a). The thermal motion is clearly damped when the tip is in

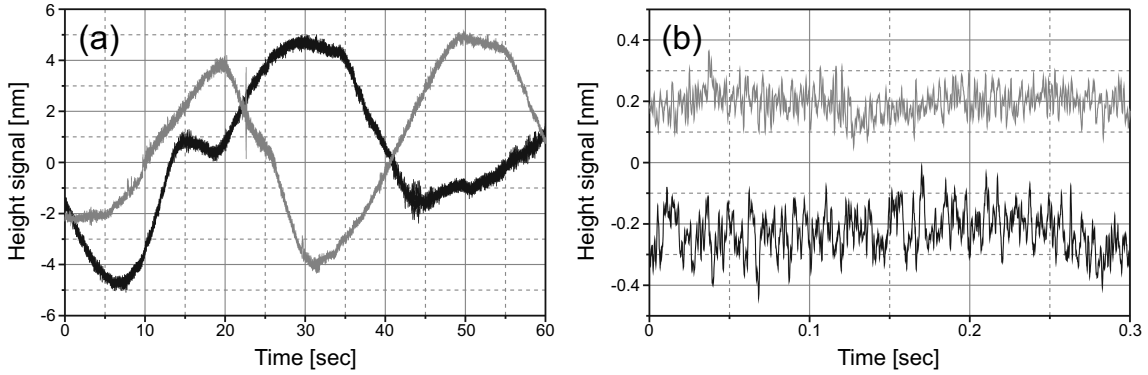

Figure 4.10. Time traces of the height signal measured in contact with the coverglass in contact mode (black curve) and in tapping mode (gray curve). (a) Timetrace measured over 60 sec showing the low frequency height variation due to thermal expansion and contraction of the AFM construction. (b) Timetrace over 0.3 sec, the peak-peak noise on this timescale in contact mode amounts ~ 0.4 nm and in contact mode ~ 0.2 nm.

contact.
The height signal shows a number of distinct peaks due to mechanical vibrations. At 6 Hz there is a very prominent peak which corresponds to the eigenfrequency of the complete AFFM on the inner tubes. This peak also appears when the tip is free in solution. Furthermore, vibration peaks occur between $\sim$ 200 and 800 Hz with a pronounced peak close to 600 Hz.
In addition to the peaks due to mechanical vibrations, the 50 Hz peak from the electronics and its 3rd (150 Hz) and 5th (250 Hz) harmonic are prominently present. The corresponding time domain measurements of the height signal are shown in Fig. 4.10 (black curves). The timetraces were recorded in two time intervals: 60 sec, which corresponds roughly with the time needed to record a single AFM image and 0.3 sec, which is in the order of a single line scan. The 60 sec timetrace shows the low frequency thermal expansion and contraction of the AFM construction over $\sim$ 10 nm. The small temperature changes causing this motion are mostly originating from air flow along the construction. The amplitude of this slow thermal motion is significantly decreased when the AFM head is covered with a closed box reducing this air flow (data not shown). These low frequency components are usually filtered from the height signal and therefore do not appear in the image. Between 42 and 47 seconds, a disturbance due to mechanical vibrations at 6 Hz appears. The peak-peak noise on the short time scale determines the detection limit. For the contact mode trace in Fig. 4.10(b) a peak-peak noise of ~ 0.4 nm is found.

Tapping mode

In tapping mode, the deflection signal is first filtered by a bandpass filter around the tapping frequency (bandwidth $\sim$50 kHz, from 10-60 kHz) and subsequently the r.m.s. amplitude is determined by a true r.m.s. decoder with a bandwidth of 5 kHz. This means that, for a tapping frequency of 35 kHz, only 7 tip-sample contacts are used

to measure the tapping amplitude. This resulting r.m.s. deflection value is the input signal for the feedback loop. The electronic noise (black), the laser noise (dark gray) and the thermal noise (gray) contributions to this signal are plotted in Fig. 4.9(b). The thermal noise was determined with cantilever F free in solution. The detection of the r.m.s value of the tapping amplitude is limited by the thermal motion of the cantilever. A striking difference between these noise levels and the noise levels in the deflection signal (Fig. 4.9(a)) is the complete absence of the low frequency '1/f' part of the noise. Also the 50, 150 and 250 Hz peaks generated by the electronic power supply are not present in the r.m.s. tapping signal. In the AC coupled tapping mode signal, these low frequency disturbances are rejected by the bandpass filter.
Subsequently the tip was brought into contact and the feedback was switched on. The tip was oscillated with an amplitude of $\sim$ 5 nm and the damping was set to the minimum value that resulted in a stable feedback. The spectral distribution of the height signal (light gray curve Fig. 4.9(b)) is very similar to the one measured in contact mode. Again the strong peak at 6 Hz is present as well as the peaks between 200 and 800 Hz. However, the supply frequencies at 50, 150 and 250 Hz are absent. At 32 kHz the peak of the tapping frequency appears.
The corresponding time domain measurements of the height signal are shown in Fig. 4.10 (gray curves), again recorded during time intervals of 60 sec and 0.3 sec. The 60 sec timetrace shows the same low frequency thermal expansion and contraction of the AFM construction, as expected, which could be reduced by covering the AFM head. The timetrace over 0.3 sec shows a peak-peak noise in the height signal of $\sim$ 0.2 nm.

Discussion

From the noise measurements in contact it is clear that the suspension of the AFFM can be improved. The 6 Hz peak is very prominent and is also detected by tip C free in solution. During the measurements, this frequency was very easily excited even by the smallest disturbance. The vibrational peaks between 200 and 800 Hz may also be reduces by improving the suspension.
The height measurement was also found to be very sensitive to acoustic noise sources, as may be expected from the geometry of the measurement situation. The substrate holder has been designed such that the freely suspended surface area of the cover-glass is as small as possible to minimize acoustic coupling. To prevent large acoustic disturbances, the AFFM should be placed in a very quiet environment.
The 50 Hz peak from the electronics and its higher harmonics form a relatively large contribution to the height signal in contact mode measurements. These contributions can most likely be reduced by improvement of the electronic connections.
In general, it can be concluded that the noise in the height signal is dominated by vibrations. Therefore, to improve the signal to noise ratio in the height signal, the vibration damping in the instrument should be optimized. In contact mode the vibration contribution can be improved by roughly a factor of 3 before the laser noise becomes dominant and no further improvement can be achieved. However, the tapping

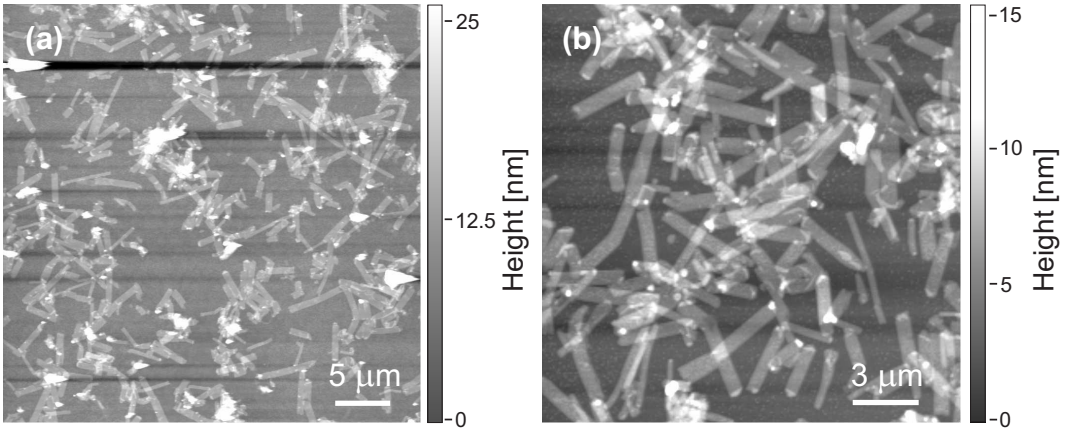

Figure 4.11. Large range AFM images of 2D LH2 crystals using the sample stage. (a) 38×38 μm^2; (b) 19×19 μm^2. The images show no distortions due to the internal position feedback of the stage.

mode leaves potentially much more room for improvement, because the low frequency '1/f' contributions from the deflection signal are not playing any role in this mode. Nevertheless, the determined detection limits for the AFFM of 0.4 nm for contact mode and 0.2 nm for tapping mode is a very good result for the combined instrument.

4.2.3 From large range to high resolution

The atomic force microscope in the AFFM is in principle a stand alone AFM, meaning that the AFM head is equipped with its own three dimensional piezo-tube scanner to perform imaging. However, in the combined microscope the lateral scanning motion can also be performed by the sample scanning stage, while the tip is kept fixed in lateral directions. The sample scanner has two main advantages over the tip scanner. First, the scan range of this stage is 40×40 μm^2 compared to the 3×3 μm^2 lateral range of the piezo tube. Therefore a much larger surface area can be covered by using the sample stage. Second, the sample scanner is equipped with an accurate internal position feedback system. This prevents the non-linear motion characteristics typical for piezo actuators without position feedback.
In Fig. 4.11(a) and (b), large range AFM images are shown of 2 dimensional crystals of LH2 complexes. The sample was prepared on a mica substrate and imaged in air, using a silicon nitride tip (k=0.5 N/m). The scan range in Fig. 4.11(a) is 38×38 μm^2 and in (b) 19×19 μm^2.
The motion of the sample stage is controlled by a 16 bit data acquisition card (6052 E, National Instruments). Therefore, the full range of 40 μm can be sampled with a minimum step size of 0.6 nm ($40000/2^{16}$). High resolution small range images can be acquired anywhere within the total scan range by zooming-in using just the software. By reducing the initial scan range using the AFM hardware, the minimum step size can be reduced further.
Fig. 4.12 shows examples of high resolution images, acquired using the sample scanner.

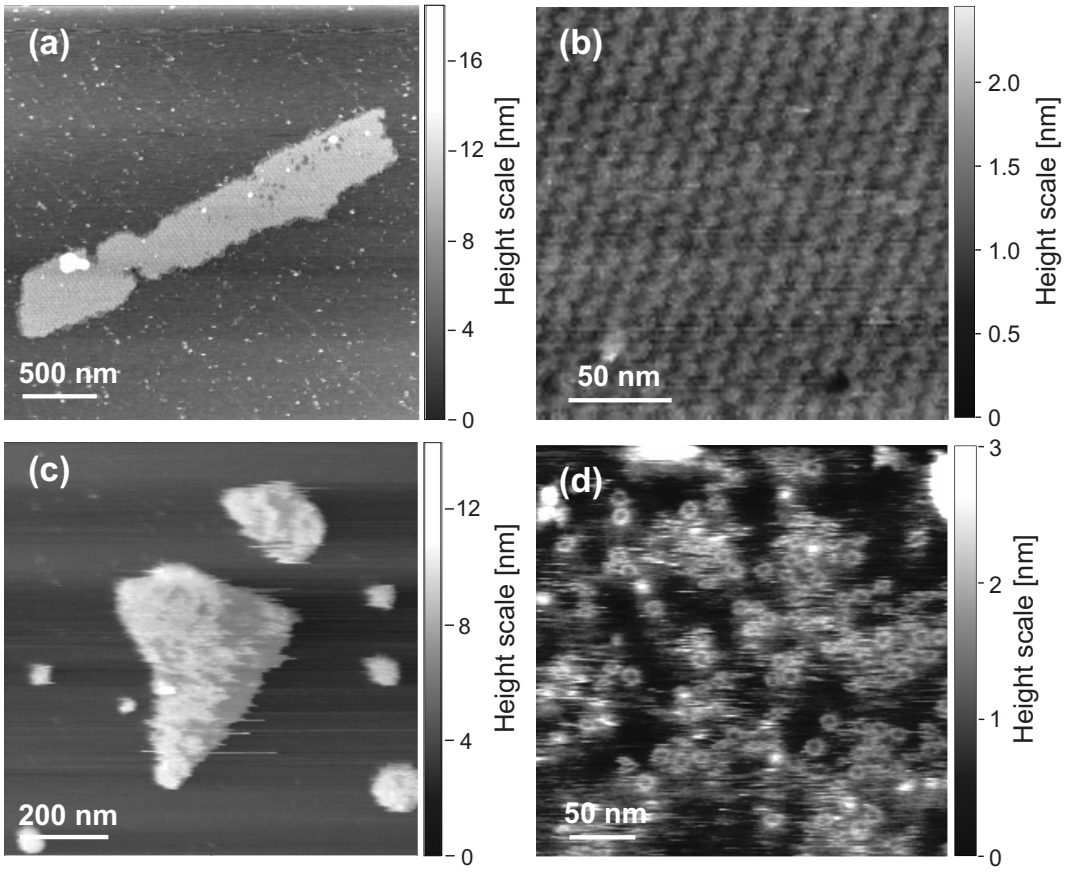

Figure 4.12. High resolution images of 2 dimensional crystals of LH1 and LH2 complexes. (a) Overview of an LH2 crystal; some periodic structure can already be observed. (b) Zoom-in on the LH2 crystal, showing the 'zig-zag' packing arrangement. (c) Overview of an LH1 crystal. (d) High resolution image of the individual LH1 complexes in the crystal. All images were measured on mica in buffer solution.

Fig. 4.12(a) shows an overview of a 2D LH2 crystal. Already some order in the structure of the crystal is observable at this scan range. A zoom-in on the crystal (b) shows the 'zig-zag' packing of the individual LH2 complexes. Similarly, a 2D LH1 crystal image is shown in (c). In the zoomed-in image of Fig. 4.12(d) the ring shape of the individual pigment-protein complexes can be resolved. All images were recorded on a mica substrate in buffer solution.

The combination of the AFM with the confocal fluorescence microscope does not compromise the ability to measure topographic images with a high spatial resolution. The mechanical vibrations observable in Fig. 4.9 do not appear in the image. The use of a long range scanner with internal position feedback in combination with 16 bit control enables large range overview scanning down to high resolution small range imaging.

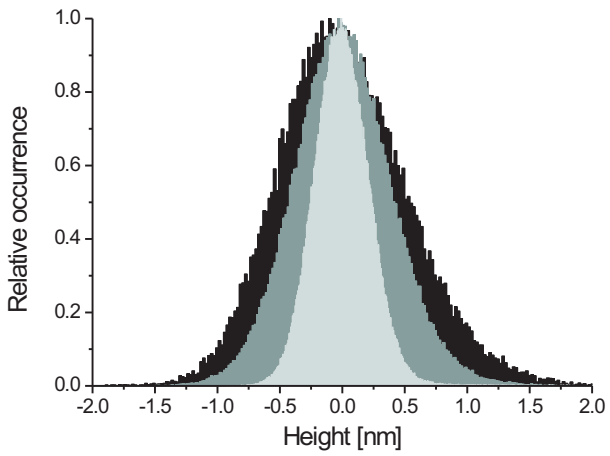

Figure 4.13. Comparison of the surface roughness of glass and mica. The roughness was estimated from topography images measured on a surface of 624×624 nm^2 for mica, glass and glass coated with 0.01% poly-L-lysine. The height distribution for of all pixels of each image was plotted in a height histogram. The light grey histogram corresponds to the mica surface, the dark grey to the glass surface and the black corresponds to the glass coated with PLL.

4.2.4 AFM on individual pigment-proteins on mica and glass substrates

The most commonly used substrate for AFM measurements is mica. Mica is layered material, which can be easily cleaved using tape to produce clean and atomically flat surfaces, ideal for AFM measurements. The mica surface is negatively charged at all pH values. Since most proteins contain both positive and negative amino-acid residues, this surface charge is used for immobilization of samples to the surface based on electrostatic interaction.

For combined AFM and optical measurements however, mica is not well suited since this material is birefringent and has a comparatively low optical transmittance. It is therefore most convenient to use standard glass coverslips as a substrate in combined experiments. However the surface of these glasses is not as smooth as a mica surface. A comparison between the surface roughness of a mica slide and standard coverslips is shown in Fig. 4.13. For this measurement, an area of freshly cleaved mica (muscovite mica, Ted Pella Inc., Redding, California, USA) of 624×624 nm^2 and a similar area on a coverslip (#1, ⌀ 24 mm, Menzel-Gläser, Braunschweig, Germany) was measured at 512×512 pixels. The coverslip was extensively cleaned by sonication in a solution of 65% HNO_3. In addition, the surface of a coverglass coated with poly-L-lysine (PLL, 0.01%) was measured at 256×256 pixels, also over an area of 624×624 nm^2. The height distributions of all the pixels for each substrate were plotted in a height histogram. The FWHM (full width at half of the maximum) of this distribution is 0.48 nm for mica, 0.84 nm for glass and 1.12 nm for glass with PLL. Although the glass surface, and in particular the one coated with PLL, is indeed more rough than mica, the smoothness should still be sufficient for the localization of individual proteins.

To test this conclusion, individual LH2 complexes were immobilized on a mica and a PLL-coated glass surface, and subsequently imaged in TRIS buffer at pH7.5, using

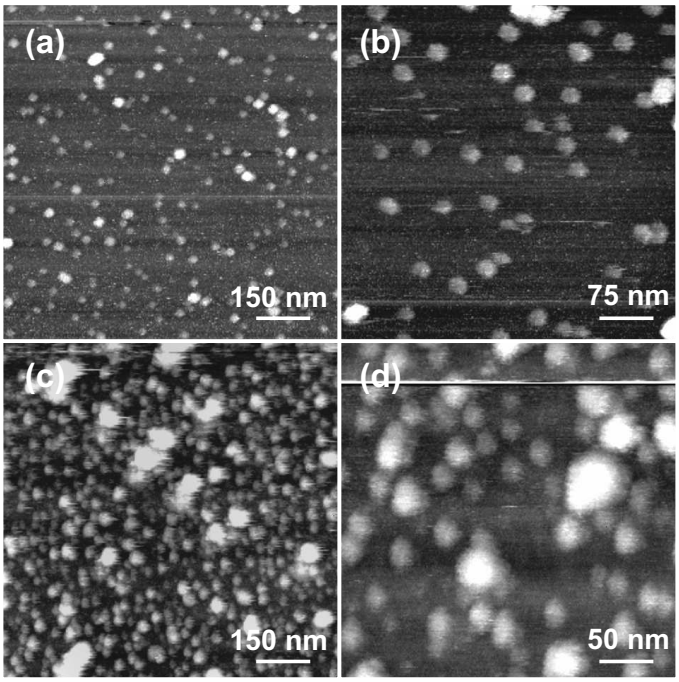

Figure 4.14. AFM images of individual LH2 complexes. Images (a) and (b) were taken on a mica substrate while (c) and (d) were measured on glass substrate coated with poly-L-lysine.

a Si_3N_4 tip (Tip F, k=0.5 N/m, Veeco Microlevers, MSCT-AUHW). The images are shown in Fig. 4.14. The individual proteins are clearly visible on both mica and glass. In both cases the individual objects appear ~ 4 nm high and $20 - 30$ nm in diameter due to tip convolution. This largely corresponds to the dimensions of the complexes. Although the proteins can be visualized on both types of substrate, sharp and reproducible images proved to be easier obtainable on mica than on glass.

4.3 Conclusions

The requirements which were defined for the AFFM are fulfilled in the constructed instrument.The confocal fluorescence microscope has the sensitivity to detect single molecule fluorescence up to the near IR part of the spectrum using the APD's as well as the spectrograph. In spectral time traces, single molecule spectra can be acquired with a time resolution of 150 ms.
The 1050 nm light from the AFM-laser, collected by the microscope objective, can be sufficiently suppressed in the detection path using the AFM suppression filter. On the timescales of single molecule measurements, this light causes no significant background. Furthermore, the 1050 nm wavelength in combination with the interference filter prevents excitation of the light harvesting complexes by the AFM laser.
The detection system in the AFM is limited by laser noise and is sensitive enough to detect the Brownian motion of the cantilevers. The noise in the height signal is dominated by vibrations. The signal-to-noise ratio can be improved by changing the suspension of the AFFM. Nevertheless, the detection limits were determined to be ~ 0.4 nm in contact mode and ~ 0.2 nm for tapping mode.

The large range sample stage allows AFM imaging over large areas. The 16 bit resolution of the data acquisition card enables zooming in and performing high resolution imaging just by software zooming. Individual LH complexes could be observed on a mica surface as well as on a glass surface.

Chapter 5

Combined experiments

In this chapter, the operation of the AFFM is demonstrated on biological samples in an aqueous environment. The experiments are performed in several modes of operation. The power of simultaneous imaging and combined AFM / spectral fluorescence imaging is demonstrated respectively on LH2 crystals and membrane fragments containing both LH1 and LH2 complexes. The ultimate goal for the AFFM is to perform simultaneous AFM and fluorescence measurements on individual proteins, and additionally to use the AFM tip as a manipulation tool while simultaneously recording fluorescence emission. The steps taken to achieve this goal are treated in this chapter along with combined experiments on single LH2 complexes.

5.1 Photoluminescence of the tip material

During simultaneous imaging of a sample, a direct spatial correlation between topographic and optical features is obtained when the AFM tip is aligned within the excitation focus of the confocal microscope. However, it was found that proper alignment inevitably leads to luminescence caused by the tip material itself, in addition to the direct scattering of the excitation light from the tip. This was also recently reported by Toda *et al.* (2004). The intensity of the luminescence depends on the specific material. The most commonly used tip materials are silicon (Si) and silicon nitride (Si_3N_4). The emission spectra of a Si_3N_4 tip (Veeco Microlevers, MSCT-AUHW) and a Si tip (Mikromasch, NSC36/Cr-AuBS) excited with 488 nm and 800 nm laser light, measured by the spectrograph, are presented in Fig. 5.1. The spectrum emitted at 800 nm excitation was accumulated over a 1 minute time interval and that with 488 nm excitation over a 3 sec time interval. In both cases ~ 7 μW of laser light was focussed on the tip.
The luminescence from the Si_3N_4 tip covers a broad spectral region and may spectrally overlap with the emission of the chromophores in the sample, in which case it cannot be removed by spectral filtering. The intensity of this luminescence is comparable with the fluorescence intensity of a few LH1 or LH2 molecules in the case of 800 nm excitation, and is far more intense when excited with 488 nm excitation. The Si tip

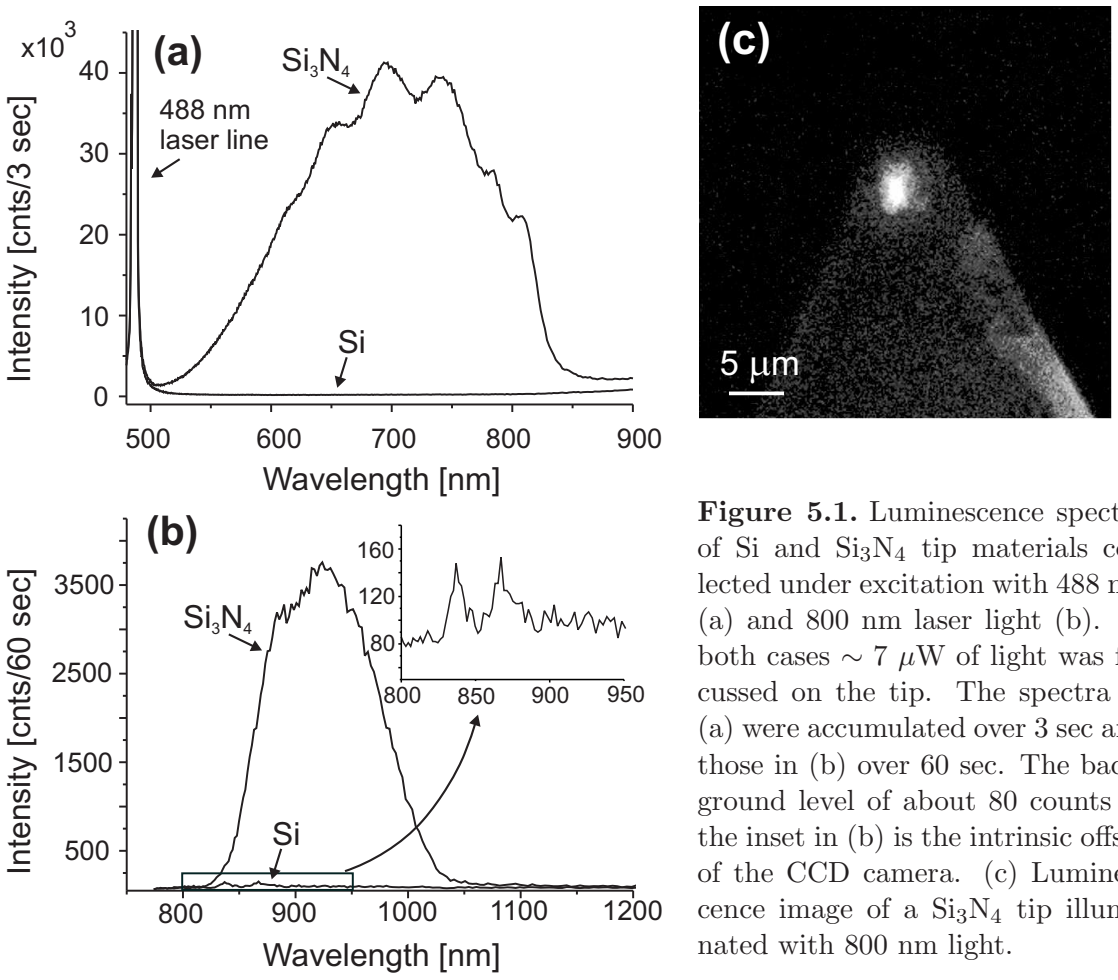

Figure 5.1. Luminescence spectra of Si and Si_3N_4 tip materials collected under excitation with 488 nm (a) and 800 nm laser light (b). In both cases ~ 7 μW of light was focussed on the tip. The spectra in (a) were accumulated over 3 sec and those in (b) over 60 sec. The background level of about 80 counts in the inset in (b) is the intrinsic offset of the CCD camera. (c) Luminescence image of a Si_3N_4 tip illuminated with 800 nm light.

however, shows a different type of emission with much lower intensity (Fig. 5.1), which is negligible compared to typical single molecule emission intensities, even at 488 nm excitation.

The low luminescence of the silicon tips is caused by the fact that crystalline silicon has an indirect band gap. Electrons in indirect band gap semiconductors need to change both momentum and energy to switch between the valence and the conduction band levels. Luminescence from silicon is therefore highly unlikely. However, amorphous silicon and amorphous silicon nitride are known to be strongly photoluminescent (Wolford *et al.*, 1983; Poolton and Cros, 1991; Aydinli *et al.*, 1996). Silicon nitride tips are generally manufactured from amorphous material, produced by low pressure chemical vapor deposition (LPCVD) (personal communication with Veeco Microlevers), and thus display considerable luminescence. The luminescence spectrum measured from the silicon nitride tip (Fig. 5.1) corresponds nice with the spectrum of bulk amorphous silicon nitride found in the literature (Serpengüzel, 2001). Silicon tips on the other hand are produced from crystalline silicon, hence the low amount of luminescence produced by these tips. This leads to the conclusion that it is imperative to use tips made from crystalline silicon or other low-luminescent materials for the purpose of

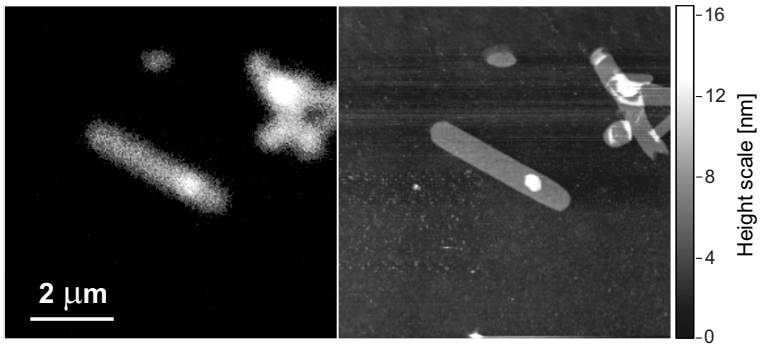

Figure 5.2. Combined simultaneous imaging on 2 dimensional LH2 crystals. The AFM tip was aligned with the optical axis of the fluorescence microscope. While scanning the sample, the height profile and optical information was detected simultaneously. One of the APD's was used for the optical detection.

simultaneous AFM/optical measurements.

5.2 Combined imaging on crystals and membranes

Simultaneous imaging

In simultaneous fluorescence and topographic imaging mode, the sample is scanned between the microscope objective and the AFM-tip. The vertical motion of the tip relative to the sample is induced by the piezo-tube inside the AFM in order to maintain a constant imaging force. Fluorescence and topographical information are collected simultaneously and are inherently spatially correlated, due to the coincidence of the excitation focus and the AFM tip.

Fig. 5.2 shows simultaneously recorded fluorescence and topographic AFFM images of two-dimensional crystals of light harvesting complexes LH2. The crystals were adsorbed on a poly-L-lysine (0.01%) coated coverglass. The glasses were extensively cleaned in a solution of 65% HNO_3 before adding the coating. The measurement was performed in a solution of 50mM TRIS pH7.8, 150 mM KCl in tapping mode using a Si tip (Mikromasch, NSC36/Cr-AuBS, k=0.6 N/m). The optical signal was recorded using one of the APD's. The sample was imaged with 256×256 pixels and a pixel frequency of 2000 Hz and hence a recording time of the optical signal of 0.5 ms per pixel.

In the AFM image, the LH2 crystals are observed as sheets with a length of several microns and a width up to ~ 1 μm. The crystals are ~ 6 nm high. A clear correlation exists between the topographic and the optical image. Comparison of both images demonstrates the superior lateral resolution of the AFM. The optical image provides information about the composition of the structures. The higher topographic features on the crystals correspond with an increased intensity of the fluorescence emission, indicating that a second layer of crystal is lying on top rather than some impurity.

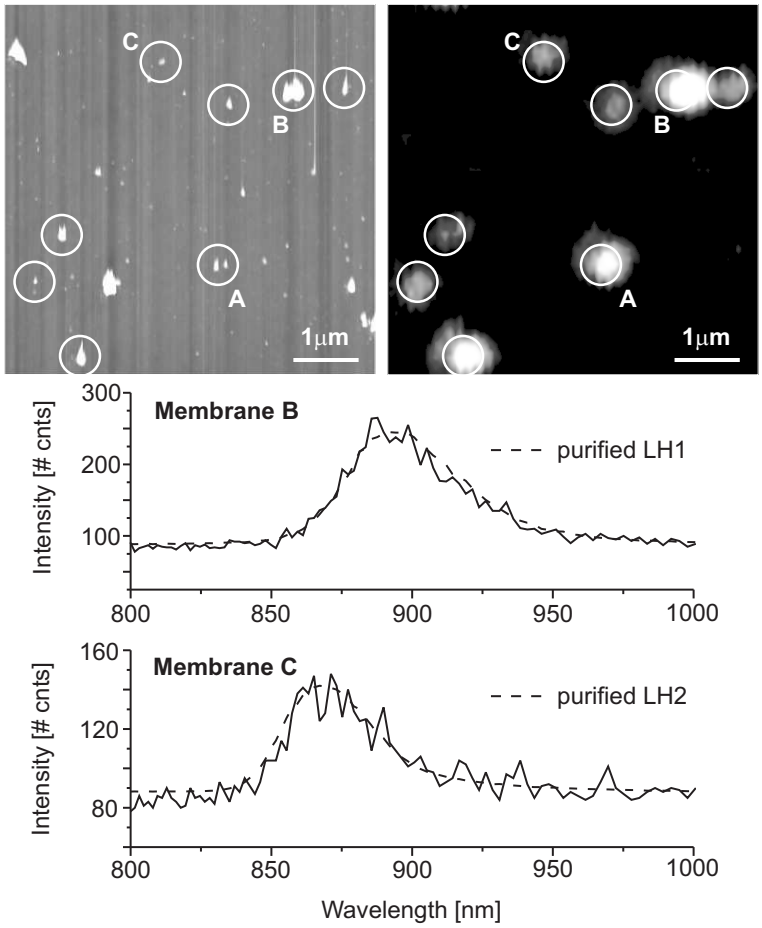

Figure 5.3. Combined AFM and fluorescence spectral imaging on membranes fragments from *R. Sphaeroides*, containing both LH1 and LH2 complexes. The content of the membrane fragments can be estimated from the spectral information. See the text for a discussion of this figure.

Combined AFM and spectral fluorescence imaging

The ability to perform spectral fluorescence imaging strongly enhances the chemical identification capacity of the instrument. In conventional spectral fluorescence imaging, a complete fluorescence spectrum is measured for each image pixel. Multiple fluorescent components can be easily distinguished even when their emission spectra partially overlap. In order to obtain a spectrum with a sufficient signal to noise ratio, the acquisition time per pixel is usually in the order of 10 ms or more. However, in AFM imaging the time per pixel is usually much lower, typically ranging from 0.2 to 0.5 ms. Because of this discrepancy, the AFM and spectral fluorescence images are recorded sequentially.

The potential of combined AFM and spectral imaging is demonstrated in Fig. 5.3. In this measurement, small membrane fragments of the photosynthetic bacterium *R. sphaeroides* were immobilized on a coverglass coated with poly-L-lysine. The membranes contain both types of light harvesting complexes, LH1 and LH2. The sample was measured in a buffer solution containing 10 mM HEPES pH7.5, 150 mM KCl. The spectral image was recorded on an area of 5.5×5.5 μm^2 at 128×128 pixels and an integration time of 35 ms per pixel. Subsequently a tapping mode AFM image

was measured on the same area using a Si_3N_4 tip (Veeco Instruments, MSCT-AUHW, k=0.5 N/m) at 512×512 pixels. The fragments are 50-100 nm in diameter and 7-50 nm in height.
In location A in the AFM image, two separate membrane fragments are observed lying close together. These fragments cannot be resolved in the optical image. On the other hand, the fluorescence measurement identifies those topographic structures which contain various amounts of light harvesting complexes. The optical spots clearly co-localize with topographic features, although there are also objects in the AFM image which are absent in the optical image. These non-fluorescent objects could well be 'empty' membrane fragments, not containing any LH complexes. Moreover, the spectral information collected on each pixel provides information about the composition of the different membrane fragments. The spectrum emitted by membrane B (Fig. 5.3) closely resembles the LH1 emission spectrum, suggesting that this membrane mainly contains LH1 complexes. In contrast, membrane C shows a spectrum resembling LH2 emission, suggesting a larger number of LH2 complexes in this membrane. For comparison, the measured emission spectra of concentrated solutions of purified LH1 and LH2 complexes were scaled and plotted along with the membrane spectra (dashed curves).

5.3 Combined measurements on single complexes

In the previous section, combined measurements were shown on relatively large structures. These structures provide a clear topographic and optical signal. However, the ultimate test for the AFFM is to perform simultaneous imaging on the single molecule level. Making this step from relatively large structures to single molecules raises a number of additional challenges.

5.3.1 Conflicting scanning requirements for simultaneous imaging

The obtainable lateral resolution of a confocal fluorescence microscope is determined by the size of the diffraction limited excitation focus. When 800 nm laser light is used for excitation, the focus has a diameter of ~ 560 nm and consequently the LH2 complexes are imaged as spots with this diameter. On the other hand, well spaced single proteins imaged by the AFM tip appear as objects with a diameter of $\sim 20-30$ nm, resulting in a difference in lateral resolution between both techniques of roughly a factor of 25. If we stipulate that for both techniques at least 5×5 lateral image pixels are required in a measured 'spot' to reliably identify this spot as a single protein, then the maximum step size (nm's per pixel) in an optical image amounts to 112 nm/pixel (560/5) and in an AFM image ~ 6 nm/pixel (30/5). Any smaller step size, or increase in lateral sampling, results in a more detailed mapping of the objects, and a more reliable identification. In the combined simultaneous imaging mode, both the optical probe and the AFM probe have to detect the individual proteins in a single scan. As a result, the AFM scanning requirement (a maximum of 6 nm/pixel) dictates the scan

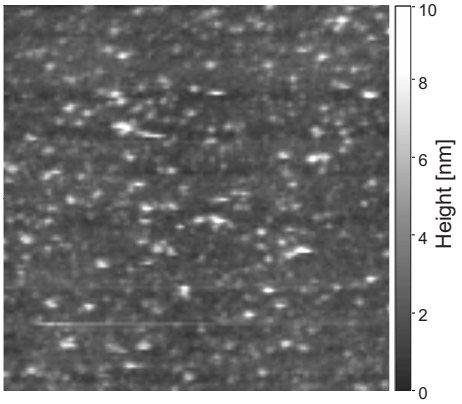

Figure 5.4. AFM image of a glass-PLL substrate with the presence of the oxygen scavenging system containing: 4.5 mg glucose/ml, 216 μg glucose oxidase/ml and 36 μg catalase/ml. Many surface features are present due to non-specific adsorption of these components to the glass.

settings in combined simultaneous imaging, and the optical image is consequently strongly over-sampled.

The typical scan frequencies for both fluorescence and AFM imaging are roughly the same, $\sim$ 2000 Hz, or 0.5 ms/pixel. Consequently the over-sampling in the optical measurement results in a very long illumination of the fluorescent proteins, leading to photobleaching during the scan.

A decrease in excitation intensity can reduce photobleaching, but can also lead to a significant decrease in signal-to-noise ratio in the optical image. This is particularly important in single molecule experiments where the fluorescence intensity is low. Alternatively, an increase in scan frequency would reduce the total illumination time. However, there is a limitation to this frequency. A sample of individual proteins, well separated on the surface, imposes height impulses on the cantilever during scanning. When the AFM is operated in constant force mode, the z-motion piezo has to respond to these impulses in order to keep the interaction force constant. When the scan frequency is too high, the piezo cannot follow the height impulse adequately, resulting in a momentarily higher force and a lower measured height. To prevent this, the scan frequency should be kept below the resonance frequency of the piezo actuator, which is 3 kHz in the AFFM. Therefore, the scan frequency can not be increased significantly above 2 kHz. In addition, an increased scan frequency will also lead to a lower optical signal-to-noise ratio.

As discussed previously, removing the oxygen from the sample solution can strongly reduce photobleaching. The enzymatic oxygen scavenging system consisting of glucose, glucose oxidase and catalase is particularly useful because of its capacity to continuously remove oxygen. However, the significant disadvantage of this system lies in the fact that the molecular weights of glucose oxidase (160 kDa) and catalase (232 kDa) are comparable to the LH2 complex (129 kDa). When this oxygen scavenging system is added to the sample solution the glucose oxidase and catalase bind non-specifically to the glass-PLL substrate. AFM images taken under these conditions show a surface covered with topographic features due to these enzymes (Fig 5.4), making it impossible to distinguish the light harvesting complexes.

Because of the negative effects of the options mentioned above, a different approach has been taken to deal with the conflicting scanning requirements. The fact that the

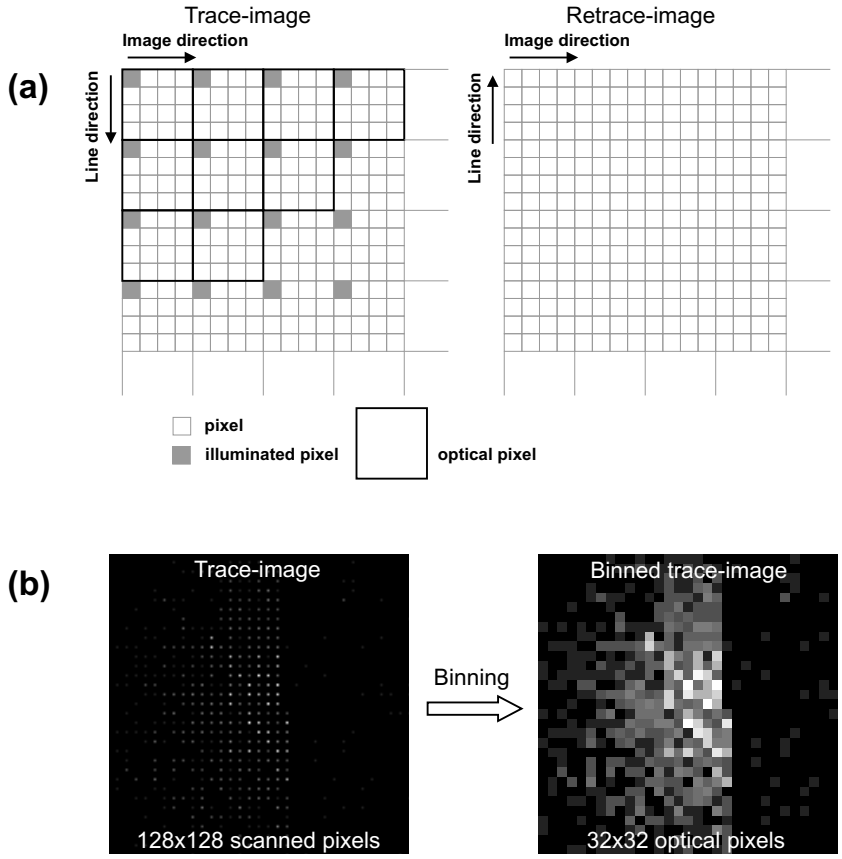

Figure 5.5. (a) Fractional illumination: only a small fraction of the scanned pixels is illuminated during the 'trace-image' and the laser is switched off during the 'retrace-image'. After the measurement, the square sections containing one illuminated pixel can be binned to form a single optical pixel. (b) Demonstration of fractional illumination. The image shows a close-up of a single LH2 complex over a range of 700×700 nm^2. The scan consists of 128×128 pixels of which only one in every four pixels was illuminated. A normal fluorescence image of 32×32 pixels is obtained after binning. The total illumination time is reduced by a factor 32.

optical image is over-sampled allows the reduction of the total illumination time by switching the excitation laser on during only a small fraction of the scanned pixels in the 'trace-image', and leaving the laser off during the 'retrace-image'. To achieve this, a second pattern is generated by the software together with the x,y scan pattern, marking the pixels where the laser should be on. This pattern is synchronously sent to the laser diode controller during scanning. The same pattern can be sent as a gating signal to the APD. After the measurement, the square sections containing one illuminated pixel can be binned to form a single optical pixel. This is illustrated in Fig. 5.5 where, as an example, one in every four scanned pixels is illuminated in the line direction as well as in the image direction. The ratio between the number of scanned pixels and illuminated pixels can be set to any value. In the particular example of Fig. 5.5 the illumination time is reduced by a factor of 32.

5.3.2 Combined sample scanning

For combined measurements on single LH complexes, the sample was prepared in the following manner. The stock solution of purified LH2 complexes was diluted $10^5\times$ in buffer [50mM TRIS (pH 7.8), 100mM KCl, 0.1% lauryldimethylamine oxide (LDAO)]. A droplet of 15 μL of the diluted solution was placed on a PLL coated coverglass. After $\sim$ 5 min of adsorption time, the surface was rinsed with 0.5 mL of buffer in order to remove all unbound proteins. Subsequently, the sample was placed on the AFFM.

Sequential imaging

In order to quickly identify the positions of the individual molecules, a fluorescence image was measured over $\sim 7 \times 7$ μm^2, with the AFM-tip not in contact. Next, a fluorescence image was recorded on one of the molecules with a scan range of approximately 1×1 μm^2 by applying fractional illumination. To measure the AFM image of the same area, the tip was brought into contact with the surface and manoeuvred within the diffraction limited focus as accurately as possible by using the translation stages on which the AFM tripod is positioned as well as by utilizing the manual control of the piezo tube x,y-directions, while observing the scattered light from the tip on the camera (see Fig. 2.7 chapter 2). Subsequently, the AFM image was recorded using the exact same scan settings.
Two examples of these experiments are shown in Fig. 5.6. The fluorescence images clearly show the discrete steps in emission intensity typical for single complex emission, which proves that indeed a single complex is observed. The topographic image of Fig. 5.6(a') shows a prominent feature within the area of the focus. The lateral dimensions of the object are rather large, $\sim 75 \times 110$ nm. A very likely explanation is that this shape reflects the tip shape, since the same oval shape appears for all features in the AFM image. The height of $\sim$ 4 nm does correspond to what is expected from a single LH2 complex. For the feature in Fig. 5.6(b') a height was measured of $\sim$ 3 nm and lateral diameter of $\sim$ 30 nm. These values correspond with expected values for a single LH2 complex (see also Fig. 4.15, chapter 4). Therefore, the measured topographic object was most likely the isolated LH2 complex which were imaged by fluorescence before.

Simultaneous imaging

After the sequential imaging of single LH2 complexes, the same procedure was repeated, however now both images were recorded simultaneously. Fig. 5.7(a') shows a topographic feature within the fluorescence spot. Unfortunately, the emission of the molecule lasted for a very short time. The sizes of the topographic object again correspond quite nicely with expected values (height: $\sim$ 5 nm; lateral dimensions: $\sim 30 \times 40$ nm). In Fig. 5.7(b') a very large object appears, marked by the arrow (height $>$ 12nm, not determined exactly because of clipping; lateral dimensions: $\sim 90 \times 115$ nm). Therefore, this object cannot represent a single complex. It seems

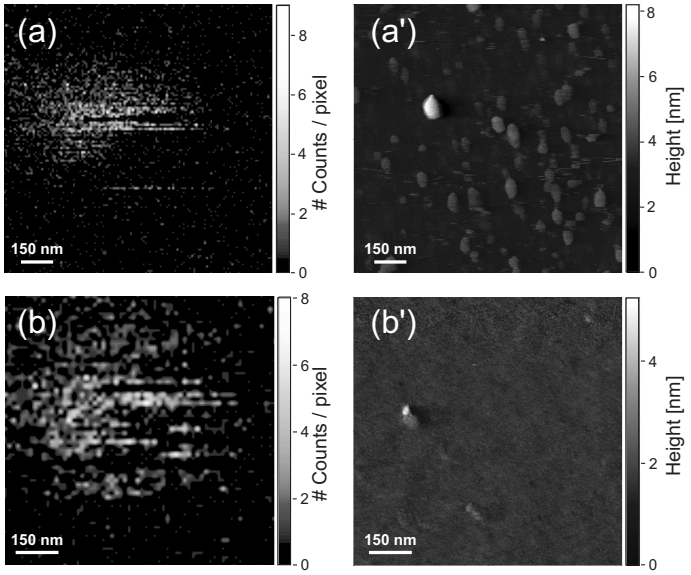

Figure 5.6. Combined sequential images of single LH2 complexes. (a) Fractional illuminated fluorescence image (512 × 512 pixels scanned; 128 × 128 pixels illuminated). (a') AFM image of the same area recorded with the same scan settings. (b) Fluorescence image (512 × 512 pixels scanned; 64 × 64 pixels illuminated). (b') AFM image of the same area recorded with the same scan settings.

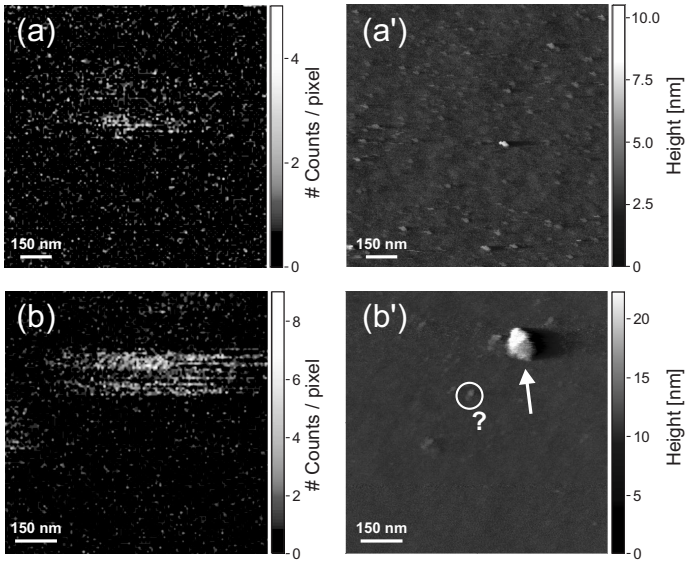

Figure 5.7. Simultaneous imaging of single LH2 complexes. Fractional illumination was applied to record the fluorescence image, scanning 512 × 512 pixels with 128 × 128 pixels illuminated. (a) Fluorescence image showing only a brief period of emission. (a') Simultaneously recorded AFM image. (b) Fluorescence image with clear single molecule emission behavior. (b') Simultaneously recorded AFM image.

more likely that one of the smaller objects on the surface, e.g. the one marked by the circle, is the emitting molecule.

5.3.3 Combined tip scanning

Two additional modes of combined operation were implemented in the instrument. In these modes, the sample is placed in a fixed location, while the tip is scanned in two and three dimensions respectively. The sample is continuously illuminated. In this way, the fluorescence emission is measured as a function of the tip position and interaction force. The two and three dimensional tip scanning modes are demonstrated in this section.

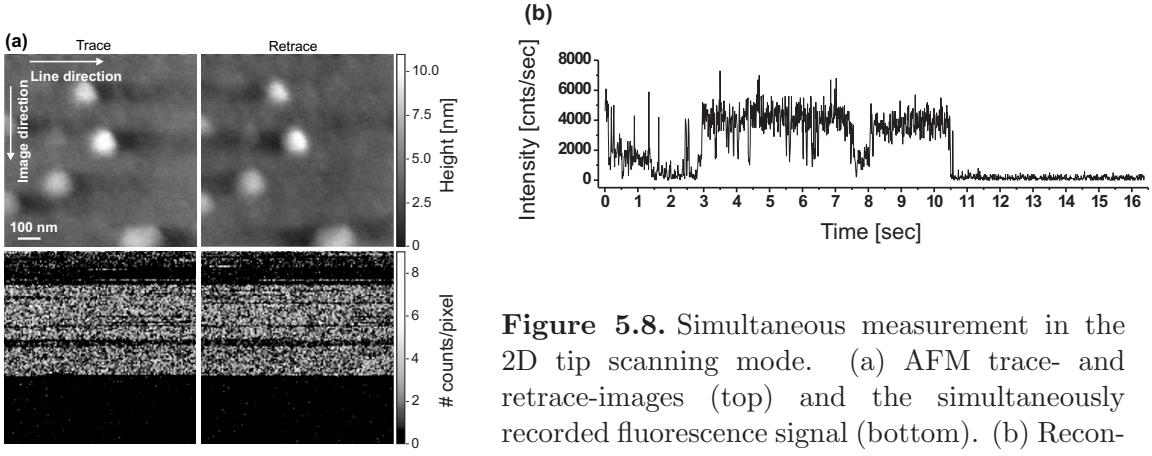

Figure 5.8. Simultaneous measurement in the 2D tip scanning mode. (a) AFM trace- and retrace-images (top) and the simultaneously recorded fluorescence signal (bottom). (b) Reconstructed timetrace of fluorescence emission.

Two-dimensional tip scanning

The sample was prepared in the same way as in the previous experiments. Again an overview fluorescence image was recorded to locate the individual complexes. One of the molecules was selected and placed in the center of the excitation focus. Subsequently, the tip was scanned in tapping mode over an area of 844 × 844 nm through the focus, while simultaneously recording the fluorescence signal as a function of tip position. This is illustrated in Fig. 5.8(a), where the two top images represent the AFM trace- and retrace-images and the two bottom images show the simultaneously detected number of photons as a function of the two-dimensional position of the tip. When the fluorescence signals along the AFM line-directions in the trace- and retrace-images are appended, a single molecule emission timetrace appears (Fig. 5.8(b)), proving that there is only one emitting molecule in the focus. However, in the topographic image, multiple objects are visible with a height of approximately 4 ± 1 nm. Again, the objects have large lateral dimensions ($\sim$ 100nm), which could be attributed to a blunt or polluted tip. Since the height is more or less correct, the objects are probably single LH2 complexes. However, it is not possible to unambiguously identify the emitting object.

In Fig. 5.9 a similar measurement is shown in which only one object appears in the AFM image. The height of the feature is about 10 nm, which is too high for a single LH2 complex. Also the fluorescence timetrace, generated from the collected fluorescence signals, suggests the presence of at least two emitting complexes in the focus.

In both measurements no clear response of the fluorescence at the positions of the topographic objects is observed. Consequently, if one of the objects in the AFM image is indeed the emitting complex, then the emission is not disturbed by the passing tip. In these combined measurements it is absolutely crucial to very accurately position the AFM tip within the excitation focus. Because the scans are taken on an area of only $\sim 1 \times 1\ \mu\mathrm{m}^2$, a slight misalignment causes the tip and focus to 'look' at a different area of the sample. When an assembly of objects is imaged over a larger range, a slight misalignment is not so much of a problem since the pattern of the objects can

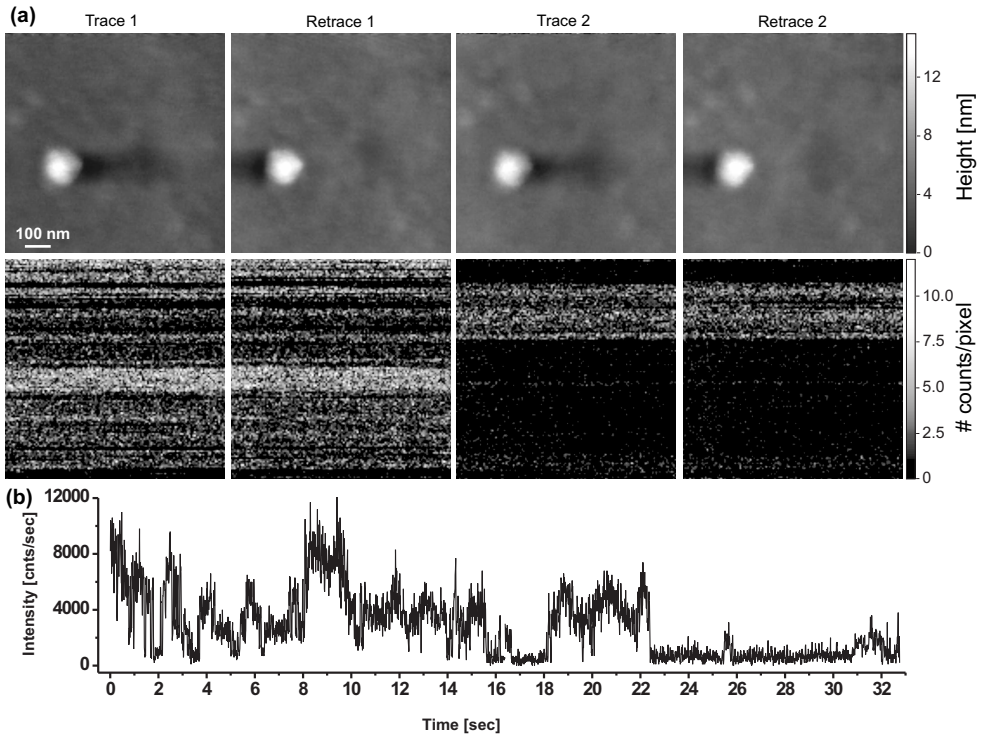

Figure 5.9. Simultaneous measurement in 2D tip scanning mode. Two consecutive scans were taken on the same area, resulting in two trace and two retrace images (a). The fluorescence signal was recorded simultaneously as a function of tip position. (b) Reconstructed timetrace from the optical signal. The fluorescence timetrace shows multiple intensity levels which should correspond to a few emitters. Indeed the dimensions of the observed topographic feature are larger than those expected for a single complex.

be matched in both images.

Fig. 5.10 shows an example of a similar measurement where the tip was accidentally slightly fluorescent (either by picking up some fluorescent material or by a crystal defect in the silicon material). In the first part of the optical image the emission of a single LH2 complex is observed until the molecule photobleaches. In the second part of the image the passage of the fluorescent tip through the focus is visible. The tip is mapping the position of the focus, marked by the gray circle. In the second part of the reconstructed timetrace of Fig. 5.10(b) and enlarged in Fig. 5.10(c), the periodic passage of the tip through the focus is visible with a frequency equal to the line frequency of the scan. In this case, the tip was clearly aligned in the top-right corner of the focus. In the AFM images, no object is found in the center of the focus. The large object is located at the edge of the excitation spot and could in principle be the emitting object, although not optimally excited.

The alignment of the tip with respect to the focus will be discussed in more detail in section 5.4.

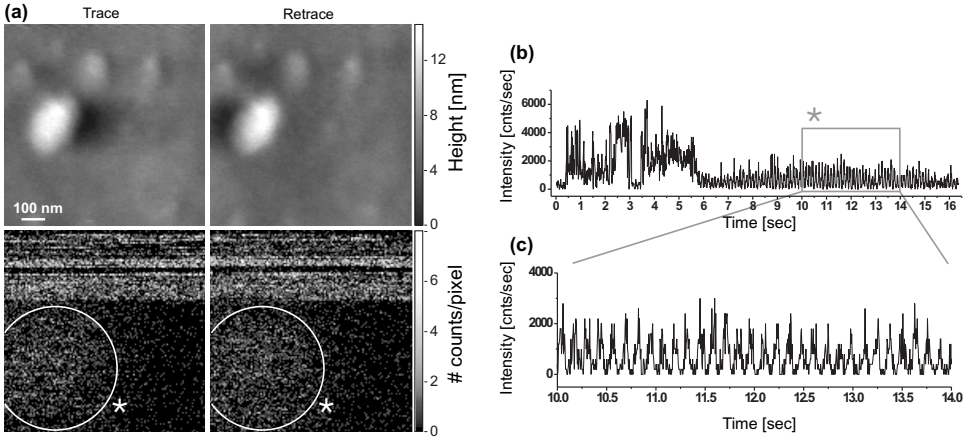

Figure 5.10. 2D tip scanning mode with an accidentally slightly fluorescent tip. (a) The tip maps the position of the focus, marked by the gray circle. The tip was positioned in the upper right corner of the focus before scanning. (b) Reconstructed fluorescence timetrace. (c) Part of the timetrace visualizing the periodic passage of the tip through the focus.

Three-dimensional tip scanning

For the measurement of mechanical properties of objects, interaction forces and adhesion forces, the so-called force-extension mode is generally used (Lee *et al.*, 1994; Hinterdorfer *et al.*, 1996; Rief *et al.*, 1997; Müller *et al.*, 1999a; Willemsen, 1999; Oesterhelt *et al.*, 2000). In this mode, the AFM tip is lowered towards the surface until it makes contact and a certain preset force is reached, after which the tip is retracted again. In this way, a force-extension curve is measured and stored for each image pixel. In the three-dimensional tip scanning mode a fluorescence timetrace is recorded by the APD's and stored along with the force-extension curve for each lateral pixel. In a force-extension measurement, the maximum force that the tip exerts on the sample is well controlled, and the optical response of a molecular system can be observed as a function of the applied force.
This enables the use of the AFM tip as a nanomanipulation tool. Applying a well controlled mechanical pressure on a light harvesting complex will deform the ring structure and therefore alter the interactions between the chromophores in the complex. This could cause a shift in the peak position of the emission spectrum.
The combined force-extension mode is illustrated in Fig. 5.11, where the luminescence of a silicon nitride tip was recorded as a function of the three dimensional tip position. The excitation light ($\lambda = 800$ nm) was focussed on the upper surface of a clean coverglass. The Si_3N_4 tip was ramped perpendicular to the glass surface with a frequency of 1Hz in liquid. At each pixel, a complete force-extension curve was recorded with simultaneous detection of the luminescence of the Si_3N_4 tip material in the optical timetraces. It follows that the maximum luminescence intensity is detected when the tip touches the glass surface. The measurement was performed on 32×32 pixels over a total lateral range of 2.7×2.7 μm^2 and a vertical range of ~ 900 nm. The force-extension curve and the optical trace were sampled 5000 times, yielding a

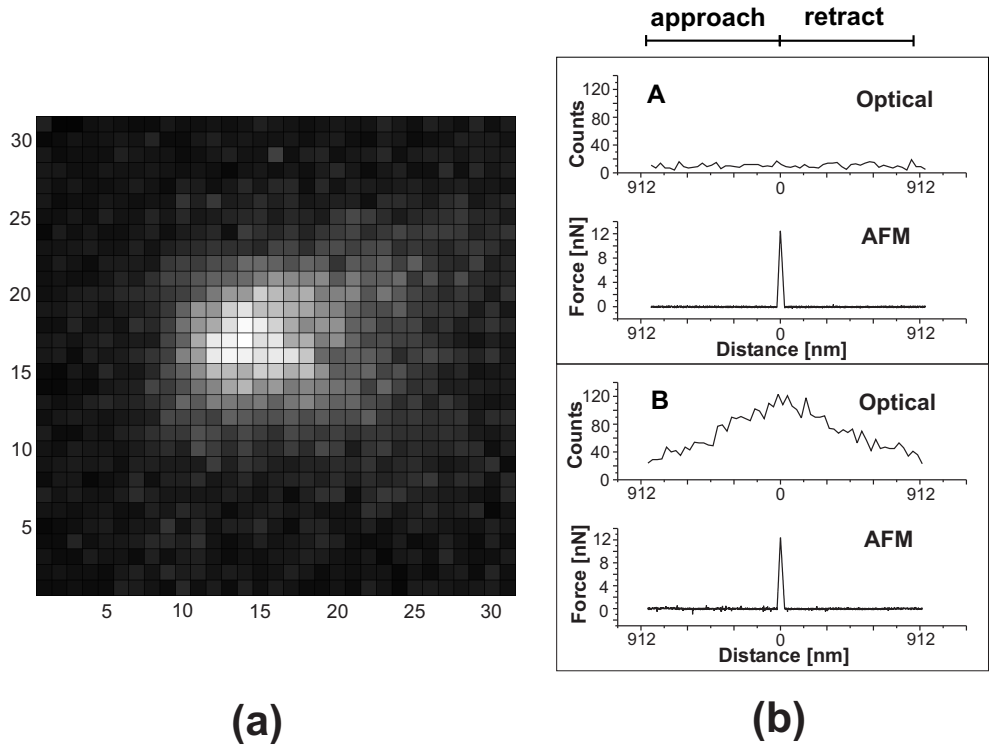

Figure 5.11. Combined force extension measurement, where a complete force-extension curve and optical trace is collected for each lateral pixel. The total lateral range amounts $2.7 \times 2.7\ \mu m^2$. The force extension curves were collected over a vertical range of $\sim 900\ nm$. (a) Image reconstructed from the optical traces. In each pixel the number of photon counts at the moment when the tip touched the surface was plotted. When the Si_3N_4 tip enters the focus, the optical signal increases. (b) Two examples of the total data-set. In location A where the tip approaches outside the focus, no optical signal is recorded. In location B the tip approaches in the center of the focus, resulting in a clear fluorescence signal from the tip material.

time resolution of 0.2 ms. The optical data was binned 100 times afterwards. The image of Fig. 5.11(a) was obtained from the optical traces. The amplitude in the image reflects the number of counts at the moment when the tip touched the surface and reached maximum deflection. The force-extension curve and the corresponding timetrace of two particular pixels are shown in Fig. 5.11(b). In pixel A the tip touches the glass outside the focus and therefore the fluorescence signal is unchanged during the force-extension curve. In pixel B, the tip is lowered in the center of the focus and the fluorescence signal increases until the tip touches the surface.

The duration of such an experiment is determined by the number of lateral pixels and the ramp frequency. In the ideal situation where the AFM tip is perfectly aligned with respect to the molecule and the focus, only a vertical tip movement on a single lateral pixel would be required. However, such a perfect alignment is very hard to achieve and maintain over the duration of the experiment. Therefore, it is necessary to perform the force extension curves over a number of lateral pixels, probing the area

around the molecule. In one of the pixels the actual interaction will take place. The maximum ramp frequency is mainly determined by the cantilever used. To detect and to apply subtle forces in the order of 100 pN, cantilevers with a low spring constant should be used. Cantilevers experience a viscous drag force when they are moved in liquid. When the cantilever moves down it deflects up a bit and when it is moved up it deflects the other way. When the tip touches the surface, the end of the cantilever stops moving. As a result, the drag force is diminished and an additional load is generated on the surface. To minimize this additional load, small rectangular cantilevers, which experience minimal drag forces, are preferable. With a proper choice of cantilever and a minimal ramping distance, pixel frequencies of 65 Hz have been achieved although frequencies of 10-25 Hz are more commonly used (Willemsen, 1999). Finally, in combined experiments, the pixel frequency should be low enough to allow the detection of the optical responses with sufficient signal-to-noise ratio.
A combined force-extension experiment performed over 64×64 pixels at a pixel frequency of 25 Hz would take 164 sec (2.7 min) to measure. Unfortunately, the LH2 complexes photobleach within seconds when dissolved oxygen is present in the solution.

5.4 Discussion

From the experiments described above it is clear that there are a number of important aspects involved in combined experiments on single molecules. These aspects will be discussed in some more detail in this section.

Clean substrate surface

In combined imaging on single molecules, the surface coverage of the molecules should be such that the distance between them is larger than the resolution of the optical microscope. In practice, this corresponds to a surface concentration of about 1 molecule per 1×1 μm^2. A single protein of a few nanometers in size should be unambiguously identifiable on this surface area. Any contamination on the substrate surface will make the identification more difficult.
The fact that a mica surface can be cleaved just before use, exposing an atomically flat and perfectly clean surface, makes it an ideal substrate for AFM measurements. Proteins can often be immobilized directly on this surface, based on charge interactions. However, as mentioned before, mica is not suitable for combined experiments because of its optical properties. The AFFM requires transparent substrates with a thickness of about 170 μm, a prerequisite imposed by the high NA objective. In the experiments, ordinary glass coverslips have been used, cleaned in an acid solution. This provides a surface which is sufficiently clean and smooth (see Fig. 4.13 chapter 4). However, often an additional surface coating has to be added in order to immobilize the proteins. This coating procedure introduces a risk of contaminations or an inhomogeneous distribution of the coating which can lead to an increased surface

roughness. Preparation of a clean functionalized thin transparent substrate is very important for combined experiments on the single molecule level.

Surface functionalization and tip chemistry

So far, the glass slides have been coated with poly-L-lysine, which provides a relatively smooth positively charged surface. The LH complexes immobilize on this surface based on electrostatic charge interaction. The photoluminescence caused by the silicon nitride tip material motivated the use of silicon tips. However, when silicon tips were used for imaging individual molecules it was found that the sharpness of the images rapidly disappeared, often in the first few images taken with a fresh tip. The loss of lateral resolution occurred much faster than with silicon nitride tips. This could either be caused by wear of the tip apex itself or by sample material that non-specifically adheres to the tip.

Silicon nitride possess significant hardness and wear resistance. Silicon on the other hand is known to be a more fragile material and therefore Si tips are more likely to suffer from loss of resolution by wear. However, in order to visualize the individual proteins, the tip sample interaction are reduced to a minimum. Therefore serious mechanical wear of the tip within the first few images can be excluded.

Non-specific adherence of sample material to the tip is a more likely explanation. In this process the surface chemistry of the tip material plays an important role. Under exposure to oxygen, a silicon surface oxidizes to form a native silicon dioxide (SiO_2) layer. This process can take place in air,

$$Si + O_2 \longrightarrow SiO_2,$$

so-called 'dry-oxidation' or in aqueous solution,

$$Si + 2H_2O \longrightarrow SiO_2 + 2H_2,$$

through 'wet-oxidation'. This process will form a layer of SiO_2 on a silicon surface, which is slowly increasing in thickness. Silicon tips that are stored in air and subsequently used in a liquid will therefore have a SiO_2 surface layer. SiO_2 has an isoelectric point (IEP) of 1.8-2.8 (Parks, 1965) which means that silicon oxide is negatively charged at pH values above the IEP. The same material and hence a similar surface charge electrostatically coats the glass coverslip ($\sim$ 72 % SiO_2) with the positively charged poly-L-lysine (PLL). Therefore it seems very likely that the charged Si tip could pick up PLL from the glass surface. This could in itself cause a decrease in image sharpness. However, a layer of PLL on the tip could also trigger the adsorption of the proteins to the tip, and in this way cause a loss of resolution. In addition, the negative charge of the tip could directly cause non-specific protein adsorption (Popat *et al.*, 2003).

The surface chemistry of a Si_3N_4 tip in liquid is somewhat more complex. For virgin

silicon nitride, each surface nitrogen atom can be viewed as being bonded to three silicon atoms (Si_3N) (Senden and Drummond, 1995). In principle, the surface nitrogen atom may undergo a sequence of hydrolysis reactions in aqueous solutions, i.e.

$$\begin{aligned} Si_3N + H_2O &\longrightarrow Si_2\text{-}NH + Si\text{-}OH \\ Si_2\text{-}NH + H_2O &\longrightarrow Si\text{-}NH_2 + Si\text{-}OH \\ Si\text{-}NH_2 + H_2O &\longrightarrow NH_3(aq) + Si\text{-}OH \end{aligned}$$

Therefore the surface of a hydrolysed silicon nitride tip may be composed of silanol (Si-OH), silazane (Si_2-NH) and silylamine (Si-NH_2) surface groups. The relative proportion of each surface group will depend on the extent of the surface hydrolysis. These groups will subsequently form the following acid-base dissociation equilibria (Senden and Drummond, 1995):

$$\begin{aligned} Si\text{-}OH_2^+ &\longleftrightarrow Si\text{-}OH + H_s^+ \\ Si\text{-}OH &\longleftrightarrow Si\text{-}O^- + H_s^+ \\ Si_2\text{-}NH_2^+ &\longleftrightarrow Si_2\text{-}NH + H_s^+ \\ Si\text{-}NH_3^+ &\longleftrightarrow Si\text{-}NH_2 + H_s^+ \end{aligned}$$

The charge density is therefore given by:

$$\sigma = e([Si\text{-}OH_2^+] + [Si_2\text{-}NH_2^+] + [Si\text{-}NH_3^+] - [Si\text{-}O^-])$$

The isoelectric point of colloidal silicon nitride particles, in aqueous solution containing 10 mM NaCl, has been found to vary from pH 4.2 to 7.6 depending on the relative proportions of each surface group. Lin *et al.* (1993) have determined the isoelectric point of their Si_3N_4 tip to be at pH 6.0 ± 0.4, by taking force curves in liquid at various pH values.

The surface chemistry analysis of both Si and Si_3N_4 leads to the conclusion that a silicon tip is much more likely to bear a significant surface charge than a silicon nitride tip. In combination with a PLL coated surface, which is also based on charge interaction, this could very well be an important reason for the rapid loss of resolution with Si tips, as opposed to Si_3N_4 tips.

In order to solve this problem, different surface treatments should be tested such as the exposure to glow discharge or silanization (Müller *et al.*, 1997; Perret *et al.*, 2002).

Control of the oxygen level

The oxygen concentration in the buffer solution has a significant influence on the total emission time of the LH complexes (section 4.1.5, chapter 4) (Bopp *et al.*, 1999). Although fractional illumination strongly reduces the total illumination time during combined imaging and thereby minimizes photobleaching, it is preferable to remove

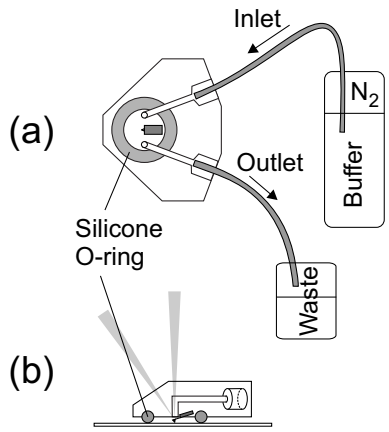

Figure 5.12. Schematic illustration of the closed liquid cell. This cell can be attached to the piezo tube of the AFM. A silicone O-ring is pressed against the substrate, closing the liquid cell. The cantilever is located in the center of the O-ring. An inlet and outlet allow the exchange of buffers in the liquid cell. (a) Top view. (b) Side view.

oxygen from the buffer solution. This is particularly crucial for the combined force-extension mode in which fractional illumination cannot be applied and the measurement times are in general longer. The enzymatic oxygen scavenging system of glucose oxidase, catalase and glucose is very effective in pure fluorescence measurements, but is obviously not applicable in combined experiments (Fig. 5.4).
Alternatively, the buffer solution can be de-oxygenated by bubbling nitrogen gas through the solution. In this case, no additional chemical components have to be added to the solution that could potentially introduce surface contamination. Rutkauskas *et al.* (2004a; 2004b) demonstrated that when oxygen is removed by this procedure, fluorescence emission of single LH2 complexes could be observed for minutes. A requirement in this approach is that the buffer is not exposed to ambient air after de-oxygenation such that oxygen cannot re-dissolve into the solution. Therefore, the AFM has to be equipped with a closed liquid cell in which buffer solutions can be exchanged. Such a liquid cell is present in the AFFM instrument and is schematically shown in Fig. 5.12. When the AFM head with the liquid cell is placed on the glass substrate the silicone O-ring seals the cell. The macroscopic flexibility of the ring permits the scanning motion of the tip and the sample stage. The use of this liquid cell for direct imaging of DNA protein interactions has been described by Van Noort *et al.* (1998; 1999). However, the use of a closed liquid cell can possibly introduce additional drift of the tip relative to the sample surface and the excitation focus. Furthermore, pressing the silicone ring to the glass surface may hamper the alignment of the tip relative to the focus. To which extent these factors hinder proper operation of the microscope has yet to be investigated.

Alignment of tip, focus and object

The accurate alignment of the AFM tip, the excitation focus and the sample is very important in combined imaging on small areas and in manipulation experiments. In the experiments described in this chapter, the tip was aligned within the focus by manually adjusting the translation stages and the lateral directions of the piezo tube, while simultaneously observing the light scattered from the tip on the camera. This procedure is sufficiently accurate to position the tip very close to or actually within

the focus. However, this method is not accurate enough to reliably locate the tip exactly in the center of the focus.
A more reliable alignment can be achieved by application of a method described by Kolodny *et al.* (2001). The intensity profile of the focus is mapped by scanning the tip through the focus and recording the light scattered from the tip apex as a function of tip position. The scattered light is measured through a confocal pinhole by a Si PIN photodiode. In order to separate the tip scattering from the light reflected from the glass surface, the output of the photodiode was directed to a lock-in amplifier, referenced to the drive frequency of the AFM tip. Using the acquired scattering image of the intensity profile, the tip can subsequently be positioned at the coordinates where the tip passed the center of the focus. Consequently the tip is accurately aligned.

Possible near-field effects

Even though no apparent influence of the AFM tip on the fluorescence emission was observed in the experiments, some effects may be expected. The field in the diffraction limited focus is locally perturbed in the presence of an opaque tip. The polarization component of the field parallel to the long axis of the tip can give rise to a locally enhanced field. Large field enhancements can be achieved with metallic tips although also high index dielectric tips can give rise to an enhanced excitation field. This effect is exploited in apertureless near-field scanning optical microscopy (ANSOM), introduced by Zenhausern *et al.* (1994). A review about this field of microscopy is given by Patanè *et al.* (2004). In this type of microscopy, this strongly localized near field at the tip is used to obtain sub-diffraction limit resolution in optical spectroscopy. The enhanced local field in the presence of a tip can boost the fluorescence, however at very short tip-sample distances the fluorescence may be quenched by the tip. The actual fluorescence intensity is therefore a result of the competition between field enhancement and non-radiative transfer to the tip. Azoulay *et al.* (1999) have reported single molecule fluorescence enhancement by a factor of 10 in the presence of a silicon tip. In a separate paper the same authors present a model which describes the fluorescence enhancement as a function of the distance between the tip and the molecule. The model includes both field enhancement and fluorescence quenching. At small distances the quenching is found to be dominant (Azoulay *et al.*, 2000). Trabesinger *et al.* (2003) conducted a study on the fluorescence behavior of single molecules as a function of the position of a silicon nitride tip. They found a shortening of the fluorescence lifetime and a decrease in decay rate in the presence of the tip.
A fivefold fluorescence enhancement for a silicon probe located over a single quantum dot (QD) was achieved by Protasenko *et al.* (2002; 2004). They concluded that the optical enhancements are very sensitive to tip cleaning. Recently, these authors measured up to 7.3 times fluorescence enhancement on single molecules (Protasenko and Gallagher, 2004).
These results from the literature have consequences for the combined measurements on single LH complexes. When a single protein is approached using a silicon tip, a slight fluorescence enhancement may be observed at a certain distance between the

tip and the molecule. However, when the tip starts to mechanically interact with the molecule, the fluorescence emission may be quenched completely. To what extend this will be the case needs to be investigated. Alternatively, the local field enhancement around a silicon tip may be exploited, and the AFFM may be used as a ANSOM.

5.5 Conclusions

In this chapter, the operation of the AFFM has been shown in various modes. All experiments were performed on biological material in a relevant buffer environment. Simultaneously recorded images of 2D crystals of LH2 complexes show a clear correspondence between the optical and the topographic features. The combination of both techniques allows the identification of structures measured by the AFM. A significant increase in the identification capability is provided by the fluorescence spectral detection. Combined AFM and spectral fluorescence imaging not only allows a classification of fluorescing and non-fluorescing objects, but also provides a sensitive means to spectrally distinguish the emitting species.
Combined (simultaneous) measurements on the single molecular level were attempted. The detection sensitivity of both parts of the AFFM is sufficient to perform simultaneous experiments on individual proteins. The sample preparation and tip positioning become the determining factors at this point.

Chapter 6

A prism-based wavelength selector

In order to extend the versatility of the AFFM, an optical fiber connection has been realized between the instrument and a mixed gas Argon-Krypton laser. This type of laser emits wavelengths ranging from 450 to 650 nm. When the laser is operated in the multi-line mode, all wavelengths are produced simultaneously in a single beam. To be able to flexibly select any color, or combination of colors from this beam, a prism-based wavelength selector has been developed. The selected colors emerging from the prism set-up are by design accurately overlaid into a single beam. This results in a precise overlap of the different wavelengths in the focus of a high NA objective. This overlap is important in multi-color co-localization studies using fluorescence imaging and crucial in coincidence analysis by fluorescence cross-correlation spectroscopy. Although the prism set-up is primarily designed with strict overlay requirements to facilitate these spectroscopy techniques, the accurate focus overlap also enables the efficient coupling of multiple wavelengths into the small aperture of a single-mode fiber. In this chapter, the design of the prism set-up is described. The overlay of the wavelengths is tested in a CFM using the scattered light from individual gold nano-beads.

6.1 Introduction

In the study of biological systems there is an increasing interest in observing multiple chromophores simultaneously, for example in co-localization experiments with proteins labelled with different fluorescent dyes and in fluorescence cross correlation spectroscopy (FCCS).
Fluorescence studies with multiple fluorescent probes have been done using multiple excitation wavelengths coming from different lasers (Schwille *et al.*, 1997; Li *et al.*, 2003). The beams from the separate lasers are brought together in a single beam by using dichroic mirrors. However, very small angle differences between the different colors result in a poor overlap of the different foci. For instance, an angle difference of $2.5 \cdot 10^{-3}$ deg causes a displacement in colors of ~ 150 nm using an objective with a focal distance of 3.47 mm. Optimal overlap is, however, important in multi-color co-localization studies using fluorescence imaging and crucial in coincidence analysis

using FCCS.
To circumvent this problem, multi-chromophore experiments have been done with a single excitation wavelength using direct excitation by one-photon absorption as well as using two-photon excitation (Lacoste *et al.*, 2000; Xu *et al.*, 1996; Heinze *et al.*, 2000). However, they all rely on the availability of fluorescent probes with a common excitation wavelength and distinguishable emission characteristics. Another possibility is to use a single beam from a laser operated in multi-line mode to excite a combination of probes with different excitation wavelengths (Winkler *et al.*, 1999). For this technique a very specialized set of optical filters is required to select the desired wavelengths from the beam and strongly suppress all other wavelengths.
In this chapter a simple and elegant set-up is described consisting of two prisms and a retro-reflector which provides both an easy and flexible way of selecting any combination of wavelengths from a laser operated in multi-line mode and an accurate control over the direction of the beams. As a result it enables a precise overlap of the excitation volumes for different colors. These properties make the proposed prism coupling scheme excellent for application in multi-color fluorescence imaging and multi-color FCCS.

6.2 Principle of the prism set-up

A schematic layout of the prism set-up is shown in Fig. 6.1. The laser beam containing multiple wavelengths passes through the first prism (A) which disperses the wavelengths into different directions. The second prism (B) is oriented such that all the wavelengths exit this prism parallel to each other with a spatial separation which is determined by the chosen geometry and size of the prisms.
At position 'S' in the set-up (Fig. 6.1), the unwanted wavelengths are removed from the beam, while the desired wavelengths are transmitted. The selected wavelengths are reflected and displaced downwards by a retro-reflector prism (R), so that these wavelengths pass prisms B and A for the second time. The return path through the same dispersive elements effectively re-overlaps the colors into a single beam.

6.3 Design of the prism set-up

For an optimal configuration of the prisms, there are certain criteria that have to be met and which determine to a large extent the design of the set-up.
In order to create a perfect overlap between the selected wavelengths after the prism set-up, it is crucial that the entrance facet of prism B is parallel to the exit facet of prism A (Fig. 6.1). This determines the rotational orientation of the two prisms with respect to each other.
The amount of spatial separation between the wavelengths after prism B should be sufficient to be able to block specific wavelengths from the complete spectrum. The widest separation is achieved when the spectrum fills the entire entrance facet of prism

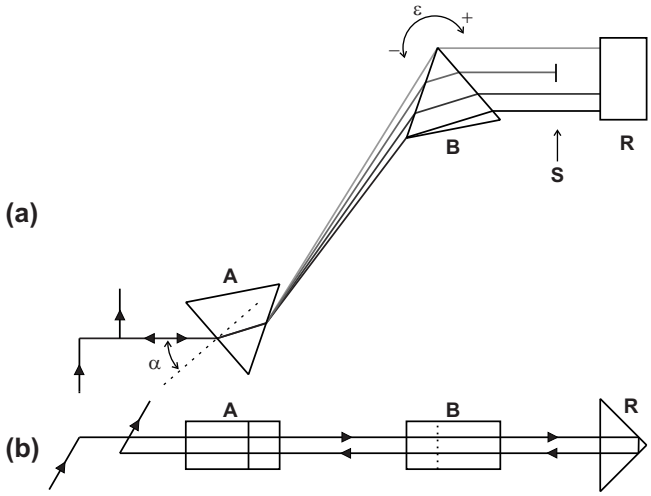

Figure 6.1. The principle of selecting and combining any set of wavelengths using the prism set-up. (a) Top view of the set-up where α represents the angle of incidence of the beam on prism A, ε represents the rotation of prism B with respect to prism A. In the area indicated by 'S' the desired wavelengths can easily be selected. (b) Side view of the set-up. The selected wavelengths are reflected and displaced downwards by the retro-reflector.

B (Fig. 6.1). This criterion determines the lateral position of prism B with respect to prism A.
The only variable left to choose is the angle of incidence α of the laser beam on prism A. This angle of incidence therefore completely determines the ultimate design of the set-up. Important aspects of the set-up, such as the spatial separation between the wavelengths, the size and the transmission of the prism set-up can now be considered as a function of α only. From this analysis, the optimal angle of incidence α can be selected.
We describe a prism set-up consisting of two equal prisms of flint (F2) glass with an apex angle of 60 deg and a side length of 60 mm. The calculations have been done for a full spectrum of 440 nm till 647 nm, corresponding to the emission range of an argon-krypton laser. Calculations of the spatial separation of the spectrum and the size of the set-up have been done using Snell's law and the dispersion relation for F2 glass. The transmission of the set-up has been calculated using the Fresnel equations.

6.3.1 Spatial separation between the wavelengths

The spatial separation that can be achieved after prism B is determined as a function of the angle of incidence α, and plotted in Fig. 6.2 (left axis).
From this figure it can be concluded that smaller angles of incidence result in a larger separation between the wavelengths. The smallest possible angle of incidence is determined by the occurrence of total internal reflection inside the first prism. In the case of F2 glass, this minimum angle is first reached for the shortest wavelength of the spectrum (440 nm) and amounts to 38.82 deg.

6.3.2 Size of the set-up

The distance between the two prisms is determined by the condition that the spectrum should fill the entire entrance facet of prism B. For some angles of incidence α, this

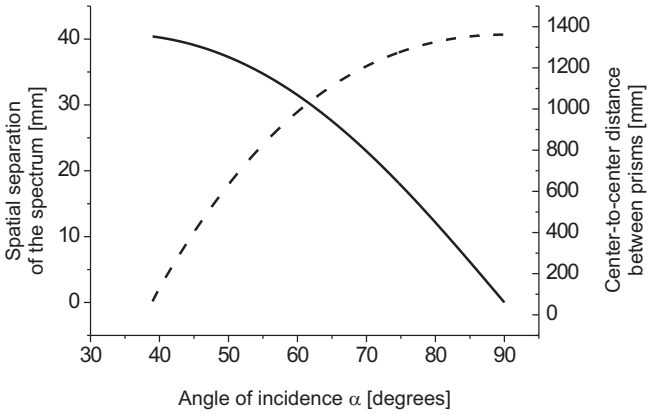

Figure 6.2. (—): spatial separation of the spectrum (440-647 nm) as a function of the angle of incidence on the first prism α for prisms with a side length of 60 mm. (- - -): the size of the prism set-up, represented as the center-to-center distance between the two prisms. For larger angles of incidence the size of the set-up can become very large.

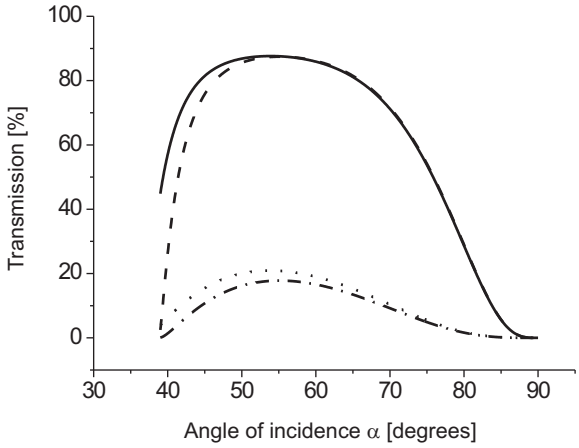

Figure 6.3. Transmission of the prism set-up for the two extreme wavelengths of the spectrum and for s and p polarized light as a function of the angle of incidence α on prism A. (—): p-polarized, 647nm; (- - -): p-polarized, 440nm; ($\cdots$): s-polarized, 647nm; (- $\cdot$ -): s-polarized, 440nm.

can lead to a rather large separation between the prisms. This is demonstrated in Fig. 6.2 (right axis).
In this figure the center-to-center distance between the prisms is plotted as a function of α. It is clear that a small angle of incidence on prism A leads to the smallest set-up and results in the largest spatial separation between the wavelengths.

6.3.3 Transmission of the set-up

The transmission through the prism set-up can be optimized by taking Fresnel-losses at all interfaces properly into account. The losses will depend on the wavelength, the angle of incidence at the interface and the polarization. The transmission of the total set-up for the two extreme wavelengths of the spectrum is plotted in Fig. 6.3 as a function of the angle of incidence α, and for s and p polarizations.
In order to reduce the loss of intensity, the laser beam should be in the p-polarization. For applications where the laser intensity is limiting, an angle of incidence of 55 deg is optimal. However, this decreases the color separation after prism B and significantly increases the size of the set-up (Fig. 6.2).

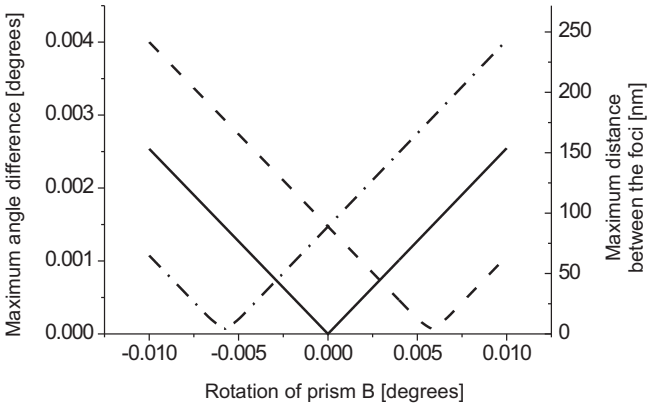

Figure 6.4. Maximum angle difference between the wavelengths emerging from the prism set-up as a function of rotational misalignment ε of prism B. The solid line represents the situation where the two prisms have identical apex angles. The other two lines represent the situation where the apex angle of prism B differs slightly with respect to the apex angle of prism A. (- · -): -0.02 deg; (—): 0 deg; (- - -): 0.02 deg difference in apex angle.

6.4 Prism orientation and beam overlap

When multi-wavelength excitation is applied in confocal fluorescence imaging or in FCS, the excitation volumes of the different wavelengths should overlap in the sample. For the lateral overlap this means that there should be no angle difference between the selected wavelengths in the beam.

Optimal alignment of prism B causes all the beams to exit the prism set-up without any angle difference. However a misalignment of prism B of ± 0.01 deg results in a maximum angle difference of $\sim 2.5 \cdot 10^{-3}$ deg. This is illustrated by the solid line in Fig. 6.4 (left axis) where the maximum angle difference between the wavelengths in the range from 440 nm to 647 nm is plotted as a function of the rotational misalignment ε (defined in Fig. 6.1) of prism B. Even these very small angle differences lead to a significant displacement between the excitation foci (Fig. 6.4 right axis). For the calculation of the maximum distance between the foci we considered an objective with a focal distance of 3.47 mm.

A slight difference in apex angle between prisms A and B also causes an angle difference between different colors. This can almost completely be compensated as is illustrated in Fig.6.4 (dashed and dash-dotted lines) by a small adjustment of the orientation of prism B. In the figure, curves are presented for various differences in the apex angle of prism B with respect to the apex angle of prism A. The corresponding maximum distance between the foci is plotted on the right axis.

6.5 Experimental overlay verification

The prism set-up described in the previous sections has been constructed consisting of two prisms with an apex angle of 60 deg and a side length of 60 mm (Melles Griot, 01PEH019). In order to minimize differences in apex angles, we purchased a single prism from which prism A and B were manufactured after defining one angle as the apex angle. The prism material is flint (F2) glass because of its strong dispersion

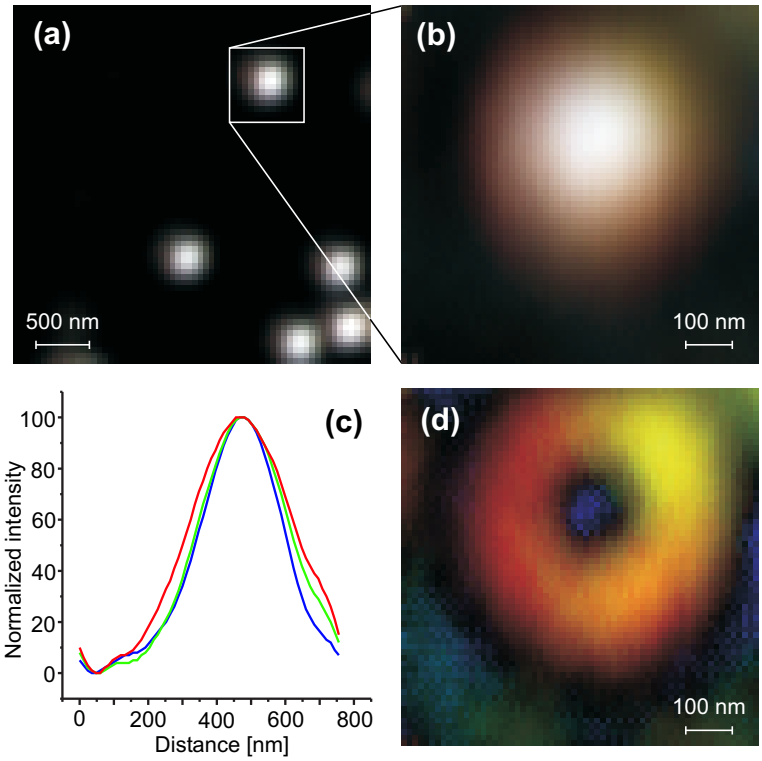

Figure 6.5. Representation of the procedure used for determination of the focus overlap of three different wavelengths selected with the prism set-up (457, 514 and 568 nm). *For a colored version of this figure I refer to the electronic version of this thesis.* (a) Overview of the sample with 25 nm gold beads. (b) RGB image composed of the normalized images of the three different wavelengths. The white color represents an equal contribution of the three imaged point spread functions. This image shows a near perfect overlap of the colors. (c) Contour projection of the three separate PSF images. (d) Difference RGB representation of B. In order to visualize the tiny differences in focus position, the level that is common for the three wavelengths was subtracted for each pixel. Therefore dark now represents an equal contribution of the three wavelengths. This difference RGB image provides a very sensitive representation of the focus overlap, and is very useful in optimizing the alignment of the prism set-up.

in the desired wavelength range. As a retro-reflector we used a right angle prism with a side length of 50.8 mm (Melles Griot, 01PRP035). Both dispersing prisms are placed on rotation stages (Oriel Instruments, 13021) which allow an accurate angular alignment of both prisms with respect to each other. The angle of incidence α on prism A is set to 41 deg to optimize the spectral separation and to minimize the size of the set-up.

This prism set-up is incorporated in a confocal fluorescence microscope with single molecule sensitivity. The overlap in excitation volumes of the different wavelengths has been rigorously tested. For this, three laser lines were selected from the complete spectrum of an argon-krypton laser, namely 457 nm, 514 nm and 568 nm. All other wavelengths were blocked after prism B. The alignment of the prism set-up was

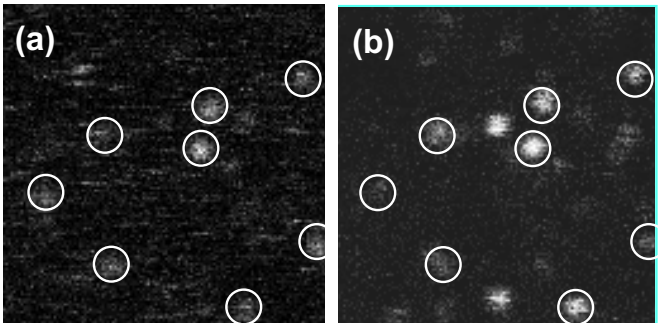

Figure 6.6. Confocal microscopy images from complexes of EGFP labelled XPA and Cy3.5-DNA in a 1% agarose matrix with simultaneous excitation and emission detection of EGFP and Cy3.5 label. Excitation was at 488 nm for EGFP and at 568 nm for Cy3.5. (a) Cy3.5 emission 577-632 nm; (b) EGFP emission 500-550 nm. Image size is 6.2×6.2 μm^2, 128×128 pixels, dwell time 0.5 msec/pixel, excitation 4 kW/cm^{-2} at both 488 nm and 568 nm. Circled positions indicate co-localization of EGFP-XPA and Cy3.5-DNA.

adjusted by the rotation of prism B.

The beam emerging from the prism set-up was directed towards the confocal microscope and focussed on the substrate by a high NA objective (Zeiss, C-Apochromat 63x, 1.20 NA). A gold bead, with a diameter of 25 nm, was used to probe the focus overlap of the beam composed of the three different wavelengths. Imaging the scattered light coming from the bead actually results in an image of the point spread function (PSF) because the bead is small compared to the size of the focus. By imaging the same bead with the three different wavelengths, the overlap of the foci can be determined. This procedure is illustrated in Fig. 6.5. *For a colored version of this figure I refer to the electronic version of this thesis.*

An RGB image of the PSF composed of the normalized images of the three different wavelengths is shown in Fig. 6.5(b). A contour projection of the three separate PSF images (Fig. 6.5(c)) shows a near perfect overlap of the foci. In order to visualize the tiny deviations in focus position, a difference RGB image is shown in Fig. 6.5(d).

The center position of the focus of each wavelength was determined by applying a 2D Gaussian fit to the measured point spread function. The large number of photons that can be collected from a scattering bead allows an accurate determination of the center of the scattering for different colors. From these measurements a maximum center-to-center distance between the three foci was found of 11 ± 1 nm, corresponding to a spatial overlap of better than 95 % of the excitation volumes.

In Fig. 6.6 we demonstrate the application of this prism set-up in a single molecule co-localization experiment, probing protein-DNA binding. The protein (XPA) was labelled with a single enhanced green fluorescent protein (EGFP) and the DNA was labelled with a single Cy-3.5 chromophore. Samples were prepared by embedding the molecules in a small volume of 1% agarose gel. Within this type of matrix both the protein molecules as well as protein-bound DNA become immobilized. Free DNA is

freely diffusing in the gel. For details concerning this experiment we refer to Segers-Nolten *et al.* (2002). We used the prism setup to select and overlap the 488 nm and 568 nm wavelengths from the argon-krypton laser. The emission of the EGFP and Cy3.5 was detected simultaneously on two single photon counting modules (EG&G SPCM-161).
At several positions in the images co-localized spots from EGFP and Cy3.5 can be observed. This co-localization indicates that a DNA molecule is bound by EGFP-XPA. The background signal in the Cy3.5 channel comes from freely diffusing DNA, which is not bound to protein. From the presence of the non-co-localized EGFP-XPA molecules can be concluded that co-localization is not a result of crosstalk from EGFP signal into the Cy3.5 detection channel. From an EGFP-XPA only experiment the crosstalk was determined to be very low. Fig. 6.6 demonstrates that the method for simultaneous multi-color excitation has significant value in single molecule experiments.

6.6 Fiber connection to the AFFM

The availability of visible laser wavelengths in the AFFM, suitable for excitation of all commonly used dyes in biological research, greatly increases the versatility of the instrument. For this purpose, a fiber connection was realized between the Ar-Kr laser with prism set-up and the AFFM.
Although the fiber in-coupling efficiency is considerably higher for a multi-mode fiber than for a single-mode fiber, the latter produces an output beam of much higher quality. The fundamental mode field in a single-mode fiber has a Gaussian distribution, leading to a high quality Gaussian beam shape after collimation. This well defined beam shape is important to create a tight focus in the confocal microscope.
A step index single-mode fiber was selected with a mode field diameter of 3.5 ± 0.5 μm (460HP, step index fiber, operating wavelength 450-600 nm, NA 0.13, Thorlabs Inc., Newton, USA). A low magnification objective ($3.5\times$) is used for in-coupling with an numerical aperture (NA 0.1) that is slightly lower than that of the fiber (NA 0.13). A collimating lens (F260FC-A, NA 0.16, Thorlabs Inc., Newton, USA) connected to the end of the fiber produces a parallel Gaussian output beam.
The excellent overlap of the selected wavelengths, created by the prism set-up, allows easy switching between colors without rigorous realignment and facilitates the coupling of multiple wavelengths simultaneously into the fiber. Fig. 6.7 shows all the wavelengths available in the AFFM through the fiber, as measured by the spectrograph.

6.7 Conclusion

The prism set-up described in this chapter provides a very simple and flexible means of selecting any combination of wavelengths from a laser operated in multi-line mode. The characteristics of such a set-up has been described for the wavelength range from

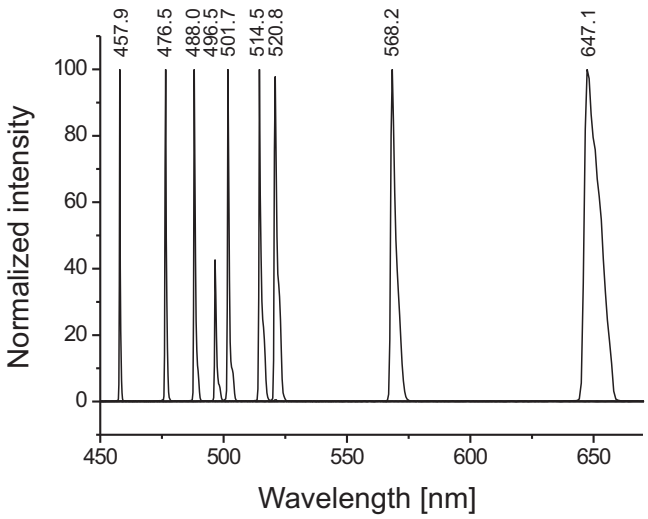

Figure 6.7. Excitation wavelengths available in the AFFM through the optical fiber, as measured by the spectrograph. The exact wavelength values are marked above the peaks. All of these lines can be coupled to the fiber individually or in any combination by means of the prism set-up.

440 nm to 647 nm corresponding to the spectral range emitted by an Argon-Krypton laser. However, the design of the set-up can be optimized for any spectral range. The distance over which the spectrum is spread out can be increased by using larger prisms. This can be important if wavelengths should be separated that are spectrally very close together.

In addition to the flexible selection of wavelengths, the prism set-up also provides a very good overlap of the selected wavelengths. The difference in apex angle between the two prisms is a factor that can be minimized by cutting a single prism in half, and using the same angle as the apex angle. A small remaining difference can be corrected by a rotation of prism B. The position of the retro-reflector is not a critical parameter. This means that the only essential parameter for optimizing the beam overlap is the rotation of prism B and this parameter can be well controlled by placing this prism on an accurate rotation stage.

A prism set-up as described makes it possible to perform multi-color experiments without the need for two or more expensive laser systems, by simply using multiple lines from a single laser. It is a very helpful tool for multi-color experiments where no dye system is available which meets all the criteria needed for single wavelength excitation and where a good overlap of the excitation volumes is crucial.

A fiber connection from this laser combined with the prism set-up to the AFFM allows the use of many commonly used fluorescent dyes in the AFFM. The accurate overlap of the selected colors enables the flexible switching between wavelengths coupled into the fiber, as well as the coupling of multiple wavelengths simultaneously.

Chapter 7

Outlook

This chapter provides an outlook on the potential future applications of the AFFM. The instrument combines two widely used techniques in scientific research. Consequently there are numerous possible applications where a combination of the two offers a significant added value. This outlook focusses on the application on photosynthetic systems, both from a biological as well as a bio-nanotechnological perspective. The fields of 'dip-pen' nanolithography and apertureless near-field scanning optical microscopy are discussed as potentially important application areas of the AFFM.

7.1 Application to photosynthetic systems

The first high resolution AFM images of photosynthetic membranes have recently appeared in the literature revealing the organization of LH complexes that enables the incredibly efficient process of light absorption, energy transfer and eventually ATP production. With the AFFM it becomes possible to relate the structure of the imaged membrane directly to its functioning by observing the optical properties.

The energy transfer between the light harvesting complexes in a membrane can be studied by excitation of the LH2 complexes at a wavelength of 800 nm and observation of the emission emerging from membrane. When all the excitation energy is transferred from the pool of LH2 complexes to the LH1s, only LH1 emission around 890 nm will be observed. Consequently, the amount of LH2 emission provides a measure for the energy transfer efficiency within the membrane. The relative concentrations and spatial organization of the LH2 and LH1 complexes can be determined from the high resolution AFM image of the same membrane and related to the observed emission spectrum. The excitation intensity should be very low in order to prevent singlet-singlet and singlet-triplet annihilation within the membrane (van Amerongen *et al.*, 2000). Observation of the emission under various excitation intensities could provide insight in the saturation levels of the system.

The structural rigidity of individual LH complexes can be investigated, using the AFM tip to apply pushing or pulling forces while simultaneously recording the emission properties. A pushing force can be generated by simply applying a downward pressure on the complex with the tip. To apply a pulling force, the complexes may be modified

with a cysteine or a histidine tag that can bind to the AFM tip. These type of experiments may provide optical evidence for the difference in flexibility between LH1 and LH2 complexes observed in AFM measurements (Bahatyrova *et al.*, 2004a). Observation of the emission of LH complexes while they are being imaged in tapping or contact mode can give direct insight into the effect of certain imaging forces on the protein integrity. Additionally, fluorescence quenching or enhancement effects due to the tip may be observed. These experiments can be performed in the 2D and 3D tip scanning modes presented in chapter 5.

The AFFM may be used to study single molecule fluorescence resonance energy transfer (FRET) experimentally. Either the donor or acceptor molecule can be attached to the AFM probe (perhaps through a suitable spacer molecule) while the other part of the FRET pair is attached to the substrate. The distance between donor and acceptor molecule can be varied accurately by moving the AFM tip. In this way, the distance dependance of energy transfer can be determined directly at the single molecule level. Any suitable FRET pair can be used in such an experiment, however in the line of this research a combination of LH1 and LH2 is particularly interesting.

The unique energy transfer properties of light harvesting complexes may be exploited in biophysical engineering to produce biomolecular photonic wires. This requires the accurate arrangement of the LH complexes in linear arrays. The AFM can play a role in aligning the complexes and imaging the result, while the optical properties can be studied with the fluorescence microscope (see also section 7.4 and section 7.3).

7.2 Quantum dots as a model system

In order to improve and further test various modes of simultaneous operation on single molecules and to study the influence of the AFM tip on the fluorescence emission it is preferable to initially use a suitable model system that is more robust than individual proteins. Quantum dots (QD) are very suitable as a model system for multiple reasons. First, QDs have an excellent photostability which significantly reduces the problem of photobleaching and provides more time for the experiments. Second, QDs are available in a range of sizes comparable to that of a large macromolecule or protein, ranging from 10 to 20 nm. Third, the emission properties of QDs strongly depend on the particle size. The smallest QDs emit at $\sim$ 525 nm and the largest at $\sim$ 800 nm. The extinction coefficient of the dots and consequently their brightness increases with the size. Therefore, in the combined experiments QDs can be purpose selected: 'large' QDs to provide a relatively large topographical signature with a bright fluorescence signal for initial testing down to small QDs for a topographical signal and fluorescence intensity comparable to a single protein. Fourth, QDs are mechanically more robust than proteins, which reduces the risk of inducing damage during the experiments.

An example of a simultaneous measurement on single QDs is shown in Fig. 7.1. For this experiment, QDs with an emission wavelength of 655 nm were used (QDot655 Streptavidin Conjugate, Quantum Dot Corporation, Hayward, USA). The stock solution was diluted $10^4\times$ in buffer (50 mM TRIS HCl, pH 7.5, 150 mM KCl), and

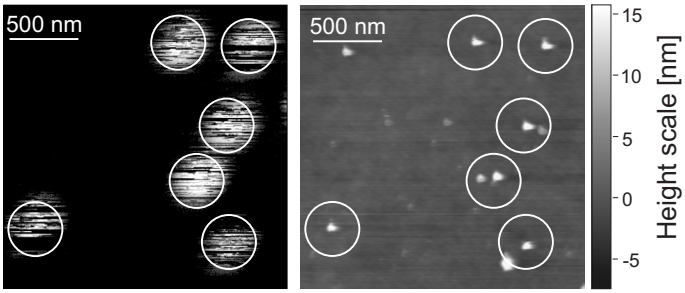

Figure 7.1. Simultaneous measurement on individual quantum dots (QD655) on glass coated with PLL. The quantum dots serve as a model system for individual proteins.

subsequently immobilized on a PLL coated coverglass. The measurement was performed in the same buffer. The QDs were excited with 488 nm laser light from the Ar-Kr laser, using the wavelength selector presented in chapter 6.
Because of their suitable size and emission properties, quantum dots form a proper intermediate for the transition from simultaneous measurements on relatively large and brightly fluorescent structures such as membranes and crystals down to individual proteins.

7.3 'Dip-pen' nanolithography

Dip-pen nanolithography (DPN) is a relatively new scanning-probe based technique for direct fabrication of nanostructures on surfaces, introduced in 1999 (Piner *et al.*, 1999). DPN uses an AFM tip as a 'pen' to write surface patterns with sub-100 nm dimensions with various types of 'ink' materials. The principle of DPN is schematically illustrated in Fig. 7.2. The technique enables the production of nano-scale dot arrays and lines in any pattern. The limit to the feature size is determined by the tip geometry, the water meniscus properties and the chemical properties of the ink and the substrate. Linewidths in the order of 15 nm have been reported with 16-mercaptohexadecanoic acid (MHA) molecules written on an atomically flat terrace of an Au(111) substrate (Hong *et al.*, 1999).
Interestingly, a number of groups have reported the patterning of proteins using DPN onto various surfaces, among which SiO_2 (Noy *et al.*, 2002; Lim *et al.*, 2003; Pena *et al.*, 2003). With its capacity of nano-patterning biomolecules, DPN has the potential to revolutionize the technology of surface based biomolecular assays. The AFFM could be particularly suitable for this application. Using the AFFM in a dip-pen mode, various fluorescently tagged proteins could be patterned in a nano array and directly probed with the highly sensitive fluorescence microscope. Multiple fluorescent markers can be excited simultaneously using the prism set-up and the emission can be spectrally detected with single molecule sensitivity.
The DPN technique can be used as an approach to create lines of light harvesting complexes to fabricate biomolecular photonic wires as briefly discussed at the end of section 7.1. Tests can be performed with direct writing of LH complexes onto a suitable substrate. Alternatively, DPN can be used to write narrow lines of smaller molecules which can be used as a template for the attachment of LH complexes.

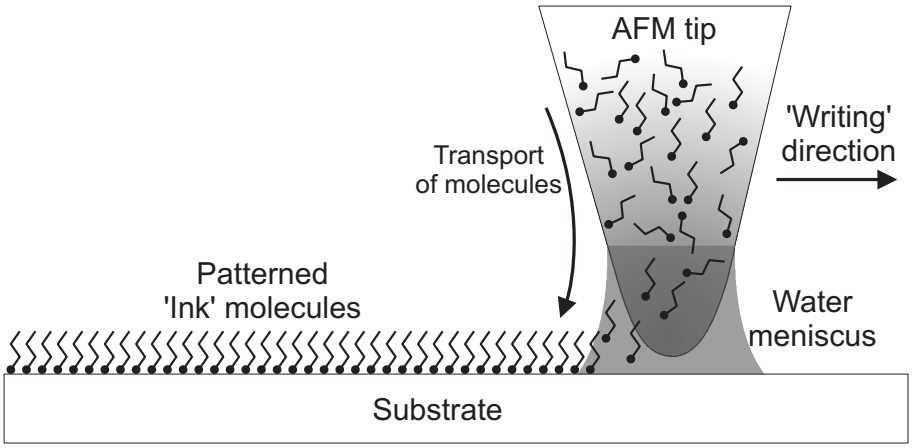

Figure 7.2. Schematic illustration of dip-pen nanolithography (DPN). A water meniscus forms between the 'inked' AFM tip and the substrate. Capillary forces transport the 'ink' molecules from the AFM tip to the substrate surface. DPN is used to 'write' sub-100 nm structures of various materials onto various surfaces. This figure was adapted from Piner *et al.* (1999).

In this way, LH complexes can be aligned indirectly by using this nanolithography technique. DPN can even be used to fabricate metal nanostructures (Li *et al.*, 2001; Maynor *et al.*, 2001; Porter *et al.*, 2002). Nano sized gold lines can also be used as a template for aligning cysteine labelled LH complexes.
An extensive overview of the potential and the applications of DPN is given in a recent review of the technique (Ginger *et al.*, 2004). The modularity and flexibility of the AFFM make the instrument suitable for dip-pen nanolithography. The combination with single molecule optical detection enables direct observation and spectral analysis of the nano-scale patterns which provides a significant added value to conventional DPN.

7.4 Apertureless near-field microscopy

As discussed in the section 5.4 of chapter 5, around the apex of an illuminated metallic or dielectric AFM tip an enhanced near field can occur. This effect is used in apertureless near-field scanning optical microscopy (ANSOM) where this strongly localized near-field is used to obtain an optical resolution below the diffraction limit (Zenhausern *et al.*, 1994; Patanè *et al.*, 2004). The AFFM contains all the functionality to be used as an ANSOM. A silicon or metal coated AFM tip can be directly illuminated by the laser focus produced by the microscope objective. Alternatively an objective type total internal reflection fluorescence microscope (objective type TIRFM) configuration can be used (Axelrod, 1989; Protasenko *et al.*, 2004; Protasenko and Gallagher, 2004) to obtain a homogeneous near-field illumination with the polarization along the long axis of the tip, interacting only with the very end of the tip apex. This reduces scattering from the tip/cantilever geometry.

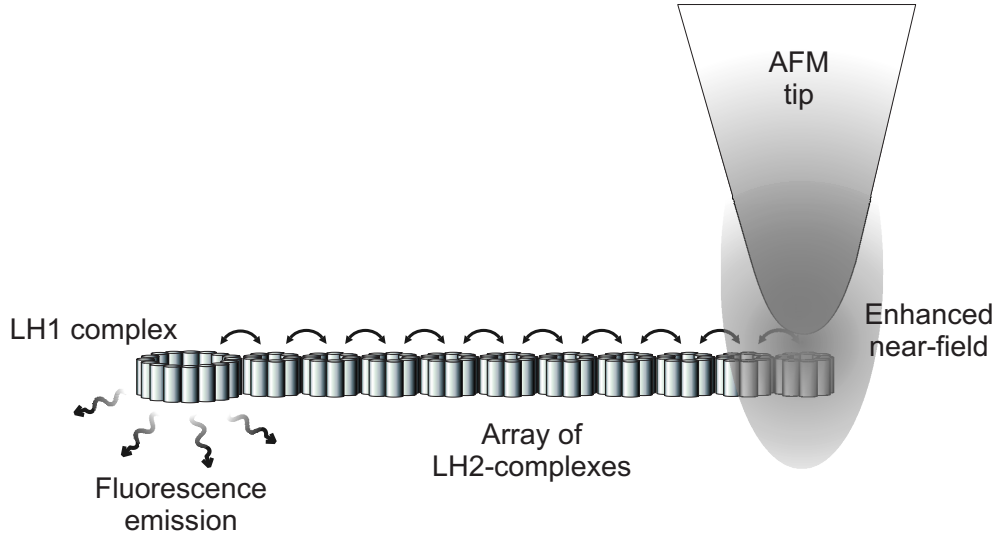

Figure 7.3. Schematic illustration of an energy migration experiment on a linear array of LH2 complexes with an LH1 complex at the end. Local field enhancement around an AFM tip can be used to locally excite the specimen. In by observing the LH1 emission while exciting at different locations, energy transfer over various distances can be studied.

Field enhancement and fluorescence quenching due to the presence of the tip can be studied using the 2D and 3D tip scanning modes, discussed in chapter 5. ANSOM imaging can be performed by scanning the sample in between the objective and the tip, when the tip is well aligned on the optical axis.

The enhanced near-field around the tip apex can be used to obtain a more localized excitation. This can be particularly useful in energy transfer studies on photosynthetic membranes and engineered arrays of light harvesting complexes. This is schematically illustrated in Fig. 7.3, where an array of LH2 complexes is shown with one LH1 complex at the end of the line. The location of excitation can be controlled using the enhanced near-field around the tip. Exciting the array at one end, the excitation energy can migrate back and forth through the array. Once the excitation energy reaches the LH1 ring at the other end, back transfer towards the LH2s is less likely because of the lower excited state energy of LH1. The energy will be released by emission of a fluorescence photon. By observing the LH1 fluorescence emission resulting from an excitation at a known location, the energy transfer processes over various distances can be studied.

We have conducted initial calculations on the obtainable field enhancement around the apex of a gold coated tip based on analytical expressions of the local field (Salomé, 2003). In these calculations the tip was modelled as gold ellipsoid in a water environment and the polarization of the light was assumed to be parallel to the long axis of the ellipsoid. These calculations showed that for every excitation wavelength one specific value of the aspect ratio of the ellipsoid yields an optimal field enhancement. This is illustrated in Fig. 7.4(a) where the calculated intensity enhancement at the tip is shown in a logarithmic color scale as a function of the wavelength and the aspect

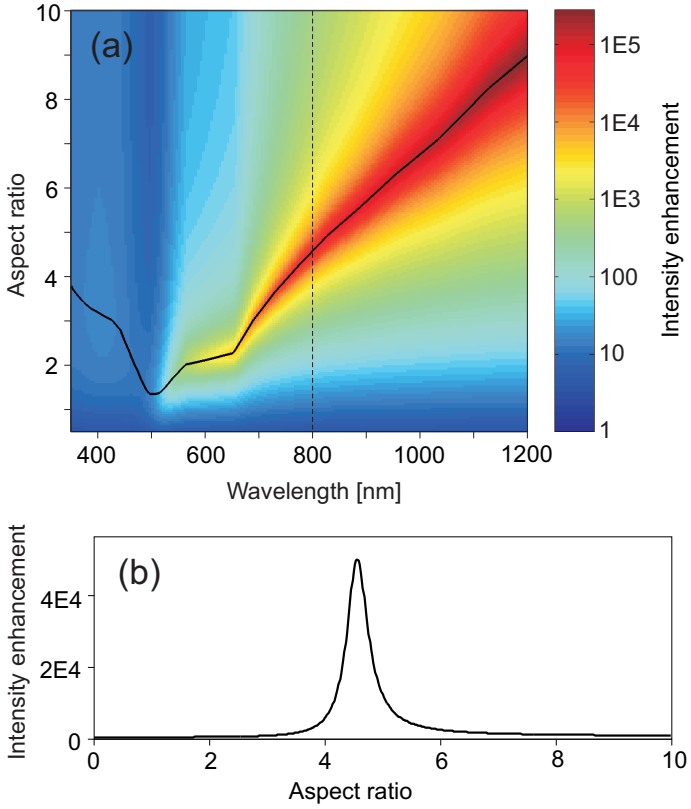

Figure 7.4. (a) Calculated intensity enhancement at the apex of a gold ellipsoid in water as a function of the wavelength and the aspect ratio of the ellipsoid. The polarization of the light is assumed to be along the long axis of the ellipsoid. The solid black line marks the aspect ratio with the highest intensity enhancement for each wavelength. (b) Intensity enhancement as a function of the wavelength under illumination with 800 nm light. A clear optimal aspect ratio of 4.6 is found for this wavelength.

ratio of the ellipsoid. The solid black line marks for each wavelength the aspect ratio with the highest field enhancement. The intensity enhancement for 800 nm is plotted as a function of the aspect ratio in Fig. 7.4(b), showing a clear peak at an aspect ratio of 4.6. The values of the intensity enhancement in Fig. 7.4 are the maximum attainable enhancement factors, based on the material properties (dielectric constants of the tip material and the medium around the tip) and the shape of the ellipsoid. However, for a more accurate estimation radiation damping caused by the volume of the ellipsoid should be taken into account.

In Fig. 7.5(a) the calculated intensity distribution around a tip with the optimal aspect ratio for 800 nm (4.6) is shown in a logarithmic color scale relative to the tip size. Fig. 7.5(b) shows the intensity of the field as a function of the distance from the tip along the dotted line in Fig. 7.5(a) for various sizes of the ellipsoid, all with an aspect ratio of 4.6. The enhancement values in this graph were calculated with the volume dependant damping taken into account. Obviously, the smallest ellipsoid (short axis: 1 nm; long axis: 4.6 nm) generates the highest intensity enhancement (close to the maximum enhancement of 50000). The field around this ellipsoid also decays rapidly. The enhanced field around larger ellipsoids experiences more damping and the maximum enhancement is consequently lower. However, the enhanced field extends over longer distances.

To obtain a strong field enhancement for ANSOM imaging it is desired to have an accurate control over the aspect ratio of the tip. For experiments on LH complexes such as presented in Fig. 7.3, a tip with an aspect ratio of 4.6 would be most suitable. Yu

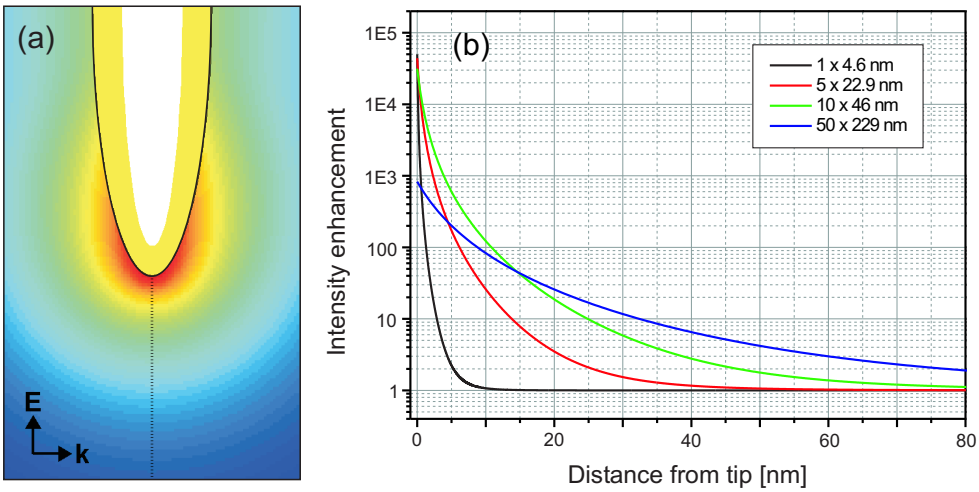

Figure 7.5. (a) Intensity distribution around a tip with an aspect ratio of 4.6. (b) Intensity enhancements as a function of the distance from the apex of the ellipsoid, along the dotted line in (a). The curves were calculated for ellipsoids with an aspect ratio of 4.6, however with different sizes (short axis × long axis). Small ellipsoids generate the highest enhancement and the intensity decays over the shortest distance.

et al. (1997) demonstrated that gold nanorods can be electrochemically synthesized with relatively well controlled aspect ratios, and a mean short axis of 10 nm. Such a gold nanorod with the proper aspect ratio attached to a silicon tip would form an ideal well controlled probe for ANSOM experiments.

References

Albrecht T. R., and Quate C. F., "Atomic resolution imaging of a non-conductor by atomic force microscopy", *J. Appl. Phys.*, **62**(7), 2599–2602. 1987.

van Amerongen H., Valkunas L., and van Grondelle R., *Photosynthetic excitons*. World Scientific Publishing Co. Pte. Ltd. 2000.

Amos W. B., White J. G., and Fordham M., "Use of confocal imaging in the study of biological structures", *Appl. Opt.*, **26**(16), 3239–3243. 1987.

Anczykowski B., Kruger D., Bancock K. L., and Fuchs H., "Basic properties of dynamic force spectroscopy with the scanning force microscope in experiment and simulation", *Ultramicroscopy*, **66**, 251–259. 1996.

Angerhofer A., Bornhäuser F., Gall A., and Cogdell R.J., "Optical and optically detected magnetic resonance investigation on purple photosynthetic bacterial antenna complexes", *Chem. Phys.*, **194**(2-3), 259–274. 1995.

Arimoto A., Ojima M., Chinone N., Oishi A., Gotoh T., and Ohnuki N., "Optimum Conditions for the High Frequency Noise Reduction Method in Optical Videodisk Players", *Applied Optics*, **25**(9), 1398–1403. 1986.

Arimoto A., and Ojima M., "Diode Laser Noise at Control Frequencies in Optical Videodisk Players", *Applied Optics*, **23**(17), 2913–2920. 1984.

Axelrod D., "Total internal-reflection fluorescence microscopy", *Meth. Cell Biol.*, **30**, 245–270. 1989.

Aydinli A., Serpengüzel A., and Vardar D., "Visible photoluminescence from low temperature deposited hydrogenated amorphous silicon nitride", *Solid State Commun.*, **98**(4), 273–277. 1996.

Azoulay J., Bébarre A., Richard A., and Tchénio P., "Field enhancement and apertureless near-field optical spectroscopy of single molecules", *J. Microscopy*, **194**, 486–490. 1999.

Azoulay J., Bébarre A., Richard A., and Tchénio P., "Quenching and enhancement of single-molecule fluorescence under metallic and dielectric tips", *Europhys. Lett.*, **51**(4), 374–380. 2000.

Bahatyrova S., Frese R. N., van der Werf K. O., Otto C., Hunter C. N., and Olsen J. D., "Flexibility and size heterogeneity of the LH1 light harvesting complex revealed by atomic force microscopy", *J. Biol. Chem.*, **279**(20), 21327–21333. 2004^a.

Bahatyrova S., Frese R. N., Siebert C. A., Olsen J. D., van der Werf K. O., van Grondelle R., Niederman R. A., Bullough P. A., Otto C., and Hunter C. N., "The native architecture of a photosynthetic membrane", *Nature*, **430**, 1058–1062. 2004^b.

Binnig G., Rohrer H., Gerber Ch., and Weibel E., "Surface studies by scanning tunneling microscopy", *Phys. Rev. Lett.*, **49**(1), 57–61. 1982^a.

Binnig G., Rohrer H., Gerber Ch., and Weibel E., "Tunneling through a controllable vacuum gap", *Appl. Phys. Lett.*, **40**, 178–180. 1982^b.

Binnig G., Quate C. F., and Gerber Ch., "Atomic force microscope", *Phys. Rev. Lett.*, **56**(9), 930–933. 1986.

Bonnell D., *Scanning probe microscopy and spectroscopy.* second edn., Wiley-VCH. 2001.

Bopp M. A., Jia Y., Li L., Cogdell R. J., and Hochstrasser R. M., "Fluorescence and photobleaching dynamics of single light-harvesting complexes", *Proc. Natl. Acad. Sci. USA*, **94**, 10630–10635. 1997.

Bopp M. A., Sytnik A., Howard T. D., Cogdell R. J., and Hochstrasser R. M., "The dynamics of structural deformations of immobilized single light-harvesting complexes", *Proc. Natl. Acad. Sci. USA*, **96**, 11271–11276. 1999.

van den Bout D. A., Yip W.-T., Hu D., Fu D.-K., Swager T. M., and Barbara P. F., "Discrete intensity jumps and intramolecular electronic energy transfer in the spectroscopy of single conjugated polymer molecules", *Science*, **277**, 1074–1077. 1997.

Brakenhoff G. J., Blom P., and Barends P., "Confocal scanning light microscopy with high aperture immersion lenses", *J. Microscopy*, **117**(2), 219–232. 1979.

Cleveland J. P., Anczykowski B., Schmid A. E., and Elings V. B., "Energy dissipation in tapping-mode atomic force microscopy", *Appl. Phys. Lett.*, **72**(20), 2613–2615. 1998.

Cogdell R. J., Hipkins M. F., MacDonald W., and Truscott T. G., "Energy transfer between the carotenoid and the bacteriochlorophyll within the B-800-850 light-harvesting pigment-protein complex of *Rhodopseudomonas sphaeroides*", *Biochim. Biophys. Acta*, **634**, 191–202. 1981.

Cogdell R. J., Gardiner A. T., Roszak A. W., Law C. J., Southall J., and Isaacs N. W., "Rings, ellipses and horseshoes: how purple bacteria harvest solar energy", *Photosynth. Res.*, **81**, 207–214. 2004.

Czajkowsky D. M., and Shao Z., "Submolecular resolution of single macromolecules with atomic force microscopy", *FEBS Letters*, **430**, 51–54. 1998.

Davidovits P., and Egger M. D., "Scanning laser microscope", *Nature*, **223**, 831. 1969.

Drake B., Prater C. B., Weisenhorn A. L., Gould S. A. C., Albrecht T. T., Quate C. F., Canell D. S., Hansma H. G., and Hansma P. K., "Imaging crystals, polymers and processes in water with the atomic force microscope", *Science*, **243**(10), 1586–1589. 1989.

Dunn R. C., "Near-field scanning optical microscopy", *Chem. Rev.*, **99**(10), 2891–2927. 1999.

Ebenstein Y., Mokari T., and Banin U., "Fluorescence quantum yield of CdSe/ZnS nanocrystals investigated by correlated atomic-force and single-particle fluorescence microscopy", *Appl. Phys. Lett.*, **80**, 4033–4035. 2002.

Fotiadis D., Scheuring S., Müller S. A., Engel A., and Müller D. J., "Imaging and manipulation of biological structures with the AFM", *Micron*, **33**, 385–397. 2002.

Fotiadis D., Liang Y., Filipek S., Saperstein D. A., Engel A., and Palczewski K., "The G protein-coupled receptor rhodopsin in the native membrane", *FEBS Letters*, **564**, 281–288. 2004[a].

Fotiadis D., Qian P., Philippsen A., Bullough P. A., Engel A., and Hunter C. N., "Structural analysis of the reaction center light-harvesting complex I photosynthetic core complex of *Rhodospirillum rubrum* using atomic force microscopy", *J. Biol. Chem.*, **279**(3), 2063–2068. 2004[b].

Foubert P., Vanoppen P., Martin M., Gensch T., Hofkens J., Helser A., Seeger A., Taylor R. M., Rowan A. E., Nolte R. J. M., and Schrijver F.C. De, "Mechanical and optical manipulation of porphyrin rings at the submicrometer scale", *Nanotechnology*, **11**, 16–23. 2000.

Fraser N. J., Hashimoto H., and Cogdell R. J., "Carotenoids and bacterial photosynthesis: The story so far...", *Photosynth. Res.*, **70**, 249–256. 2001.

Frederix P. L. T. M., Asselbergs M. A. H., van Sark W. G. J. H. M., van den Heuvel D. J., Hamelink W., de Beer E. L., and Gerritsen H. C., "High sensitivity spectrograph for use in fluorescence microscopy", *Appl. Spectr.*, **55**(8), 1005–1012. 2001.

Frisbie C. D., Rozsnyai L. F., Noy A., Wrighton M. S., and Lieber C. M., "Functional group imaging by chemical force microscopy", *Science*, **265**, 2071–2074. 1994.

Fritzsch G., Koepke J., Diem R., Kuglstatter A., and Baciou L., "Charge separation induces conformational changes in the photosynthetic reaction centre of purple bacteria", *Acta Crystallogr.*, **D58**, 1660–1663. 2002.

Frohn J. T., Knapp H. F., and Stemmer A., "True optical resolution beyond the Rayleigh limit achieved by standing wave illumination", *Proc. Natl. Acad. Sci. USA*, **97**(13), 7232–7236. 2000.

Furman B. F., Christman J., Kearny M., Wojcik F., and Tortonese M., "Battery-operated atomic force microscope", *Rev. Sci. Instrum.*, **69**(1), 215–220. 1998.

Giessibl F. J., and Trafas B. M., "Piezoresistive cantilevers utilized for scanning tunneling and scanning force microscope in ultrahigh vacuum", *Rev. Sci. Instrum.*, **65**(6), 1923–1929. 1994.

Ginger D. S., Zhang H., and Mirkin C. A., "The evolution of dip-pen nanolithography", *Angew. Chem. Int. Ed.*, **43**, 30–45. 2004.

Gittes F., and Schmidt C. F., "Thermal noise limitations on micromechanical experiments", *Eur. Biophys. J.*, **27**, 75–81. 1998.

Gradinaru C. C., Martinsson P., Aartsma T. J., and Schmidt T., "Simultaneous atomic force and two-photon fluorescence imaging of biological specimens in vivo", *Ultramicroscopy*, **99**, 235–245. 2004.

Hansma P. K., Cleveland J. P., Radmacher M., Walters D. A., Hillner P.E., Bezanilla M., Fritz M., Vie D., Hansma H. G., Prater C. B., Massie J., Fukunaga L., Gurley J., and Elings V., "Tapping mode atomic force microscopy in liquids", *Appl. Phys. Lett.*, **64**(13), 1738–1740. 1994.

Harada Y., Sakurada K., Aoki T., Thomas D. D., and Yanagida T., "Mechanochemical coupling in actomyosin energy transduction studied by *in Vitro* movement assay", *J. Mol. Biol.*, **216**, 49–68. 1990.

Hecht B., Bielefeldt H., Inouye Y., Pohl D. W., and Novotny L., "Facts and artifacts in near-field optical microscopy", *J. Appl. Phys.*, **81**(6), 2492–2498. 1997.

Heinze K. G., Koltermann A., and Schwille P., "Simultaneous two-photon excitation of distinct labels for dual-color fluorescence cross-correlation analysis", *Proc. Natl. Acad. Sci. USA*, **97**(19), 10377–10382. 2000.

Hell S. W., Schrader M., and der Voort H. T. M. Van, "Far-field fluorescence microscopy with three-dimensional resolution in the 100-nm range", *J. Microsc.*, **187**(1), 1–7. 1997.

Hell S. W., and Stelzer E. H. K., "Properties of a 4Pi confocal fluorescence microscope", *J. Opt. Soc. Am. A*, **9**(12), 2159–2166. 1992.

Hinterdorfer P., Baumgartner W., Gruber H. J., Schilcher K., and Schindler H., "Detection and localization of individual antibody-antigen recognition events by atomic force microscopy", *Proc. Natl. Acad. Sci. USA*, **93**, 3477–3481. 1996.

Hong S. H., Zhu J., and Mirkin C. A., "Multiple ink nanolithography: toward a multiple-pen nanoplotter", *Science*, **286**, 523–525. 1999.

Horton M., Charras G., ballestrem C., and Lehenkari P., "Integration of atomic force and confocal microscopy", *Single Mol.*, **1**(2), 135–137. 2000.

Hu X., Ritz T., Damjanović A., Autenrieth F., and Schulten K., "Photosynthetic apparatus of purple bacteria", *Quarterly Rev. of Biophys.*, **35**(1), 1–62. 2002.

Jamieson S. J., Wang P. Y., Qian P., Kirkland J. Y., Conroy M. J., Hunter C. N., and Bullough P. A., "Projection structure of the photosynthetic reaction centre-antenna complex of *Rhodospirillum rubrum* at 8.5 angstrom resolution", *EMBO J.*, **21**(15), 3927–3935. 2002.

Jungas C., Ranck J. L., Rigaud J. L., Joliot P., and Vermeglio A., "Supramolecular organization of the photosynthetic apparatus of *Rhodobacter sphaeroides*", *EMBO J.*, **18**(3), 534–542. 1999.

Karrasch S., Bullough P. A., and Ghosh R., "The 8.5-angstrom projection map of the light-harvesting complex-I from *Rhodospirillum rubrum* reveals a ring composed of 16 subunits", *EMBO J.*, **14**(4), 631–638. 1995.

Klar T. A., Jakobs S., Dyba M., Egner A., and Hell S. W., "Fluorescence microscopy with diffraction resolution barrier broken by stimulated emission", *Proc. Natl. Acad. Sci. USA*, **97**(15), 8206–8210. 2000.

Klar T. A., and Hell S. W., "Subdiffraction resolution in far-field fluorescence microscopy", *Optics Lett.*, **24**(14), 954–956. 1999.

Koepke J., Hu X., Muenke C., Schulten K., and Michel H., "The crystal structures of the light-harvesting complex II (B800-850) from *Rhodospirillum molischianum*", *Structure*, **4**, 581–597. 1996.

Kolodny L. A., Willard D. M., Carillo L. L., Nelson M. W., and Orden A. Van, "Spatially correlated fluorescence/AFM of individual nanosized particles and biomolecules", *Anal. Chem.*, **73**(9), 1959–1966. 2001.

Kühnemuth R., and Seidel C. A. M., "Principles of single molecule multiparameter fluorescence spectroscopy", *Single Mol.*, **2**(4), 251–254. 2001.

Lacoste T. D., Michalet X., Pinaud F., Chemla D. S., Alivisatos A. P., and Weiss S., "Ultrahigh-resolution multicolor colocalization of single fluorescent probes", *Proc. Natl. Acad. Sci. USA*, **97**(17), 9461–9466. 2000.

Lal R., and Proksch R., "Multimodal atomic force microscopy: biological imaging using atomic force microscopy combined with light fluorescence and confocal microscopies and electrophysiologic recording", *Int. J. Imag. Syst. Tech.*, **8**(3), 293–300. 1997.

Lang R., and Kobayashi K., "External Optical Feedback Effects on Semiconductor Injection Laser Properties", *IEEE Journal of Quantum Electronics*, **QE-16**(3), 347–355. 1980.

Lau K. Y., Harder C., and Yariv A., "Longitudinal Mode Spectrum of Semiconductor Lasers Under High-Speed Modulation", *IEEE Journal of Quantum Electronics*, **QE-20**(1), 71–79. 1984.

Law C. J., and Cogdell R. J., "The effect of chemical oxidation on the fluorescence of the LH1 (B880) complex from the purple bacterium *Rhodobium marinum*", *FEBS Lett.*, **432**, 27–30. 1998.

Lee G. U., Kidwell D. A., and Colton R. J., "Sensing discrete streptavidin-biotin interactions with atomic force microscopy", *Langmuir*, **10**(2), 354–357. 1994.

Li H., Ying L., Green J. J., Balasubramanian S., and Klenerman D., "Ultrasensitive coincidence fluorescence detection of single DNA molecules", *Anal. Chem.*, **75**(7), 1664–1670. 2003.

Li Y., Maynor B. W., and Liu J., "Electrochemical AFM dip-pen nanolithography", *J. Am. Chem. Soc.*, **123**(9), 2105–2106. 2001.

Lieberman K., Ben-Ami N., and Lewis A., "A fully integrated near-field optical, far-field optical, and normal-force scanned probe microscope", *Rev. Sci. Instrum.*, **67**(10), 3567–3572. 1996.

Lim J. H., Ginger D. S., Lee K. B., Heo J., Nam J. M., and Mirkin C. A., "Direct-write dip-pen nanolithography of proteins on modified silicon oxide surfaces", *Angew. Chem.*, **115**, 2411–2414. 2003.

Lin X.-Y, Creuzet F., and Arribart H., "Atomic force microscopy for local characterization of surface acid-base properties", *J. Phys. Chem.*, **97**, 7272–7276. 1993.

Marti O., Drake B., and Hansma P. K., "Atomic force microscopy of liquid covered surfaces: atomic resolution images", *Appl. Phys. Lett.*, **51**(7), 484–486. 1987.

Marti O., Colchero J., and Mlynek J., "Combined scanning force and friction microscopy of mica", *Nanotechnology*, **1**, 141–144. 1990.

Mate C. M., McClelland G. M., Erlandsson R., and Chiang S., "Atomic-scale friction of a tungsten tip on a graphite surface", *Phys. Rev. Lett.*, **59**(17), 1942–1945. 1987.

Maynor B. W., Li Y., and Liu J., "Au ink for AFM dip-pen nanolithography", *Langmuir*, **17**(9), 2575–2578. 2001.

McDermott G., Prince S. M., Freer A. A., Hawthornthwaite-Lawless A. M., Papiz M. Z., Cogdell R. J., and Isaacs N. W., "Crystal structure of an integral membrane light-harvesting complex from photosynthetic bacteria", *Nature*, **374**, 517–521. 1995.

McKendry R., Theoclitou M. E., Rayment T., and Abell C., "Chiral discrimination by chemical force microscopy", *Nature*, **391**, 566–568. 1998.

Méndez-Vilas A., González-Martín M. L., and Nuevo M. J., "Optical Interference Artifacts in Contact Atomic Force Microscopy Images", *Ultramicroscopy*, **92**, 243–250. 2002.

Meyer G., and Amer N. M., "Novel approach to atomic force microscopy", *Appl. Phys. Lett.*, **53**(12), 1045–1047. 1988.

Minsky M., "Microscopy apparatus", *U.S. Patent, 3013467, December 19, 1961.* 1961.

Minsky M., "Memoir on inventing the confocal scanning microscope", *Scanning*, **10**, 128–138. 1988.

Monger T. G., Cogdell R. J., and Parson W. W., "Triplet states of bacteriochlorophyll and carotenoids in chromatophores of photosynthetic bacteria", *Biochim. Biophys. Acta*, **449**, 136–153. 1976.

Monshouwer R., Abrahamsson M., van Mourik F., and van Grondelle R., "Superradiance and exciton delocalization in bacterial photosynthetic light-harvesting systems", *J. Phys. Chem. B.*, **101**, 7241–7248. 1997.

Müller D. J., Engel A., and Amrein M., "Preparation techniques for the observation of native biological systems with the atomic force microscope", *Biosensors & Bioelectr.*, **12**(8), 867–877. 1997.

Müller D. J., Baumeister W., and Engel A., "Controlled unzipping of a bacterial surface layer with atomic force microscopy", *Proc. Natl. Acad. Sci. USA*, **96**(23), 13170–13174. 1999^a.

Müller D. J., Fotiadis D., Scheuring S., Müller S. A., and Engel A., "Electrostatically balanced subnanometer imaging of biological specimens by atomic force microscope", *Biophys. J.*, **76**, 1101–1111. 1999^b.

van Noort S. J. T., *Atomic force microscopy of dynamic protein DNA interactions*, PhD Thesis, University of Twente. 1999 (June).

van Noort S. J. T., van der Werf K. O., Eker A. P. M., Wyman C., de Grooth B. G., van Hulst N. F., and Greve J., "Direct visualization of dynamic protein-DNA interactions with a dedicated atomic force microscope", *Biophys. J.*, **74**, 2840–2849. 1998.

Noy A., Sanders C. H., Vezenov D. V., Wong S. S., and Lieber C. M., "Chemically-sensitive imaging in tapping mode by chemical force microscopy: relationship between phase lag and adhesion", *Langmuir*, **14**, 1508–1511. 1998.

Noy A., Miller A. E., Klare J. E., Weeks B. L., Woods B. W., and DeYoreo J. J., "Fabrication of luminescent nanostructures and polymer nanowires using dip-pen nanolithography", *Nano Lett.*, **2**(2), 109–112. 2002.

Noy A., and Huser T. R., "Combined force and photonic probe microscope with single molecule sensitivity", *Rev. Sci. Instrum.*, **74**(3), 1217–1221. 2003.

Oesterhelt F., Oesterhelt D., Pfeiffer M., Engel A., Gaub H. E., and Müller D. J., "Unfolding pathways of individual bacteriorhodopsins", *Science*, **288**, 143–146. 2000.

Ojima M., Arimoto A., Chinone N., Gotoh T., and Aiki K., "Diode Laser Noise at Video Frequencies in Optical Videodisk Players", *Applied Optics*, **25**(9), 1404–1410. 1986.

Overney R. M., Meyer E., Frommer J., and Güntherodt H. J., "Force microscopy study of friction and elastic compliance of phase-separated organic thin films", *Langmuir*, **10**, 1281–1286. 1994.

Papiz M. Z., Prince S. M., Howard T., Cogdell R. J., and Isaacs N. W., "The structure and thermal motion of the B800-850 LH2 complex from *Rps. acidophila* at 2.0 Å resolution and 100 K: new structural features and functionally relevant motions", *J. Mol. Biol.*, **326**, 1523–1538. 2003.

Parks C. A., "The isoelectric points of solid oxides, solid hydroxides, and aqueous hydroxo complex systems", *Chem. Rev.*, **65**, 177–198. 1965.

Patanè S, Gucciardi P. G., Labardi M., and Allegrini M., "Apertureless near-field optical microscopy", *Riv. Nuovo Cimento*, **27**(1), 1–46. 2004.

Pena D. J., Raphael M. P., and Byers J. M., "Dip-pen nanolithography in registry with photolithography for biosensor development", *Langmuir*, **19**(21), 9028–9032. 2003.

Perret E., Leung A., Morel A., Feracci H., and Nassoy P., "Versatile decoration of glass surfaces to probe individual protein-protein interactions and cellular adhesion", *Langmuir*, **18**(3), 846–854. 2002.

Piner R. D., Zhu J., Xu F., Hong S. H., and Mirkin C. A., "Dip-Pen Nanolithography", *Science*, **283**, 661–663. 1999.

Poolton N. R. J., and Cros Y., "Luminescence excitation and bleaching involving dangling bonds in silicon nitride", *J. Phys. I France*, **1**, 1335–1345. 1991.

Popat K. C., Johnson R. W., and Desai T. A., "Characterization of vapor deposited poly (ethylene glycol) films on silicon surfaces for surface modification of microfluidic systems", *J. Vac. Sci. Technol. B*, **21**(2), 645–653. 2003.

Porter L. A., Choi H. C., Schmeltzer J. M., Ribbe A. E., Elliott L. C. C., and Buriak J. M., "Electroless nanoparticle film deposition compatible with photolithography, microcontact printing, and dip-pen nanolithography patterning technologies", *Nano Lett.*, **2**(12), 1369–1372. 2002.

Protasenko V. V., Kuno M., Gallagher A., and Nesbitt D. J., "Fluorescence of single ZnS overcoated CdSe quantum dots studied by apertureless near-field scanning optical microscopy", *Optics. Comm.*, **210**, 11–23. 2002.

Protasenko V. V., Gallagher A., and Nesbitt D. J., "Factors that influence confocal apertureless near-field scanning optical microscopy", *Optics. Comm.*, **233**, 45–56. 2004.

Protasenko V. V., and Gallagher A., "Apertureless near-field scanning optical microscopy of single molecules", *Nano Let.*, **4**(7), 1329–1332. 2004.

Putman C. A. J., der Werf K. O. Van, Grooth B. G. De, Hulst N. F. Van, and Greve J., "Tapping mode atomic force microscopy in liquid", *Appl. Phys. Lett.*, **64**(18), 2454–2456. 1994.

Reifer D., Windeit R., Kumpf R. J., Karbach A., and Fuchs H., "AFM and TEM Investigations of Polypropylene/Polyurethane Blends", *Thin Solid Films*, **264**, 148–152. 1995.

Rief M., Gautel M., Oesterhelt F., Fernandez J. M., and Gaub H. E., "Reversible unfolding of individual titin immunoglobulin domains by AFM", *Science*, **276**, 1109–1112. 1997.

Roszak A. W., Howard T. D., Southall J., Gardiner A. T., Law C. J., Isaacs N. W., and Cogdell R. J., "Crystal structure of the RC-LH1 core complex from *Rhodopseudomonas palustris*", *Science*, **302**, 1969–1972. 2003.

Rutkauskas D., Novoderezkhin V., Cogdell R. J., and van Grondelle R., "Fluorescence spectral fluctuations of single LH2 complexes from *Rhodopseudomonas acidophila* strain 10050", *Biochemistry*, **43**(15), 4431–4438. 2004[a].

Rutkauskas D., Novoderezkhin V., Cogdell R. J., and van Grondelle R., "Fluorescence spectroscopy of conformational changes of single LH2 complexes", *Biophys. J.*, In press. 2004[b].

Salomé A., "Analysis and initial tests of the local field enhancement by a gold-coated AFM tip", *Masters thesis*. 2003.

Scheuring S., Seguin J., Marco S., Lévy D., Breyton C., Robert B., and Rigaud J. L., "AFM characterization of tilt and intrinsic flexibility of *Rhodobacter sphaeroides* light harvesting complex 2 (LH2)", *J. Mol. Biol.*, **325**, 569–580. 2003[a].

Scheuring S., Seguin J., Marco S., Lévy D., Robert B., and Rigaud J. L., "Nanodissection and high-resolution imaging of the *Rhodopseudomonas viridis* photosynthetic core complex in native membranes by AFM", *Proc. Natl. Acad. Sci. USA*, **100**(4), 1690–1693. 2003[b].

Scheuring S., Rigaud J. L., and Sturgis J. N., "Variable LH2 stoichiometry and core clustering in native membranes of *Rhodospirillum photometricum*", *EMBO*, 1–7. 2004[a].

Scheuring S., Sturgis J. N., Prima V., Lévy A. Bernadac D., and Rigaud J. L., "Watching the photosynthetic apparatus in native membranes", *Proc. Natl. Acad. Sci. USA*, **101**(31), 11293–11297. 2004[b].

Schoenenberger C. A., and Hoh J. H., "Slow cellular dynamics in MDCK and R5 cells monitored by time-lapse atomic force microscopy", *Biophys. J.*, **67**, 929–936. 1994.

Schrader M., Bahlmann K., Giese G., and Hell S. W., "4Pi-confocal imaging in fixed biological specimens", *Biophys. J.*, **75**, 1659–1668. 1998.

Schwille P., Meyer-Almes F. J., and Rigler R., "Dual-Color Fluorescence Cross-Correlation Spectroscopy for Multicomponent Diffusional Analysis in Solution", *Biophys. J.*, **72**, 1878–1886. 1997.

Segers-Nolten G. M. J., Wyman C., Wijgers N., Vermeulen W., Lenferink A. T. M., Hoeijmakers J. H. J., Greve J., and Otto C., "Scanning confocal fluorescence microscopy for single molecule analysis of nucleotide excision repair complexes", *Nucleic Acids Research*, **30**(21), 4720–4727. 2002.

Senden T. J., and Drummond C. J., "Surface chemistry and tip-sample interactions in atomic force microscopy", *Coll. and Surf. A*, **94**, 29–51. 1995.

Serpengüzel A., "Amorphous silicon nitride microcavities", *J. Opt. Soc. Am. B*, **18**(7), 989–993. 2001.

Shera E. B., Seitzinger N. K., Davis L. M., Keller R. A., and Soper S. A., "Detection of single fluorescent molecules", *Chem. Phys. Lett.*, **174**, 553–557. 1990.

Stahlberg H., Müller D. J., Suda K., Fotiadis D., Engel A., Meier T., Matthey U., and Dimroth P., "Bacterial Na^+-ATP synthase has an undecameric rotor", *EMBO reports*, **2**(3), 229–233. 2001.

Stark R. W., Drobek T., and Heckl W. M., "Thermomechanical noise of a free v-shaped cantilever for atomic-force microscopy", *Ultramicroscopy*, **86**, 207–215. 2001.

Sundström V., Pullerits T., and van Grondelle R., "Photosynthetic light-harvesting: reconciling dynamics and structure of purple bacterial LH2 reveals function of photosynthetic unit", *J. Phys. Chem. B.*, **103**, 2327–2346. 1999.

Thalhammer S., Stark R. W., Müller S., Wienberg J., and Heckl W. M., "The atomic force microscope as a new microdissecting tool for the generation of genetic probes", *J. Struct. Biol.*, **119**, 232–237. 1997.

Thomson R. E., "Low-temperature atomic force microscope using piezoresistive cantilevers", *Rev. Sci. Instrum.*, **70**(8), 3369–3372. 1999.

Toda A., Kitazawa M., and Yagi A., "Silicon tip cantilevers for force microscopy in water with resonance of 20 kHz or above", *Japanese J. Appl. Phys.*, **43**(7B), 4671–4675. 2004.

Tortonese M., Barret R. C., and Quate C. F., "Atomic resolution with an atomic force microscope using piezoresistive detection", *Appl. Phys. Lett.*, **62**(8), 834–836. 1993.

Trabesinger W., Kramer A., Kreiter M., Hecht B., and Wild U. P., "Single-molecule near-field optical energy transfer microscopy with dielectric tips", *J. Microscopy*, **209**, 249–253. 2003.

Viani M. B., Pietrasanta L. I., Thompson J. B., Chand A., Gebeshuber I. C., Kindt J. H., Richter M., Hansma H. G., and Hansma P. K., "Probing protein-protein interactions in real time", *Nature Struct. Biol.*, **7**(8), 644–647. 2000.

Wallace M. I., Molloy J. E., and Trentham D. R., "Combined single-molecule force and fluorescence measurements for biology", *J. Biol.*, **2**, 4.1–4.5. 2003.

Walz T., Jamieson S. J., Bowers C. M., Bullough P. A., and Hunter C. N., "Projection structures of three photosynthetic complexes from *Rhodobacter sphaeroides*: LH2 at 6 Å, LH1 and RC-LH1 at 25 Å", *J. Mol. Biol.*, **282**, 833–845. 1998.

Weisenhorn A. L., Maivald P., Butt H. J., and Hansma P.K., "Measuring Adhesion, Attraction, and Repulsion between Surfaces in Liquids with an Atomic-Force Microscope", *Physical Review B*, **45**(19), 11226–11232. 1992.

Weiss S., "Fluorescence spectroscopy of single biomolecules", *Science*, **283**, 1676–1683. 1999.

van der Werf K. O., Putman C. A. J., de Grooth B. G., Segerink F. B., Schipper E. H., van Hulst N. F., and Greve J., "Compact stand-alone atomic force microscope", *Rev. Sci. Instrum.*, **64**(10), 2892–2897. 1993.

White J. G., Amos W. B., and Fordham M., "An evaluation of confocal versus conventional imaging of biological structures by fluorescence light microscopy", *J. Cell. Biol.*, **105**, 41–48. 1987.

Willemsen O. H., *Tip surface interactions in atomic force microscopy*, PhD Thesis, University of Twente. 1999.

Winkler T., Kettling U., Koltermann A., and Eigen M., "Confocal fluorescence coincidence analysis: An approach to ultra high-throughput screening", *Proc. Natl. Acad. Sci. USA*, **96**, 1375–1378. 1999.

Wolford D. J., Scoot B. A., Reimer J. A., and Bradley J. A., "Efficient visible luminescence from hydrogenated amorphous silicon", *Physica B*, **117-118**, 920–922. 1983.

Wong S. S., Joselevich E., Woolley A. T., Cheung C. L., and Lieber C. M., "Covalently functionalized nanotubes as nanometre-sized probes in chemistry and biology", *Nature*, **394**, 52–55. 1998.

Xu C., Zipfel W., Shear J. B., Williams R. M., and Webb W. W., "Multiphoton fluorescence excitation: New spectral windows for biological nonlinear microscopy", *Proc. Natl. Acad. Sci. USA*, **93**, 10763–10768. 1996.

Yu Y. Y., Chang S. S., Lee C. L., and Wang C. R. C., "Gold nanorods: electrochemical synthesis and optical properties", *J. Phys. Chem. B*, **101**(34), 6661–6664. 1997.

Zenhausern F., O'Boyle M. P., and Wickramashinghe H. K., "Apertureless near-field optical microscopy", *Appl. Phys. Lett.*, **65**(13), 1623–1625. 1994.

Zhong Q., Inniss D., Kjoller K., and Elings V., "Fractured polymer/silica fiber surface studied by tapping mode atomic force microscopy", *Surf. Sci. Lett.*, **290**, L688–L692. 1993.

Appendix A

Cantilever properties of the chip MSCT-AUHW, Veeco Microlevers

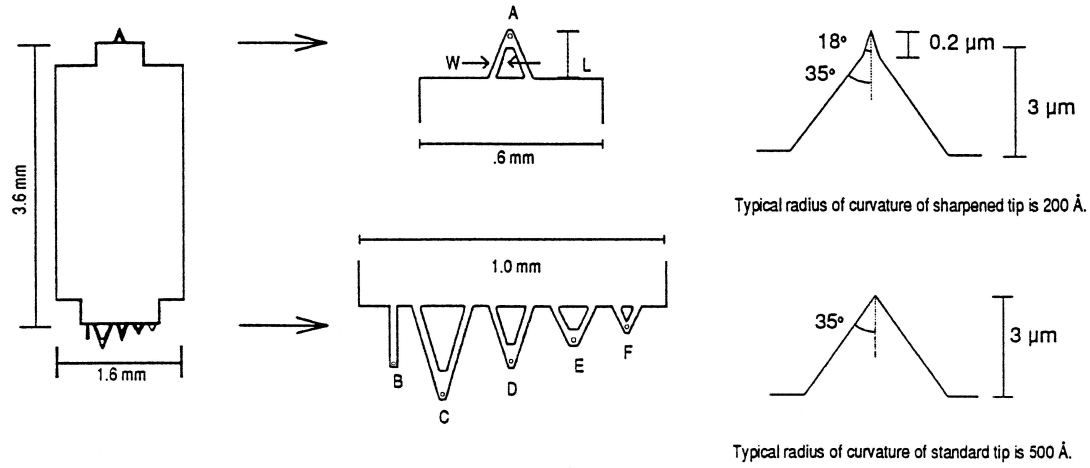

Cantilever type	A	B	C	D	E	F
Length	180 μm	200 μm	320 μm	220 μm	140 μm	85 μm
Width	18 μm	20 μm	22 μm	22 μm	18 μm	18 μm
Thickness	0.6 μm	0.6 μm	0.6 μm	0.6 μm	0.6 μm	0.6 μm
Force Constant	0.05 N/m	0.02 N/m	0.01 N/m	0.03 N/m	0.10N/m	0.50 N/m
Resonant freq. (air)	22 kHz	15 kHz	7 kHz	15 kHz	38 kHz	120 kHz

Glossary of Symbols and Abbreviations

Abbreviation	description
AFM	atomic force microscope / microscopy
AFFM	atomic force fluorescence microscope
ANSOM	apertureless near-field scanning optical microscopy
APD	avalanche photo diode
Ar-Kr	Argon-Krypton
ATP	adenosine triphosphate
Bchl	bacteriochlorophyll
Car	carotenoid
CCD	charge-coupled device
CFM	confocal fluorescence microscope / microscopy
CSOM	confocal scanning optical microscope
CW	continuous wave
DAQ	data aquisition
DPN	dip-pen nanolithography
FCS	fluorescence correlation spectroscopy
FCCS	fluorescence cross-correlation spectroscopy
FRET	fluorescence resonance energy transfer
FWHM	full width at half maximum
HELM	harmonic excitation light-microscopy
IR	infrared
LH	light harvesting complex
NA	numerical aperture
NIR	near infra-red
NSOM	near-field scanning optical microscopy
PLL	poly-L-lysine
PSF	point spread function
QD	quantum dot
RC	reaction center
r.m.s.	root mean square
SPM	scanning probe microscope
STED	stimulated emission depletion
STM	scanning tunneling microscope
SVD	singular value decomposition
TIRFM	total internal reflection fluorescence microscopy

Summary

Optical microscopy was the first method that enabled humans to observe worlds hidden to the naked eye. The technique was immediately applied by Antoni van Leeuwenhoek to study microscopic biology and today it is still one of the most important tools in biological research. Since its invention in the 1590's, optical microscopy has been developed further and perfected to a level where the light emitted by individual molecules can be observed. Properties of this light such as intensity, wavelength, polarization and lifetime provide valuable information about the nature of the specimen and it's surroundings. However, in observing ever smaller details, the attainable resolution in optical microscopy is ultimately limited by diffraction to roughly half the wavelength of the light.

A fundamentally different microscopy technique, scanning probe microscopy, was first introduced in 1981 by the invention of the scanning tunneling microscope. Scanning probe microscopes use a very sharp tip to trace the surface contours of the specimen, thereby forming a highly detailed topographic image. This technique enables imaging with a much higher resolution than that obtainable with optical methods. From the family of scanning probe microscopes, the atomic force microscope (AFM) is the most widely used scanning probed technique in biological research, because of its ability to image with very high spatial resolution in a biologically relevant aqueous environment. In AFM, the forces between the tip and the sample surface are used to map the surface topography. These general tip sample interactions make AFM applicable to a wide range of samples. However, this also strongly limits its capacity to identify different objects of the sample, unless they have a very distinct shape or size.

The complementary strengths and weaknesses of AFM and optical microscopy leads to the desire to integrate both techniques into a single microscope. This thesis describes the development of a combined AFM / confocal fluorescence microscope. This *atomic force fluorescence microscope* (AFFM) combines high resolution structural imaging with (bio-)chemically specific optical imaging.

The instrument is primarily constructed for the research on bacterial photosynthesis. The efficiency of the photosynthetic apparatus of these bacteria strongly relies on the structural organization of its individual components and the higher order organization of the whole system. The AFFM can reveal new insight in this system because of its ability to directly relate high resolution structural information of the system to its functional (optical) properties. In addition, the AFM tip can be used as a force sensor/manipulator to interact with the molecules while simultaneously observing the optical responses.

A number of strict requirements for the AFFM are defined in **chapter 2**, followed by a description of the design of the confocal fluorescence microscope and the atomic force microscope. Several distinct modes of operation are implemented in the software, such as simultaneous topographic and optical imaging, combined AFM and spectral fluorescence imaging and force extension measurements with simultaneous optical detection. These modes of operation make the instrument applicable for many types of experiments.

AFM systems that use the optical lever method to detect the cantilever displacement can suffer from serious interference and optical feedback disturbances. The AFFM was highly affected by optical feedback effects during imaging and force extension measurements, and also interference artifacts were present. In **chapter 3**, these disturbances are demonstrated and application of high frequency laser current modulation is shown to strongly decrease interference effects and completely eliminate optical feedback artifacts. A small and compact modulator is described that is suitable for driving the laser current modulation. This small package allows the application of this technique in any (commercial) AFM system.

In **chapter 4**, the performance of the AFFM is evaluated in terms of detection sensitivity and signal-to-noise ratio. The confocal fluorescence microscope and the AFM are treated separately. The fluorescence microscope is shown to be capable of detecting single molecule fluorescence up to the near-IR spectral region. This can be achieved with high time resolution using the APD as well as spectrally resolved using the spectrograph and CCD camera. The AFM, as integrated with the fluorescence microscope is capable of resolving the structure of individual ring shaped pigment protein complexes.

The combined operation of the AFFM is demonstrated in **chapter 5** on samples from the photosynthetic bacterium *Rhodobacter sphaeroides*. Simultaneous imaging is performed on 2 dimensional crystals of LH2 complexes clearly demonstrating the difference in resolution of both microscopy techniques. Combined topographic and spectral fluorescence imaging on membrane fragments shows the powerful identification capacity of spectral imaging. The attempts to perform simultaneous measurements on individual light harvesting complexes are described along with the challenges that are involved with these type of experiments.

Although primarily designed for research on bacterial photosynthesis, the AFFM is a powerful instrument for a wide scope of biophysical research topics. The general applicability if the instrument is significantly increased by the availability of a wide range of visible excitation wavelengths through a fiber connection to a mixed gas Argon-Krypton laser. **Chapter 6** describes a prism-based wavelength selector that enables the easy and flexible selection of any wavelength or any combination of wavelengths from this multi-wavelength laser, with high overlap precision.

Chapter 7 provides an outlook on future applications of the AFFM in biophysical and (bio-) nanotechnological research.

Samenvatting

Optische microscopie verschafte de mens de eerste mogelijkheid om werelden te observeren die verborgen zijn voor het blote oog. Deze techniek werd door Antoni van Leeuwenhoek meteen al toegepast om de microscopische biologie te bestuderen en is tot op de dag van vandaag een van de belangrijkste gereedschappen in biologisch onderzoek. Sinds de uitvinding ervan omstreeks 1590 is de optische microscopie verder ontwikkeld en geperfectioneerd zodat het nu mogelijk is om licht, uitgezonden door een enkel molekuul, waar te nemen. Eigenschappen van dit licht zoals intensiteit, polarisatie, golflengte en levensduur verschaffen veel informatie over het monster en zijn omgeving. Echter, bij het observeren van steeds kleinere details is de bereikbare resolutie in optische microscopie gelimiteerd door diffractie tot ingeveer de helft van de golflengte van het licht.

Een fundamenteel andere microscopie techniek, 'scanning probe' microscopie, werd voor het eerst geïntroduceerd in 1981 met de uitvinding van de 'scanning tunneling' microscoop. Scanning probe microscopen tasten met een heel scherpe naald de oppervlakte contouren van het monster af, waarbij een gedetailleerd topografisch plaatje wordt gevormd. Met deze techniek kan een veel hogere resolutie behaald worden dan met optische methoden. Van de familie van scanning probe microscopen wordt de atomaire krachtsmicroscoop (atomic force microscope, AFM) het meest toegepast in biologisch onderzoek omdat met deze techniek plaatjes met hoge resolutie kunnen worden gemeten in biologisch relevante vloeistof omgeving. Bij AFM wordt de krachtsinteractie tussen een scherpe tip en het oppervlak gebruikt om een hoogte plaatje van het monster te maken. Omdat bij AFM gebruik wordt gemaakt van zeer algemene krachtsinteracties, kan de techniek op velerlei monsters worden toegepast. Tegelijkertijd beperkt dit de capaciteit om verschillende objecten van het monster te identificeren, tenzij de objecten een heel specifieke vorm of grootte hebben.

De sterke en zwakke aspecten van AFM en optische microscopie vullen elkaar precies aan, en daardoor leidt de integratie van beide technieken in een enkele microscoop tot een krachtig instrument. Dit proefschrift beschrijft de ontwikkeling van een gecombineerde AFM / confocale fluorescentie microscoop. Deze *atomic force fluorescence microscope* (AFFM) combineert de capaciteit om zeer gedetailleerde structurele informatie te meten met AFM met de specifieke (bio-)chemische gevoeligheid van fluorescentie microscopie.

De microscoop is primair ontworpen voor het onderzoek aan bacteriële fotosynthese. De efficiëntie van het fotosynthetisch apparaat van deze bacteriën is sterk afhankelijk van de structuur van de individuele componenten en van de organisatie van het systeem als geheel. De AFFM kan nieuw inzicht verschaffen in dit systeem door de mogelijkheid om direct nauwkeurige structuur informatie te relateren aan functionele (optische) eigenschappen. Daarnaast kan de AFM tip gebruikt worden als krachts sensor/manipulator waarmee een interactie kan worden aangegaan met de moleculen terwijl tegelijkertijd de optische responsen worden gemeten.

Een aantal strikte eisen waaraan de AFFM moet voldoen, wordt gedefinieerd in **hoofdstuk 2**, gevolgd door een beschrijving van het ontwerp van de confocale fluorescentie microscoop en de atomaire krachtsmicroscoop. Een aantal verschillende operationele modi zijn geimplementeerd in de

software, zoals simultaan topografisch en optisch afbeelden, gecombineerd AFM en spectraal opgelost fluorescent afbeelden, en zgn. 'force-extension' metingen met simultane optische detectie. Deze modi maken het instrument geschikt voor veel verschillende typen experimenten.

AFM systemen die de 'optical lever' methode gebruiken om de cantilever positie te detecteren, kunnen aanzienlijke hinder ondervinden van verstoringen door interferentie en optische feedback. In de AFFM waren optische feedback effecten sterk aanwezig gedurende het maken van afbeeldingen en force extension metingen. Daarnaast waren ook interferentie effecten aanwezig. In **hoofdstuk 3** worden deze verstoringen gedemonstreerd. Door toepassing van hoog frequente laser stroom modulatie worden interferentie effecten sterk verminderd en worden de optische feedback effecten volledig voorkomen. Een zeer compacte modulator kan gebruikt worden om de hoog frequente modulatie stroom te genereren. De kleine omvang van deze modulator maakt het mogelijk om deze techniek toe te passen in elk (commerciëel) AFM systeem.

In **hoofdstuk 4** worden de prestaties van de AFFM geëvalueerd in termen van detectie gevoeligheid en signaal-ruisverhouding. De confocale fluorescentie microscoop en de AFM worden apart behandeld. De fluorescentie microscoop is in staat om fluorescentie van individuele molekulen waar te nemen tot in het nabij infra rode gebied van het spectrum. Dit kan zowel met hoge tijdsresolutie met behulp van de APD detector als spectraal opgelost met behulp van de spectrograaf met CCD camera. De AFM is, ondanks de integratie met de optische microscoop, in staat om met zeer hoge resolutie de individuele ringvormige light-harvesting complexen af te beelden.

Gecombineerde experimenten met de AFFM worden in **hoofdstuk 5** gedemonstreerd op monsters van de fotosynthetische bacterie *Rhodobacter sphaeroides*. Het simultaan afbeelden met de twee technieken is uitgevoerd op 2-dimensionale kristallen van LH2 complexen. Dit laat duidelijk het verschil in haalbare resolutie van de twee microscopie technieken zien. Het gecombineerd topografisch en spectraal opgelost fluorescent afbeelden van membraan fragmenten toont de krachtige identificatie capaciteit van de AFFM. Tevens worden de experimenten die gedaan zijn met simultane metingen op individuele molekulen beschreven en de uitdagingen van deze experimenten bediscussiëerd in dit hoofdstuk.

Hoewel de AFFM primair voor onderzoek aan bacteriële fotosynthese is ontworpen, is het een krachtig instrument voor een breed spectrum aan biofysische onderzoeks onderwerpen. De algemene toepasbaarheid van de microscoop is sterk vergroot met de beschikbaarheid van een groot aantal zichtbare excitatie golflengtes door een fiber verbinding met een mixed gas Argon-Krypton laser. **Hoofdstuk 6** beschrijft een golflengte selector bestaande uit twee prisma's en een retro-reflector die het mogelijk maakt om eenvoudig elke golflengte of combinatie van golflengtes te selecteren van deze multi-golflengte laser, met een grote overlap precisie.

Hoofdstuk 7 biedt een vooruitblik op toekomstige toepassingen van de AFFM in biofysisch en (bio-)nanotechnologisch onderzoek.

Nawoord

Met de afronding van dit proefschrift komt er een einde aan ruim vier jaar promotieonderzoek. Terugkijkend is het op vele vlakken een erg leerzame tijd geweest. Met als doelstelling om met behulp van een geïntegreerde AFM/optische microscoop simultane metingen te doen aan individuele eiwitten, ben ik begonnen met de bouw van deze microscoop. De metingen die we voor ogen hadden stelden strenge eisen aan het instrument, waardoor de ontwikkeling ervan een uitdagend project was. Het was een goede manier om beide technieken tot in detail te leren kennen. De bouw van de microscoop ging niet altijd vanzelf. De 'wet van Murphy' heb ik uitgebreid getoetst. Aan de andere kant bleek een aanvankelijk probleem later juist nieuwe mogelijkheden te bieden. Al met al was het erg leuk om zo'n hoogwaardige microscoop te construeren. De Atomic Force Fluorescence Microscope is gerealiseerd, en ik ben er trots op. Het is de eerste combinatie microscoop die daadwerkelijk simultaan op het niveau van individuele moleculen kan meten in een biologisch relevante omgeving.

Het meten aan enkele moleculen, in het regiem van nanometers en individuele fotonen, heeft mij gefascineerd. De simultane metingen op light harvesting complexen waren erg uitdagend. Het was wel eens frustrerend om experimenten te doen waarbij aan zoveel soms tegenstrijdige randvoorwaarden, opgelegd door beide technieken, moet worden voldaan. Ik had nog erg graag de eerste kracht gerelateerde optische signalen van individuele moleculen willen meten. Ik denk dat we er dicht bij zijn, maar het zat er voor mij helaas net niet meer in. Ik heb er in ieder geval alle vertrouwen in dat het apparaat toegepast gaat worden in allerlei toekomstige projecten.

Het onderzoek was niet mogelijk geweest zonder de samenwerking met prof. Neil Hunter en dr. John Olsen van de universiteit van Sheffield (UK) en prof. Rienk van Grondelle van de Vrije Universiteit Amsterdam. John, I would like to thank you for the pleasant discussions about the photosynthetic bacteria and the light harvesting complexes. I have enjoyed your enthusiasm for future experiments. Neil and John, thank you for providing us with many different samples. Rienk, bedankt voor de discussies over de optische aspecten van de light harvesting complexen. We hebben elkaar niet zo vaak gesproken, maar de paar ontmoetingen die we hebben gehad waren zeer nuttig. The collaboration with all of you has introduced us into the fascinating world of photosynthesis. I think this system is a perfect example of the complexity and beauty of nature.

Het werken bij BPE (BioPhysical Engineering) was altijd erg plezierig. Dit komt vooral door de gezellige sfeer die altijd in de leerstoel aanwezig is. Graag wil ik daarom iedereen binnen BPE bedanken voor de geweldige tijd! Toch wil ik graag een aantal mensen apart bedanken:
Cees voor dat je me na mijn afstuderen gevraagd hebt voor dit project. De inhoud paste goed bij mijn interesses en ik heb geen moment spijt gehad van de beslissing om eraan te beginnen.
Vinod voor het enorme enthousiasme voor de AFFM en voor de stimulans om het apparaat snel te publiceren. Het is jammer dat ik je maar zo kort als hoogleraar heb kunnen meemaken.
Martin voor je nuttige opmerkingen en suggesties tijdens de werkbesprekingen.
Aufried voor de technische ondersteuning. Daarnaast maakte je grote gevoel voor humor de pauzes

altijd extra gezellig.
Ine voor de talloze goede gesprekken die we hebben gehad. Bedankt dat ik altijd even mijn verhaal kwijt kon of gewoon even gezellig kon komen kletsen.
Kirsten voor je hulp in het chemische lab.
Evgueni, Yuri en Natallia voor de gezellige atmosfeer binnen de Raman groep.
Svetlana voor de prettige samenwerking en voor de gezellige tijd als kamergenoten.
Henk-Jan, Mathilde, Jurgen, Kirsten, Yvonne, Aufried, Martijn en alle anderen van het vollebal groepje voor de leuke partijtjes die we elke week speelden.
Jurgen voor de goede samenwerking en vriendschap. Het was stimulerend om allebei aan een eigen opstelling te werken en onze ervaringen uit te wisselen.
Hans de Boer voor de onderdelen die je voor de microscoop hebt gemaakt. Je was altijd bereid om mee te denken over het ontwerp van de constructie om er iets goeds van te maken.
Johan voor je technische hulp, vooral voor al je pogingen om het optische filter op maat te maken.
Frans Segerink voor je hulp bij de software ontwikkeling voor de microscoop. Ik kon altijd bij je langskomen met vragen en dat heb ik erg gewaardeerd.
Roy voor je behulpzaamheid en de scherpe diagnose van het 'aliasing probleem'.
Srirang voor de vele malen dat ik je mocht storen met een vraag over LaTeX.
Arnout voor je werk tijdens je afstudeer project en je vriendschap in die periode en daarna.
Frans voor je bereidwilligheid om met vanalles te helpen en voor het uitwisselen van ditjes en datjes 's ochtends om half acht.
Sylvia voor alles wat je voor me hebt gedaan als secretaresse van de groep, maar vooral ook voor je persoonlijke interesse en spontaniteit.
Kees van der Werf voor je geweldige begeleiding. Zonder jou was dit proefschrift nooit geworden wat het nu is. Je creativiteit en enthousiasme heeft me enorm geinspireerd en ik heb erg veel van je geleerd op allerlei gebied. Bedankt!

Ook wil ik mijn familie bedanken. Pap en mam, bedankt voor alles wat jullie mij hebben meegegeven en voor jullie nooit aflatende steun en betrokkenheid. Wiesje en Jaap, Gera en Henk, Remke en Joost, bedankt voor de interesse die jullie altijd toonden voor mijn werk.
En ten slotte mijn speciale dank aan Nan. Mijn dank voor jouw onvoorwaardelijke steun en je liefdevol luisterend oor is niet in een zin te vatten. Jouw betrokkenheid bij alles is hartverwarmend.

Roel

Publications

Papers

Kassies R., van der Werf K. O., Bennink M. L., and Otto C., "Removing interference and optical feedback artifacts in atomic force microscopy measurements by application of high frequency laser current modulation", *Rev. Sci. Instrum.*, **75**(3), 689-693. 2004.

Kassies R., van der Werf K. O., Lenferink A., Hunter C. N., Olsen J. D., Subramaniam V., and Otto C., "Combined AFM and confocal fluorescence microscope for applications in bio-nanotechnology", *J. Microscopy*, **217**, 109-116. 2005.

Kassies R., Lenferink A., Segers-Nolten G. M. J., and Otto C., "Prism-based excitation wavelength selection for multicolor fluorescence coincidence measurements", *Applied Optics*, **44**(6), 1-5. 2005.

Kassies R., van der Werf K. O., and Subramaniam V., "Compact laser modulator for elimination of interference and optical feedback disturbances in AFM", in preparation.

Conference and meeting contributions

Kassies R., Bahatyrova S., Hunter C. N., van Grondelle R., Greve J., and Otto C., "Structural and optical properties of LH2-complexes", *Proceedings of the Dutch Annual Conference on BioMedical Engineering*, pp. 73–74, Papendal. (poster and oral presentation) 2001.

Kassies R., Bahatyrova S., Hunter C. N., van Grondelle R., Greve J., and Otto C., "Structural and optical properties of LH2-complexes", *9th European Conference on the Spectroscopy of Biological Molecules*, pp. 95–95, Prague. (poster) 2001.

Kassies R., Bahatyrova S., Hunter C. N., van Grondelle R., Greve J., and Otto C., "Structural and optical properties of LH-complexes", *7th Conference on Methods and Applications of Fluorescence*, Amsterdam. (poster) 2001.

Kassies R., Bahatyrova S., Hunter C. N., van Grondelle R., Greve J., and Otto C., "AFM and Confocal Fluorescence Microscopy on Single LH2 Complexes", *8th International Workshop on Single Molecule Detection and Ultrasensitive Analysis in Life Sciences (PicoQuant)*, Berlin. (poster) 2002.

Kassies R., Bahatyrova S., Hunter C. N., van Grondelle R., Greve J., and Otto C., "Confocal microscopy and AFM on light harvesting complexes", *Proceedings of the Dutch Annual Conference on BioMedical Engineering*, pp. 59–60, Papendal. (poster) 2002.

Kassies R., Bahatyrova S., Hunter C. N., van Grondelle R., Greve J., and Otto C., "AFM and Confocal Microscopy on Light Harvesting Complexes", *Annual Linz Winter Workshop*, Linz. (poster) 2003.

Kassies R., Bahatyrova S., Hunter C. N., van Grondelle R., Greve J., and Otto C., "Force and optical microscopy on light harvesting complexes", *ALW/FOM/VvBBMT Meeting on Molecular and Cellular Biophysics*, Lunteren. (poster) 2003.

Kassies R., Bahatyrova S., Hunter C. N., van Grondelle R., Greve J., and Otto C., "A new combined AFM/confocal fluorescence microscope for study of biomolecules", *Proceedings of the Dutch Annual Conference on BioMedical Engineering*, pp. 82–83, Papendal. (poster) 2003.

Kassies R., van der Werf K. O., Lenferink A. T. M., van Grondelle R., Olsen J. D., Hunter C. N., and Otto C., "Combined AFM/CFM for the study of Photosynthetic Systems", *KNAW meeting*, Amsterdam. (oral presentation) 2004.

Kassies R., van der Werf K. O., Lenferink A. T. M., Hunter C. N., van Grondelle R., Subramaniam V., and Otto C., "Combined force- and optical spectroscopy on a bacterial photosynthetic system", *ALW/FOM/VvBBMT Meeting on Molecular and Cellular Biophysics*, Lunteren. (poster) 2004.

Kassies R., van der Werf K. O., Lenferink A. T. M., Subramaniam V., and Otto C., "Combined AFM/Fluorescence Microscopy on Bacterial Light Harvesting Complexes", *MESA+ dag*, Enschede. (oral presentation) 2004.

Kassies R., van der Werf K. O., Lenferink A. T. M., Hunter C. N., Olsen J. D., Subramaniam V., and Otto C., "A combined afm/confocal fluorescence microscope with single molecule sensitivity for application in bio-nanotechnology", *Proceedings of the Dutch Annual Conference on BioMedical Engineering*, pp. 148–149, Papendal. (poster and oral presentation) 2004.